Réponses optiques linéaires et non linéaires de semi-métaux chiraux multifolds

Miguel Angel Sánchez Martínez

Université Grenoble Alpes

THÈSE

Pour obtenir le grade de

DOCTEUR DE L'UNIVERSITE GRENOBLE ALPES

Spécialité : **Physique de la Matière Condensée et du Rayonnement**

Arrêté ministériel : 25 mai 2016

Présentée par

Miguel Ángel SÁNCHEZ MARTÍNEZ

Thèse dirigée par **Serge FLORENS, Université Grenoble Alpes**,
et codirigée par **Adolfo GRUSHIN, Université Grenoble Alpes**

préparée au sein du **Laboratoire Institut Néel**
dans **l'École Doctorale Physique**

Réponses optiques linéaires et non linéaires des semi-métaux chiraux multifolds

Linear and nonlinear optical responses of chiral multifold semimetals

Thèse soutenue publiquement le **« 23 novembre 2021 »**,
devant le jury composé de :

Ana AKRAP
Professeure associée, Université de Fribourg, Examinatrice
David CARPENTIER
Directeur de recherche, ENS Lyon, Président du jury
Jens BARDARSON
Professeur, KTH, Rapporteur
Mark Olivier GOERBIG
Directeur de recherche, Université Paris-Sud, Rapporteur
Milan ORLITA
Chargé de Recherche, LNCMI-CNRS, Examinateur

Linear and nonlinear optical responses of chiral multifold semimetals

Miguel Ángel Sánchez Martínez

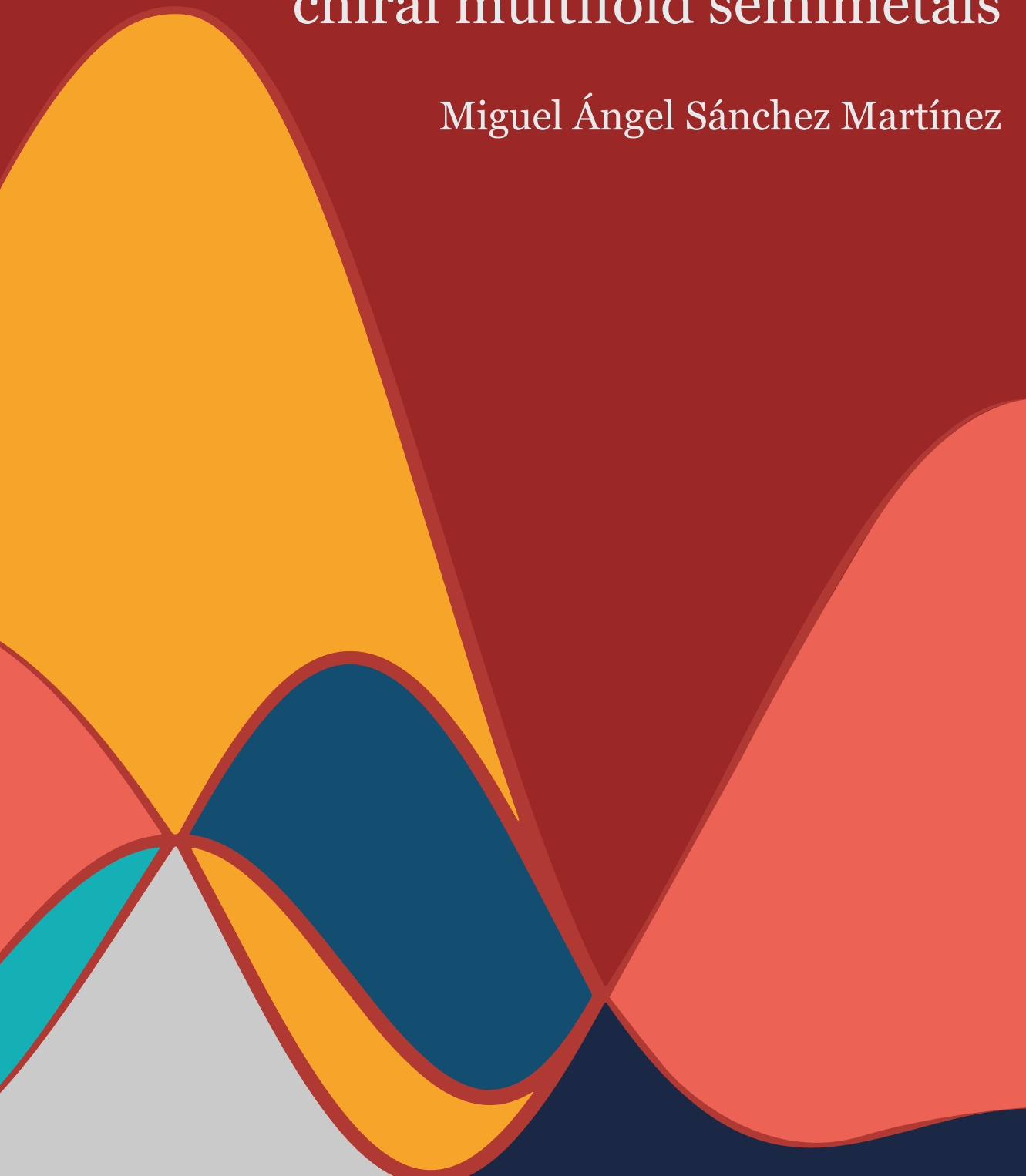

Linear and nonlinear optical responses of chiral multifold semimetals

A DISSERTATION PRESENTED
BY
MIGUEL ÁNGEL SÁNCHEZ MARTÍNEZ
UNDER THE SUPERVISION OF
ADOLFO G. GRUSHIN AND SERGE FLORENS
FOR THE DEGREE OF
DOCTOR
IN THE SUBJECT OF
PHYSICS

UNIVERSITÉ GRENOBLE ALPES
GRENOBLE, FRANCE
SEPTEMBER 2021

Contents

Acknowledgments

Like every endeavour, a thesis is not an individual accomplishment. I am indebted to many people who have contributed in different ways to the success of this thesis.

In the first place, I would like to thank my supervisor Adolfo G. Grushin. His patience, pedagogy, and kindness have been fundamental for the success of this thesis. I value each of the many hours that he has spent teaching me and discussing with me. I have learned enormously from his scientific style, his way of managing a research project, and his way of thinking about physics. He has been a mentor, and I am convinced that I will keep with me many of the lessons he taught me during my whole professional career.

I would like to thank Ana Akrap, David Carpentier, Maia García Vergniory, Mark Oliver Goerbig, Milan Orlita, and Jens Bardarson who generously accepted to be a part of my PhD committee.

During my time in Grenoble I had the luck to meet great scientists and human beings. I want to thank Serge Florens for his help and amability. He was the first person that helped me when I arrived in Grenoble, and he did not stop doing it during these years. I would like to express my gratitude to Simone Fratini. I always appreciated a conversation with him, a nice coffee, and some advice. He always helped me when I asked him for help, and he did it in the most kind and friendly way. Thank you for your friendship.

I have been lucky enough to collaborate with amazing physicists during my PhD. I would like to thank Fernando de Juan for his amability, his unbounded knowledge, and his willingness to help. Thanks to him I learned how to deal with unexpected results the day before submitting my first paper and how a Mathematica notebook should look like, among many other things. And I would like to thank Jörn Venderbos. His close style, his cheerfulness, and his amability have been a gift in every physics discussion. Thank you very much.

When I went to Santa Barbara I had the enormous luck to work with Andrey Antipov, who has helped me immensely since the very first moment we met. I have learned a lot from our many physics discussions, his management skills, and his mentoring style. I am lucky enough to keep working with him to this day, and I hope I can keep this good fortune for a long time. Thank you very much.

Working in a research institute involves correlating your work with that of many people in many different areas. I would like to thank Élodie Bernard and Patrick Belmain. They have always been helpful and kind to every PhD student I ever met at the lab. Thank you.

I was lucky enough to find friends instead of officemates. I would like to thank Théo Sepulcre. I always turned to him when some math was too hard and, thanks to him, I have received more lessons about the Fabry-Perot interferometer than any other human alive. Thank you for your friendship. I would like to thank Massimiliano Comin. His unique style of telling stories and living the life has provided us with countless hours of laughter and anecdotes. Thank you for every call in the name of Miguel Ángel Rodríguez González.

Your friends are the family you get to choose. I would like to thank Katee Driscoll. You have been my family in Grenoble, and that is the best I could hope for. Thank you for your infinite help, your friendship, and your cheerfulness. Quiero agradecer a mi amigo Fito su cercanía, su amabilidad, y su alegría. Has formado parte de mi familia en Grenoble, y eso es lo mejor que le puedo pedir a alguien.

Quisiera agradecer a mis amigos de siempre, Arturo, Pablo y Jorge. Admiro muchas cosas (y muy diferentes) de cada uno de vosotros. A los tres os tengo que agradecer vuestra amistad sincera y maravillosa. Cada una de las larguísimas conversaciones que hemos tenido sobre la vida, la existencia, el amor, el desamor, sobre todo lo que nos rodea me han hecho ser quien soy. Gracias de corazón.

Finalmente, quiero agradecer a las personas que forman parte de mi alma, que sienten cada uno de mis logros y de mis fracasos como suyos propios.

A los más pequeños de la casa, Runa, Drogo y Fiona. La infinita ilusión que me produce cada uno de los momentos con vosotros es una fuente continua de alegría en mi vida. Gracias por vuesto amor. Os quiero.

A mi abuela Charo. Gracias por haberme cuidado, por haberme consentido y por quererme incondicionalmente. Gracias por tu curiosidad, por tus ganas de aprender. Atesoro nuestras conversaciones en mi corazón como las de dos amigos que se entienden de verdad. Gracias por tu amor. Te quiero.

A mi padre, Miguel Ángel. Gracias por haber sido un hombre extraordinariamente bueno, por regalarme tus horas con alegría, por haberme descubierto la naturaleza, por tu generosidad. Gracias por el precioso tiempo compartido. Gracias por tu amor. Te quiero.

A Enrique. Gracias por tu paciencia, por tu bondad, por tu infinita disposición, por tu preocupación discreta y sincera, por estar siempre cuando he necesitado ayuda. Gracias por las ilusiones compartidas. Gracias por tu amor. Te quiero.

A mi hermana, Julia. Mi mitad, la persona que comparte mi historia, mis pensamientos, mi experiencia vital. Tengo la enorme fortuna de que mi única hermana sea una mujer extraordinaria, valiente e íntegra. Te admiro enormemente. Muchas gracias por todo lo que me has enseñado. Vas a conseguir todo lo que te propongas, y vas a salvar muchas vidas haciéndolo. Te quiero con todo mi corazón.

A mi madre, Carmen, se lo debo todo. Soy quien soy por cada una de las infinitas horas que ha dedicado a hablar conmigo, a conversar, a enseñarme, a educarme desde que tengo memoria. Hay muchas cosas que admiro de ti, y quizá tu tenacidad es la que más me sorprende. Nada de lo que he hecho lo hubiera podido hacer sin tu apoyo y sin tu amor. Espero poder darle a mis hijos tanto como me has dado tú a mí. Te quiero, mamá.

Por último, al amor de mi vida, Ana Luisa. Como todos los proyectos que emprendemos en la vida, esta tesis es un éxito de los dos. Entre las muchas virtudes que admiro de ti, tu bondad, tu corazón cálido y tu generosidad son las que más me fascinan. Gracias por tu alegría, por tu risa, por tu comprensión, por tu forma de quererme. Gracias a ti he sentido el amor que ha inspirado canciones e historias desde los albores de la humanidad. Gracias por ser mi hogar. Yo siempre quise estudiar física para entender el sentido de la existencia. A tu lado, he descubierto el sentido mismo de la vida.

List of figures

List of publications

Published

Z. Ni*, B. Xu*, **M. Á. Sánchez-Martínez**, Y. Zhang, K. Manna, C. Bernhard, J. W. F. Venderbos, F. de Juan, C. Felser, A. G. Grushin, L. Wu, "Linear and nonlinear optical responses in the chiral multifold semimetal RhSi", *npj Quantum Mater.* 5, 96 (2020).

B. Xu*, Z. Fang*, **M. Á. Sánchez-Martínez***, J. W. F. Venderbos, Z. Ni, T. Qiu, K. Manna, K. Wang, J. Paglione, C. Bernhard, C. Felser, E. J. Mele, A. G. Grushin, A. M. Rappe, L. Wu, "Optical signatures of multifold fermions in the chiral topological semimetal CoSi", *Proceedings of the National Academy of Sciences* 202010752 (2020).

M.-Á. Sánchez-Martínez*, I. Robredo*, A. Bidaurrazaga, A. Bergara, F. de Juan, A. G. Grushin, and M. G. Vergniory, "Spectral and optical properties of $Ag_3Au(Se_2,Te_2)$ and dark matter detection", *J. Phys. Mater.* **3** 014001 (2019).

M.-Á. Sánchez-Martínez, F. de Juan, and A. G. Grushin, "Linear optical conductivity of chiral multifold fermions", *Phys. Rev. B* **99**, 155145 (2019).

*Equally contributing authors

Preprints

B. Lu*, S. Sayyad*, **M. Á. Sánchez-Martínez**, K. Manna, C. Felser, A. G. Grushin, D. Torchinski, "Suppression of second-harmonic generation from linear bands in the topological multifold semimetal RhSi", *arXiv:2102.07416* (2021).

List of abbreviations

ARPES — Angle-resolved photoemission spectroscopy

BPGE — Bulk photogalvanic effect

CPGE — Circular photogalvanic effect

CVT — Chemical vapor transport

DFT — Density functional theory

FTIR — Fourier transform infrared

HME — Helical magnetic effect

JDOS — Joint density of states

LPGE — Linear photogalvanic effect

SG — Space group

SHG — Second-harmonic generation

SOC — Spin-orbit coupling

TRIM — Time-reversal invariant momentum

Linear and nonlinear optical responses of chiral multifold semimetals

Abstract

Since the initial predictions for the existence of Weyl fermions in condensed matter, many different experimental techniques have confirmed the existence of Weyl semimetals. Among these techniques, optical responses have shown a variety of effects associated with the existence of Weyl fermions, such as the linear frequency dependence of the optical conductivity and the quantized circular photogalvanic effect. In chiral crystals we find a new type of fermions protected by crystal symmetries — the chiral multifold fermions — that can be understood as a higher-spin generalization of Weyl fermions.

In the first part of this thesis, we provide a complete description of all chiral multifold fermions, studying their topological properties and the $k \cdot p$ models describing them. We compute the optical conductivity of all chiral multifold fermions and establish their optical selection rules. We find that the activation frequencies are different for each type of multifold fermion, and thus constitute an experimental fingerprint for each type of multifold fermion. Additionally, we find that the optical conductivity of threefold and fourfold fermions are up to four times larger than that of a Weyl fermion per node, given the same Fermi velocity.

Building on the theoretical results obtained from the previous analysis, we study two chiral multifold semimetals: RhSi and CoSi. We analyze the experimental results with $k \cdot p$ models and tight-binding models based on the crystal symmetries of the material. We trace back the features observed in the experimental optical conductivity to the existence of multifold fermions near the Fermi level and estimate the chemical potential and the scattering lifetime in both materials. Additionally, our analysis of the optical conductivity of CoSi indicates the existence of a spin-3/2 fourfold fermion near the Fermi level, constituting the first example of a spin-3/2 quasiparticle excitation in a crystal.

In the last part, we study the second-harmonic generation of RhSi. We analyze the experimental results using a second-order $k \cdot p$ Hamiltonian and compare our results with density functional theory calculations. We find a sizeable second-harmonic response in the low-energy regime. However, this regime is extremely challenging to access with the current experimental techniques. The density functional theory calculations reproduce the reported experimental data reasonably well, allowing us to trace back the features observed in the second-harmonic generation to different optical transitions.

Finally, we present the main conclusions of our research and motivate further studies based on the work presented in this thesis: first, understanding better chiral multifold semimetals and their responses; second, we propose to apply the analysis of optical responses developed in this thesis to different materials, such as topological superconductors. This thesis highlights the need to develop a package to compute linear and nonlinear optical responses of different models based on the codes developed during our research.

Réponses optiques linéaires et non linéaires des semi-métaux chiraux multifolds

Résumé

Depuis les prédictions initiales de l'existence de fermions de Weyl dans la matière condensée, de nombreuses techniques expérimentales différentes ont confirmé l'existence de semi-métaux de Weyl. Parmi ces techniques, les réponses optiques ont montré une variété d'effets associés à l'existence de fermions de Weyl, tels que la dépendance linéaire en fréquence de la conductivité optique et l'effet photogalvanique circulaire quantifié. Dans les cristaux chiraux, nous trouvons un nouveau type de fermions protégés par des symétries cristallines — les fermions chiraux multifolds — qui peuvent être compris comme une généralisation à spin supérieur des fermions de Weyl.

Dans la première partie de cette thèse, nous proposons une description complète de tous les fermions chiraux multifolds, en étudiant leurs propriétés topologiques et les modèles $k \cdot p$ les décrivant. Nous calculons la conductivité optique de tous les fermions chiraux multifolds et établissons leurs règles de sélection optique. Nous trouvons que les fréquences d'activation sont différentes pour chaque type de fermion multifold, et constituent ainsi une empreinte expérimentale de chaun de leurs types. De plus, nous trouvons que la conductivité optique des fermions triples et quadruples est jusqu'à quatre fois supérieure à celle d'un fermion de Weyl par nœud, étant donné la même vitesse de Fermi.

Sur la base des résultats théoriques obtenus à partir de l'analyse précédente, nous étudions deux semi-métaux chiraux multifolds : RhSi et CoSi. Nous analysons les résultats expérimentaux avec des modèles $k \cdot p$ et des modèles de tight-binding fondés sur les symétries cristallines du matériau. Nous lions les caractéristiques observées dans la conductivité optique expérimentale à l'existence de fermions multifolds près du niveau de Fermi et estimons le potentiel chimique et la durée de vie de diffusion dans les deux matériaux. De plus, notre analyse de la conductivité optique du CoSi indique l'existence d'un fermion quadruple de spin-3/2 près du niveau de Fermi, constituant le premier exemple de quasiparticule de spin-3/2 dans un cristal.

Dans la dernière partie, nous étudions la génération de deuxième harmonique de RhSi. Nous analysons les résultats expérimentaux en utilisant un hamiltonien $k \cdot p$ du second ordre et comparons nos résultats avec les calculs de la théorie de la fonctionnelle de la densité. Nous trouvons une réponse de seconde harmonique importante dans le régime de basse énergie. Cependant, ce régime est extrêmement difficile d'accès avec les techniques expérimentales actuelles. Les calculs de la théorie fonctionnelle de la densité reproduisent raisonnablement bien les données expérimentales rapportées, ce qui nous permet de relier les caractéristiques observées de la génération de la deuxième harmonique à différentes transitions optiques.

Finalement, nous présentons les principales conclusions de notre recherche et motivons d'autres études fondées sur les travaux présentés dans cette thèse : premièrement, mieux comprendre les semi-métaux chiraux multifolds et leurs réponses ; dans un deuxième temps, nous proposons d'appliquer l'analyse des réponses optiques développées dans cette thèse à différents matériaux, tels que les supraconducteurs topologiques. Cette thèse met en évidence la nécessité de développer un package pour calculer les réponses optiques linéaires et non linéaires de différents modèles à partir des codes développés au cours de nos recherches.

1

Introduction

When we think about condensed matter physics and how it has evolved, we can go all the way back to the early years of civilization. As kids we study the changes in society according to its technology and its access to materials and knowledge. However, as interesting as History is, we do not need to go to the dawn of society to witness a revolution in the way we think of materials.

In 1902 Albert A. Michelson said[1] *"it seems probable that most of the grand underlying principles have been firmly established ... An eminent physicist remarked that the future truths of physical science are to be looked for in the sixth place of decimals"*. Only three years later Albert Einstein published four papers about the photoelectric effect[2], the Brownian motion[3], the theory of special relativity[4], and the energy-mass equivalence[5], a prelude of the change of paradigm in physics during the first half of the 20th century[6].

As with the lack of evidence of the revolution to come at the turn of the 20th century, before 1980 the hints for the existence of topological phases of matter were absent in physics. In 1980 Klaus von Klitzing measured the Hall voltage of a silicon metal-oxide-semiconductor field effect transistor, showing that the Hall resistance is exactly quantized in units of h/e^2[7*]. This discovery is considered to be the first experimental milestone that put topological phenomena under the spotlight of physicists across different areas of research. The observation of this phenomenon constitutes a great success: a physical observable that can be measured without too much complication — the electrical resistance — that is quantized independently of details of the material under investigation, such as purity or size of the sample. In the 41 years that separate von Klitzing's experiment and this thesis, the

*K. von Klitzing measured the samples developed by M. Pepper and G. Dorda while working in the high magnetic field laboratory in Grenoble. Five years later he was awarded the Nobel prize for this finding.

landscape of topological phases has grown extraordinarily. Both the number of observed topological phenomena and our understanding of the underlying principles has expanded remarkably, adding a whole new dimension to the already rich realm of condensed matter physics. This — the study of topological phases — is the context of this thesis.

In my training as a physicist I have had the opportunity to discuss different points of view about our subject of study. As a theoretical physicist I have learned that physics is an experimental science, and thus the experiment plays a fundamental role in what we *actually* know and understand about reality. In the ample landscape of topological phases of matter, beyond the exciting and extremely interesting foundations, a crucial aspect to consider as theoreticians are the signatures of topological phases of matter in experimental measurements. Thus, understanding experiments will be central to this thesis.

One aspect I find particularly interesting of topological phases of matter is how they realize concepts imported from the realm of high-energy physics. One of these cross-pollinations between high-energy and condensed matter physics are Weyl fermions. Weyl fermions exist as low-energy quasiparticle excitations in three-dimensional crystals without time-reversal symmetry, inversion symmetry, or both. They, however, have not been discovered as fundamental particles. In the next chapter we will provide a more detailed explanation of what is a Weyl crossing and how to derive its topological properties. For now, we can work with the basic idea of what a Weyl semimetal is: a material that features a topological twofold crossing near the Fermi level.

1.1 Experimental signatures of topological metals

In a Weyl semimetal, the low-energy spin-1/2 quasiparticles emerging near the Weyl crossings are described by a Weyl Hamiltonian of the form[8] $H = \pm v_F \mathbf{k} \cdot \boldsymbol{\sigma}$, where v_F is the Fermi velocity, $\mathbf{k}$ is the crystalline momentum, and $\boldsymbol{\sigma}$ is a vector containing the three spin-1/2 Pauli matrices. The bands arising from this Hamiltonian disperse linearly with energy $E = \pm v_F |\mathbf{k}|$ (see Fig. 1.1 (a)). The crossing of two non-degenerate bands is special because the Weyl crossings act as

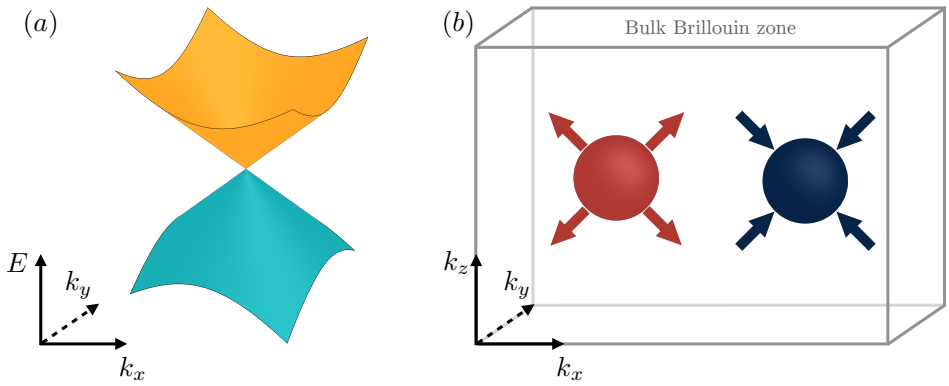

Figure 1.1: Schematic of the Weyl cone dispersion and Berry curvature. (a) Band dispersion for a fixed k_z near the Weyl crossing. The bands are linear, given by the energies $E = \pm v_F|\mathbf{k}|$ of the Weyl Hamiltonian $H = \pm v_F \mathbf{k} \cdot \boldsymbol{\sigma}$. (b) Each Weyl fermion in the Brillouin zone acts as a monopole of Berry curvature $\Omega(\mathbf{k})$. Depending on the chirality of the Weyl fermion, it can act as a source (red sphere) or a drain (blue sphere) of Berry curvature in the Brillouin zone. The Nielsen-Ninomiya theorem forces Weyl fermions to appear in pairs of opposite chirality, leading to a net vanishing chirality in the Brillouin zone.

monopoles — sources and drains — of Berry curvature[9] $\Omega(\mathbf{k})$ in the Brillouin zone (see Fig. 1.1 (b)), as we will see in Chapter 2. The Berry curvature is analogous to a magnetic field in momentum space, and the Weyl nodes act as monopoles of this magnetic field in momentum space. Thus, the only way to open a gap is to make two Weyl nodes interact, for example by bringing them closer to each other in momentum space, which is the origin of the robustness of the Weyl crossings against small perturbations in the material.

In 2D materials that break time-reversal symmetry, the Berry curvature gives rise the aforementioned quantum Hall effect. In Weyl semimetals that break time-reversal symmetry, the Hall effect features a contribution coming from the topological charge of Weyl monopoles[10]. Nevertheless, most Weyl semimetals discovered so far are non-magnetic and preserve time-reversal symmetry, which implies that the anomalous Hall conductivity is identically zero. It is thus necessary to rely on different probes to study the topological properties of Weyl semimetals.

1.1.1 ARPES and the discovery of Weyl semimetals

Different experiments have contributed to probe the existence of topological crossings in materials. The angle-resolved photoemission spectroscopy (ARPES) technique has provided very useful information about the band structure of different topological materials. This technique measures the single particle spectral function as a function of energy and momentum[11]. When the materials under investigation are weakly interacting, which is the case for most topological compounds[8], this technique gives a direct measure of their band structure. This technique played a central role in the identification of topological insulator surface states[12], and it has proven to be equally useful in identifying topological semimetals like Na_3Bi[13,14] and Cd_3As_2[15–19†].

The first prediction of a material hosting Weyl fermions was the family of pyrochlore iridates, $R_2Ir_2O_7$, where R is a rare earth[20,21]. This type of material was predicted to feature an anti-ferromagnetic behavior that breaks time-reversal symmetry, allowing the existence of Weyl crossings. Nevertheless, the magnetic order described for that type of material is still under debate in experiments[22,23], and to this date no ARPES measurements of these systems have been reported. A series of proposals followed this initial work, including a superlattice consisting of a stack of alternating thin films of a topological insulator and a normal ferromagnetic insulator[24], and the natural ferromagnet $HgCr_2Se_4$[25]. No experimental measurements to this date have reported a successful measurement indicating the existence of Weyl crossings in either of these systems.

The breakthrough took place in 2015, when different works predicted and confirmed the existence of Weyl crossings in TaAs[26–29] (see Fig. 1.2). This material has a body-centered tetragonal lattice and crystallizes in the space group 109 in a lattice that lacks inversion symmetry, a key feature for hosting Weyl fermions. The Weyl fermions in the bulk Brillouin zone of TaAs, together with the corresponding Fermi arcs, have been directly observed by ARPES measurements[28–30], providing

†ARPES measurements initially indicated that Cd_3As_2 was a Dirac semimetal. Later, magneto-optic measurements in this material showed that the conical features observed in the band structure, originally attributed to Dirac fermions, correspond to massless Kane electrons, and that the Dirac electrons may appear only at smaller energy scales[19].

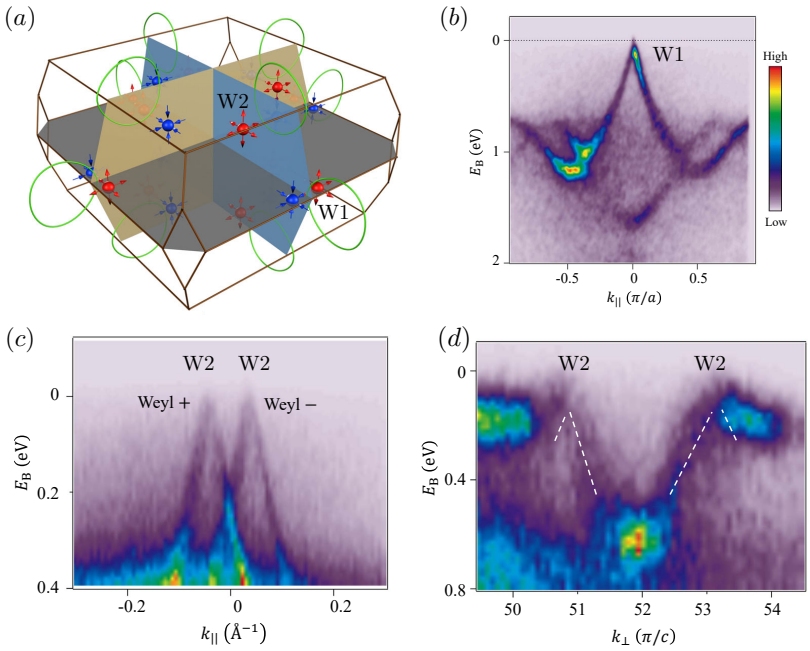

Figure 1.2: Weyl cones in the bulk Brillouin zone of TaAs. (a) In the absence of spin-orbit coupling, TaAs hosts nodal rings in the k_x and k_y mirror planes. When spin-orbit coupling is included, the nodal rings are gapped except at 12 pairs of Weyl crossings with opposite chirality (red and blue spheres) off the mirror planes: 8 Weyl points on the $k_z = 0$ plane, referred to as $W1$, and 16 Weyl points away from the $k_z = 0$ plane, referred to as $W2$. (b) ARPES in-plane energy dispersion $(E_B, k_{||})$ that goes through a $W1$ Weyl node. A linear dispersion is clearly observed, consistent with the Weyl fermion cone. (c) ARPES in-plane energy dispersion $(E_B, k_{||})$ that goes through a pair of $W2$ Weyl nodes. (d) ARPES out-of-plane energy dispersion $(E_B, k_\perp)$ that goes through two $W2$ Weyl nodes with the same k_x, k_y but different k_z value. Adapted from Refs. [27,28].

the first indications of the presence of Weyl fermions in a crystal[‡]. These measurements were complemented with spectroscopy measurements in different compounds in the TaAs family[26–30,32–42], providing further evidence of the existence of Weyl fermions in this class of materials.

[‡]A Weyl band structure was observed also in 2015 in an inversion-breaking 3D double-gyroid photonic crystal without breaking time-reversal symmetry[31].

1.1.2 The chiral anomaly and negative magnetoresistance of Weyl semimetals

The presence of Weyl fermions in a system has physical consequences beyond its band structure. Each Weyl node in a condensed matter system has a positive or negative chirality corresponding to the sign of the determinant of the velocity matrix, and determines whether the Weyl node acts as a source (positive chirality) or drain (negative chirality) of Berry curvature. Thus, a single Weyl fermion — *i.e.,* a single monopole — is not periodic in the Brillouin zone. The Nielsen-Ninomiya theorem establishes that Weyl fermions in condensed matter realizations must appear in pairs of opposite chirality to have a net zero topological charge[43]. This means that, in equilibrium, two Weyl nodes at the same energy with opposite chirality will yield a net zero chiral-dependent current, making the chirality of each Weyl node unobservable.

Although Weyl fermions appear in pairs of opposite chirality, it is possible to induce a steady-state density difference between both chiralities in the presence of parallel electric ($\mathbf{E}$) and magnetic ($\mathbf{B}$) fields proportional to $\mathbf{E} \cdot \mathbf{B}$[8]. The density imbalance between both chiralities results in a current $j \propto \tau B \mathbf{E} \cdot \mathbf{B}$, where τ is the inter-node scattering time. This current is a manifestation of the chiral anomaly in condensed matter realizations, originally predicted for Weyl fermions in high-energy physics[43]. Along the magnetic field direction, the conductivity increases proportionally to B^2, leading to a negative magnetoresistance[44,45]. Typically, metals or conventional semiconductors have a weak positive magnetoresistance that does not depend strongly on the magnetic field direction. Thus, the negative magnetoresistance could be used as a signature of Weyl fermions.

Typical measurements of the magnetoresistance involve measuring the voltage drop between two points in a sample, where an electric current is injected through metallic contacts. When the size of the contacts is smaller than the cross section of the sample, a magnetic field applied to the sample can enhance the electric current parallel to the magnetic field direction. Since we expect to observe the negative magnetoresistance characteristic of Weyl semimetals along the direction of the magnetic field, we need to measure the voltage drop along

this same direction, where the current is potentially enhanced by the magnetic field. The enhancement of the electric current along the magnetic field is known as current jetting[46–50], and can lead to an apparent negative magnetoresistance not originated by Weyl fermions[51]. Current jetting can therefore mask the signatures of Weyl fermions in magnetotransport, an extrinsic effect that is challenging to rule out.

1.1.3 Optical responses as probes for topological phases

The options for detecting experimentally the presence of Weyl fermions are not limited to observing directly their band structure or their DC electrical transport. When an incident electric field interacts with a material, the material reacts by inducing a current density proportional to the incident field. Assuming the electric field is a continuous wave with a wavelength larger than the material sample, we can neglect the spatial dependence of the electric field and express the induced current in powers of the electric field as

$$j_a(t) = \sum_b \sigma^{(1)}_{ab} E_b(t) + \sum_{bc} \sigma^{(2)}_{abc} E_b(t) E_c(t) + \cdots . \tag{1.1}$$

The quantities $\sigma^{(1)}_{ab}$ and $\sigma^{(2)}_{abc}$ are the linear and second-order conductivity tensors, respectively.

Let us start by considering linear responses $\sigma^{(1)}_{ab}$. An interesting example is the optical conductivity of graphene, a two-dimensional semimetal featuring Dirac cones at the K and $K^{'}$ points of the Brillouin zone. For interband transitions near the Dirac degeneracy, the optical conductivity of graphene has a universal value $\sigma_0 = e^2/(4\hbar)$, resulting in a frequency-independent transmission quantized in terms of the fine-structure constant $\alpha = e^2/\hbar c \approx 1/137$ as $T = 1 - \pi\alpha$[52–54]. In Weyl semimetals we can consider the low-energy limit, when higher-order terms in the dispersion can be neglected. In the absence of impurities and interactions, the result that arises from interband transitions across the Weyl node when the chemical potential is placed exactly at the Weyl degeneracy is the non-universal optical conductivity $\sigma(\omega) = N\omega e^2/(12hv_F)$, where v_F is the Fermi velocity and N is the number of nodes[24,55–57].

In non-interacting electron systems consisting of two bands that meet at the Fermi energy, which can describe generically an untilted Weyl crossing, the optical conductivity has the power-law frequency dependence $\sigma \propto \omega^{(d-2)/z}$, where d is the spatial dimensionality of the system and z is the power law of the band dispersion[58]. In graphene ($d = 2$), the linear dispersion of the bands ($z = 1$) near the K and K' points results in the constant optical conductivity σ_0 mentioned in the previous paragraph. In the case of Weyl semimetals ($d = 3$), the linear dispersion ($z = 1$) characterizing the topological bands near the Weyl crossings leads to the linear scaling ($\sigma \propto \omega$) of the optical conductivity with incident frequency.

However, the features of the optical conductivity associated with the presence of Weyl crossings in the material can be significantly affected by the position of the Fermi level and the sample disorder. It is thus necessary to have a good estimation of these quantities to interpret the experimental measurements of optical responses correctly. This endeavor will be central to this thesis.

Let us consider now the second-order response $\sigma^{(2)}_{abc}$ of a material to a monochromatic source with frequency ω. Since the second-order response is proportional to the second power of the electric field, the two Fourier components of the field $+\omega$ and $-\omega$ can interfere constructively or destructively. This interference results in different effects that can be used to probe different material properties (see Fig. 1.3).

In Weyl semimetals some nonlinear optical responses can be directly linked to the topological charge of Weyl fermions[59–65]. In inversion-breaking Weyl semimetals we can find second-order optical responses that provide valuable information about the topological charge of the Weyl crossings and the geometric properties of their bands, such as the variation of Berry curvature with the crystalline momentum.

Let us first consider the destructive interference of two incident electric fields with frequency ω, which results in a second-order DC ($\omega = 0$) response. One of the responses linked to the topological properties of Weyl semimetals is the circular photogalvanic effect (CPGE), associated with the second-order DC ($\omega = 0$) response to circularly polarized light. The optical selection rules for circularly polarized light result in asymmetric excitation probabilities within a single Weyl cone[63] (see

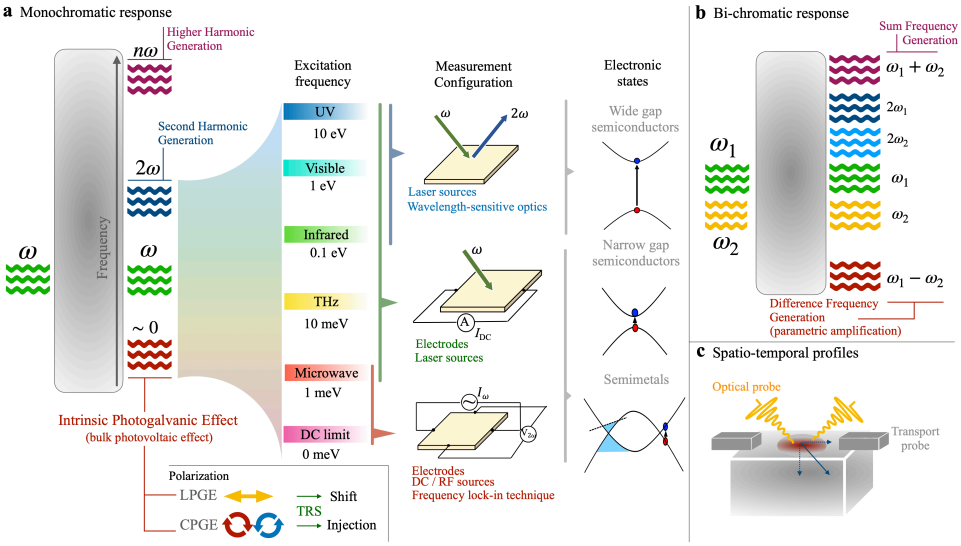

Figure 1.3: Overview of second-order nonlinear processes. (a) A monochromatic electric field at frequency ω applied to a material that lacks inversion symmetry can induce a 2ω response in the material, known as second-harmonic generation, and a DC current know as the instrinsic photogalvanic effect. Depending on the polarization of the incident light, the effect is known as the linear or circular photogalvanic effect for linear and polarized light, respectively. Depending on the frequency, the responses induced in the material can be measured with different probes, from all electric in the DC limit to all-optical for higher frequencies. (b) When the source is not monochromatic, electric fields of two frequencies $\omega_{1,2}$ can induce responses in the material at the sum or difference of their frequencies, known as sum or difference frequency generation, respectively, as well as the second-harmonic responses for each of the incident frequencies at $2\omega_{1,2}$. (c) Nonlinear photocurrents can be measured by capturing the carriers with metallic contacts or via an emitted pulse whose electric field can be detected in the far field. Reproduced from Ref. [59].

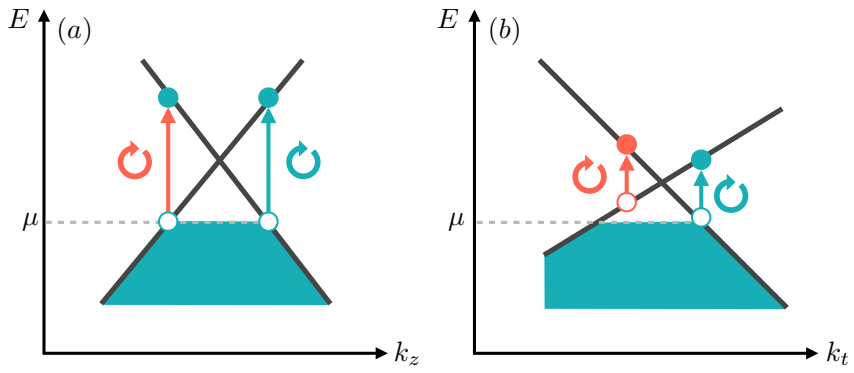

Figure 1.4: Optical excitations for circularly polarized light in tilted Weyl fermions. Occupied states below $E = \mu$ are indicated in blue. (a) Asymmetric excitations in a single Weyl cone. Circularly polarized light will excite electrons from only one side of the cone (blue arrow), while the transition in the opposite side is forbidden (red arrow) (b) In a tilted Weyl cone along the tilt direction k_t optical transitions at a given energy (blue arrow) are Pauli blocked in the opposite side of the cone (red arrow and circles).

Fig. 1.4 (a)), producing a nonzero current. However, as we mentioned in Sec. 1.1.2, the Nielsen-Ninomiya theorem forces Weyl cones to appear in pairs with opposite chirality. Weyl cones with opposite chirality contribute with opposite signs to the total current, meaning that if both chirality-opposed Weyl fermions have the same band dispersion the net current is zero. This situation can be overcome in systems with tilted Weyl cones, which is the natural situation for Weyl cones placed outside high-symmetry points in the Brillouin zone[63,64]. In this case, the optical excitations are asymmetric for different sides of a single cone. Additionally, placing the chemical potential away from the node prevents optical transitions within the Pauli-blocked region, leading to additional asymmetries in the contributions from different sides of the cone (Fig. 1.4 (b)). This combination of Pauli-blocking and optical selection rules has led to the observation of non-zero photocurrent generation[63,65].

In inversion-symmetry breaking Weyl semimetals, the variation of the Berry curvature $\Omega(\mathbf{k})$ with the crystalline momentum — the Berry dipole $\partial_k\Omega(\mathbf{k})$ — determines the strength of the CPGE[10,60,61]. The effect is, thus, generically not quantized. However, in Weyl semimetals, at nonzero frequency there is a quantization of the rate of the CPGE[62] determined by the topological charge of the Weyl crossing in units of

$e^3/\hbar^2$. It is rather unusual to find a quantized observable in a metallic system, and the CPGE in Weyl semimetals constitutes a remarkable example of a nonlinear optical response that provides a direct way of measuring the topological charge of Weyl crossings.

Turning to the constructive interference of frequencies at second order we find the second-harmonic generation (SHG). In this case, the two oscillating incident electric fields with frequency ω interfere constructively to generate a response in the material at 2ω. The second-harmonic response of a Weyl semimetal is not quantized, and its relation to the topological and geometrical properties of the band structure is still a matter of study. This response has been measured in TaAs in the energy range from 0.5 eV to 1.5 eV[66,67], revealing a giant second-harmonic response at room temperature with a resonance at 0.7 eV[68]. The giant second-harmonic response of the first discovered Weyl semimetal raised the question of whether this enhancement was mainly due to the topological nature of the Weyl crossings present in TaAs. However, the energy scale explored in the experiments ($\sim$eV) is considerably larger than the interband energy excitations near the Weyl node ($\sim$meV), thus involving non-Weyl bands in the response. The added contribution of different bands poses a challenge when aiming to determine the topological or trivial origin of the giant second-harmonic response. First-principles calculations of a wide range of crystals found that in most materials the Weyl fermions are very close together in momentum space, typically leading to short Fermi arcs and narrow topologically non-trivial energy windows[8,10,69]. Moreover, predicted band structures often exhibit a very large number of Weyl fermions scattered throughout the bulk Brillouin zone with Weyl fermions that lie far from the Fermi level as well as irrelevant trivial electron bulk and surface states at the Fermi level[8,10,69]. All these factors question the enhancement of the second-harmonic response from topological bands. In this thesis we will study the second-harmonic response of topological semimetals exhibiting a large energy window where only topological bands are involved.

Along with the interesting phenomena observed in optical responses of Weyl fermions, for excitation frequencies between the infrared ($\sim$0.1 eV) and the UV ($\sim$ 10 eV), experiments can be performed in a completely contactless fashion (see Fig. 1.3), which can be an advantage compared to transport probes. This energy range is especially relevant for the

optical conductivity and second-harmonic responses studied in this thesis. Expanding the energy scope down to the microwave (∼1 meV) regime, the measurements can be performed applying a laser source to the sample and measuring the induced current with the help of electrodes. Finally, for DC excitation frequencies (0 meV) one must rely on DC sources and electrodes to measure the current.

The scenario described here is significantly enriched when we consider bi-chromatic responses. Under this assumption we find two initial frequencies ω_1 and ω_2 that can be combined in different ways to give rise to a larger variety of responses (see Fig. 1.3 (b)). A detailed review of monochromatic and bi-chromatic nonlinear responses in topological materials can be found in Ref. [59].

1.2 Beyond Weyl crossings: multifold fermions

In the previous section we relied on time-reversal and inversion symmetry breaking as the requirements for a material to host the twofold band degeneracies giving rise to Weyl quasiparticle excitations. However, it is reasonable to ask if we can rely on a different set of symmetries to find other degenerate band crossings. In 2016 Bradlyn *et al*[70] studied what type of crossings can exist in different crystal structures analyzing all possible non-magnetic space groups. We can find two-, three-, four-, six-, and eightfold band degeneracies in different crystal structures[70,71] protected by the crystal symmetries. The low-energy quasiparticles emerging near these band degeneracies are described by a generalization of the Weyl equation with higher spin $H = v_F \mathbf{k} \cdot \mathbf{S}$, and we refer to them as multifold fermions. These quasiparticles do not have a high-energy counterpart in the traditional classification of fermions, and were originally referred to as *unconventional fermions*[70]. Out of all possibilities, only two-, three-, four-, and sixfold fermions are chiral, in the sense that they have a nonzero topological charge and act as sources of Berry curvature in the momentum space. These are central to this thesis and will be described in detail in Chapter 2.

The development of the theory of multifold fermions led to the prediction of a near-ideal chiral multifold semimetals family, the AB

material class with $A = \mathrm{Co}, \mathrm{Rh}$ and $B = \mathrm{Si}, \mathrm{Ge}$[70,72,73]. These materials crystallize in the cubic chiral space group 198. Their band structure features multifold fermions at the zone center and at the zone corner, achieving the largest momentum-space separation possible between two chiral charges in the Brillouin zone. This new class of materials opens exciting possibilities to study the effect of fermions with higher topological charges than Weyl fermions in optical responses. Unlike previous Weyl candidates, in these new materials the topological band crossings are well isolated in the Brillouin zone and separated in energy from trivial bands. This potentially allows us to trace back the features observed in the experimental measurements to the presence (or absence) of topological bands extending over a wide range of energies. Additionally, two of these materials, RhSi and CoSi, have been synthesized as single crystals, an advantage to grow clean enough samples where the effect of the chiral multifold crossings is not masked by disorder effects.

In this thesis we will study the linear and nonlinear responses of chiral multifold fermions. We will review the classification of chiral multifold fermions, describing their topological properties. Our main focus are the optical fingerprints of these multifold band degeneracies in materials hosting them. To study these fingerprints, we will rely on different models of increasing order of complexity: $k \cdot p$ Hamiltonians for each type of chiral multifold fermions and tight-binding models incorporating the crystal symmetries of the materials under study. We will compare the results obtained for the $k \cdot p$ and tight-binding models with density functional theory (DFT) calculations providing specific band structures for each material, which will allow us to examine the limitations of the simpler models. Finally, we will analyze and provide a comprehensive understanding of the linear optical conductivity in RhSi and CoSi, and address the question of the effect of topology in the second-harmonic generation of RhSi.

In this chapter we have provided an introduction to the experimental detection of Weyl semimetals, which can be considered the lowest-degeneracy case of a chiral multifold semimetal. We gave an overview of the linear and nonlinear responses that can emerge in Weyl systems, making special emphasis on the properties and experimental accesibility of nonlinear responses.

In Chapter 2 we provide a complete description of all chiral multifold fermions, studying their topological properties and the different models of increasing order of complexity that we will use throughout this thesis. We start with the simplest case, the twofold (Weyl) fermion, providing an introduction to the topological quantities that characterize it and their physical consequences. We extend this analysis to all chiral multifold fermions, and provide a relation of the Brillouin zone positions where they can appear in all chiral space groups.

In Chapter 3 we derive a general expression for the optical conductivity, and use it to compute the optical conductivity of all chiral multifold fermions using low-energy $k \cdot p$ Hamiltonians, identifying characteristic fingerprints for each type of multifold fermion. Finally, we compute the optical conductivity of two tight-binding models capable of describing real materials crystallizing in space groups 198 and 199. We analyze the main characteristics and trace back the features of the optical conductivity of these models to the presence of multifold crossings in their band structure.

In Chapter 4 we model two experiments measuring the optical conductivity of RhSi and CoSi, both materials crystallizing in SG198 and featuring multifold crossings near the Fermi level with a relatively large topological energy window. We characterize their optical conductivity using different models, and provide the first evidence for the existence of a spin-3/2 quasiparticle excitation in a crystal. The study of CoSi presented in this chapter is the result of a collaboration with Bing Xu, Christian Bernhard, and Liang Wu, who worked on the experiment, and Zhenyao Fang, Jorn Venderbos, Tian Qiu, Eugene Mele, and Andrew M. Rappe, who worked on the ab-initio calculations. The results discussed here were presented in Ref. [74]. The results for

RhSi have been obtained in collaboration with Zhuoliang Ni, Bing Xu, Yang Zhang, Kaustuv Manna, C. Bernhard, Jorn W. F. Venderbos, Fernando de Juan, Claudia Felser, and Liang Wu, and were originally presented in Ref. [75].

In Chapter 5 we study the second-harmonic generation of RhSi. We analyze the experimental results by using a second-order $k \cdot p$ Hamiltonian and DFT calculations, providing a comprehensive description of the origin of the different features in the second-harmonic response and their relation to the topological character of the bands in RhSi. This study was done in collaboration with Baozhu Lu, Kaustuv Manna, Claudia Felser, and Darius H. Torchinsky, who worked on the experiment, and Sharareh Sayyad, who performed the DFT calculations, and was originally presented in Ref. [76].

In Chapter 6 we state the conclusions of our research of linear and nonlinear optical responses of chiral multifold fermions, with emphasis in the materials RhSi and CoSi. Finally, we provide future directions for the study of chiral multifold semimetals and important applications of nonlinear responses to other families of materials.

2

Chiral multifold fermions

In my last year as an undergraduate student, the teacher of the elementary particle physics course came into the room and asked us: "*if you contact an alien very far away in space, what would you ask them to know if they are made of matter or antimatter?*". Of course, at that moment I did not know that this question is known as the Ozma problem. The answer lies in the neutral kaon K^0 decay and the violation of CP symmetry. Both the kaon K^0 and anti-kaon $\bar{K}^0$ have a slightly lower probability to produce electrons than anti-electrons in the decay process. That day the teacher explained the relevance of CP symmetry and the full symmetry of the Standard Model. It was one of my first exposures to the almighty role of symmetries in defining* the properties of physical systems.

When studying what type of free particles we can find in nature, we can divide them into bosons and fermions. The latter can be of three types: Dirac, Weyl, and Majorana fermions. The assumption underneath the traditional classification of fermions is that these particles exist in space-time, thus respecting Poincaré symmetry. However, in condensed matter systems, fermions are not constrained by Poincaré symmetry, and a natural question arises: can we find some type of fermion in condensed matter systems that does not exist as a free particle in space-time? We know condensed matter systems predicted to host Dirac, Weyl, and Majorana excitations, but recent works[70–72,77,78] studied the possibilities of finding new quasiparticles with no high-energy counterparts in crystals. These particles, together with the Weyl fermion, are the so-called multifold fermions.

In this chapter, we will study the complete classification of multifold fermions and focus on those with a nonzero topological charge: the chiral multifold fermions. We start by the simplest possible case,

**Defining* or *explaining*, depending on your epistemological approach to natural sciences.

the well-known Weyl fermion, and we will progress through all cases, explaining their properties and constructing the corresponding low-energy k.p models describing them. We will finish by turning to candidate materials to host these multifold excitations, the multifold semimetals, and discussing the structure of two space groups where these materials can crystallize.

2.1 Weyl fermions

Weyl fermions, one of the three types of fermions in the traditional classification of particles, are chiral, massless, spin-1/2 particles governed by the Weyl equation with Hamiltonian[8]

$$H_{\text{Weyl}} = \pm v_F \mathbf{k} \cdot \boldsymbol{\sigma}, \tag{2.1}$$

where $\pm$ corresponds to the positive or negative chirality of the particle, meaning that the particle propagates with velocity v_F parallel or antiparallel to its spin[†]. In condensed matter systems, v_F corresponds to the Fermi velocity of the bands meeting at the Weyl crossing. The quantity $\mathbf{k} = (k_x, k_y, k_z)$ is the momentum of the particle and $\boldsymbol{\sigma} = (\sigma_x, \sigma_y, \sigma_z)$ is a vector containing the three Pauli matrices. The bands described by Eq. 2.1 meet at a single point, which we refer to as Weyl node (see Fig. 1.1 (a)). This degeneracy cannot be gapped out in the 2×2 matrix subspace. The only linearly-independent term that we can add is proportional to σ_0, which would result in a change of the energy position of the node, and adding any term proportional to σ_x, σ_y or σ_z can be absorbed in k_x, k_y, k_z.

For some time, the connection between the material realization of Weyl quasiparticles and their high-energy counterpart remained unclear. The physics community believed that neutrinos might be Weyl fermions. However, in 2016 the evidence of nonvanishing mass of the neutrino[79,80] discarded this possibility. At the moment of writing this thesis, there are no fundamental particles believed to be massless Weyl fermions. How did this idea of massless Weyl fermions materialize in the study

[†]The relation of parellelism or antiparallelism of the spin and the direction of propagation is called helicity. This corresponds to the chirality of the particle only in the massless cases.

of condensed matter systems? In 1937 Herring[81] noted that one could find accidental twofold band degeneracies in three-dimensional solids even with no symmetries enforcing it. The low-energy dispersion of the electrons near these degeneracies was generically linear and resembled the Weyl equation. The connection between the low-energy dispersion near the twofold degeneracies studied by Herring and the Weyl fermions described in high-energy physics solidified with the work of Nielsen and Ninomiya[82]. They realized that the chiral anomaly described for high-energy Weyl fermions could have a nontrivial effect in a lattice realization of Weyl degeneracies — such as the negative magnetoresistance discussed in Sec. 1.1.2. Finally, the term *Weyl node* for these twofold degeneracies was coined in 2011[20].

To understand many of the interesting properties of Weyl fermions in condensed matter we turn to their topological aspect. In band theory, we describe the electronic states in a crystal in terms of one-particle Bloch wave functions $|u_n(\mathbf{k})\rangle$, defined within the unit cell and labeled by the crystal momentum $\mathbf{k}$ and band index n. The first concept we need to define to describe the topological features of Weyl fermions is the Berry connection of the band n, which can be expressed as[83]

$$\mathcal{A}_n(\mathbf{k}) = i \langle u_n(\mathbf{k})| \nabla_{\mathbf{k}} |u_n(\mathbf{k})\rangle . \tag{2.2}$$

It is important to note that the Berry connection can change depending on an additional phase on the definition of $|u_\pm\rangle \to e^{i\theta_k} |u_\pm\rangle$. It is thus convenient to define a field tensor $\Omega_n(\mathbf{k})$ associated to the connection $\mathcal{A}_n$,

$$\Omega_n(\mathbf{k}) = \nabla \times \mathcal{A}_n, \tag{2.3}$$

which we refer to as Berry curvature. The Berry curvature is a gauge-invariant intrinsic property of the band structure since it exclusively depends on the wave function, providing useful information about its properties. In a similar way to the calculation of the charges enclosed by a surface in electrodynamics, here we can define the flux

of Berry curvature over a surface $S_{\mathbf{k}}$ in momentum space enclosing the degeneracy point $\mathbf{k} = 0$, given by

$$\int \Omega_{\pm}(\mathbf{k}) \cdot dS_{\mathbf{k}} \tag{2.4}$$

An extensive and more general explanation of the Berry curvature, its relation to topological features of materials, and its physical consequences can be found in Ref. [83].

To compute the monopole charge of Weyl fermions obeying the Hamiltonian in Eq. 2.1 the first quantity we need are the eigenfunctions $|u_{\pm}(\mathbf{k})\rangle$ of the Hamiltonian in Eq. 2.1, expressed in polar coordinates $\mathbf{k} = k\,(\sin\theta\cos\phi, \sin\theta\sin\phi, \cos\theta)$ as[83]

$$|u_+\rangle = \begin{pmatrix} \cos\frac{\theta}{2} e^{-i\phi} \\ \sin\frac{\theta}{2} \end{pmatrix}, \quad |u_-\rangle = \begin{pmatrix} \sin\frac{\theta}{2} e^{-i\phi} \\ -\cos\frac{\theta}{2} \end{pmatrix}. \tag{2.5}$$

It is easy to compute the components of the Berry connection (Eq. 2.2) for $|u_-\rangle$, which are

$$\mathcal{A}_-^{\theta} = \langle u_-|i\partial_{\theta} u_-\rangle = 0, \tag{2.6}$$

$$\mathcal{A}_-^{\phi} = \langle u_-|i\partial_{\phi} u_-\rangle = \sin^2\frac{\theta}{2}. \tag{2.7}$$

$$\tag{2.8}$$

With these ingredients the Berry curvature reads

$$\Omega_-(\theta,\phi) = \partial_{\theta}\mathcal{A}_{\phi} - \partial_{\phi}\mathcal{A}_{\theta} = \frac{1}{2}\sin\theta. \tag{2.9}$$

If we proceed in an analogous way for $|u_+\rangle$, we obtain the Berry curvature of the + band,

$$\Omega_+(\theta,\phi) = -\frac{1}{2}\sin\theta. \tag{2.10}$$

We can now compute the flux of Berry curvature (see Eq. 2.4) over a sphere S_2 enclosing the Weyl degeneracy for each band as

$$\int_{S^2} d\phi d\theta \Omega_{\pm}(\theta, \phi) = \mp 2\pi. \tag{2.11}$$

The Chern theorem establishes that the Berry curvature integrated over a closed surface is quantized in units of 2π. The proportionality between the Berry curvature integrated over a closed surface and 2π is given by the number of monopoles enclosed by the surface. This is a topological invariant known as the Chern number C, which indicates the charge of the monopole enclosed by the surface of integration in momentum space, and can be defined as

$$C_{\pm} = \frac{1}{2\pi} \int_{S^2} d\phi d\theta \Omega_{\pm}(\theta, \phi). \tag{2.12}$$

The topological features of the Weyl fermion come from this nonzero Chern number, which indicates that the Weyl nodes in the band structure of a crystal act as sources and drains of Berry curvature (see Fig. 1.1 (b)). In order to open up a gap, it is necessary to bring together two Weyl nodes with opposite charges. Since this procedure requires strong disorder or strain, this endows the Weyl nodes with a topological robustness against perturbations and local defects. We refer commonly to this robustness as topological stability. The topological charge of the Weyl nodes is responsible for some of the exotic properties of Weyl semimetals, the materials hosting Weyl crossings, including protected surface Fermi arcs[84] connecting nodes with opposite topological charges.

2.2 The classification of chiral multifold fermions

When we consider the symmetries of a crystal structure, we find two types of symmetries: those that leave one point invariant, the point group symmetries, and the translations in three-dimensional space, which define the 14 Bravais lattices. The combination of point group symmetries and Bravais lattices lead to 230 different possibilities, which

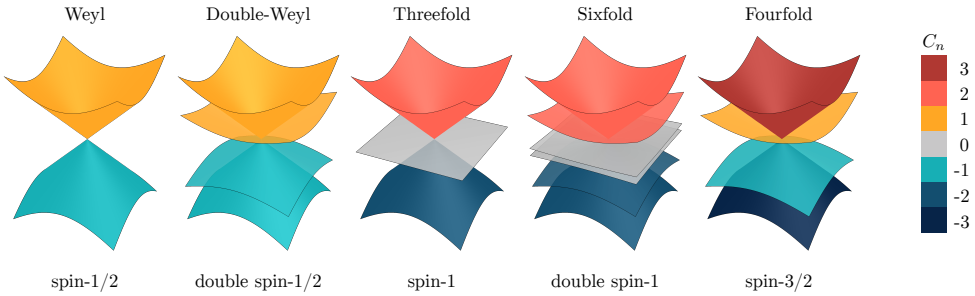

Figure 2.1: Schematic band dispersions of all chiral multifold fermions. The low-energy quasiparticles near the Weyl degeneracy have spin-1/2, and the Chern numbers of the bands are $C = 1, -1$. The double-Weyl fermion can be understood as the superposition of two Weyl fermions, which do not mix due to symmetry constraints. For the threefold fermion, the low-energy quasiparticles have spin-1, and the Chern numbers of the bands are $C = 2, 0, -2$. The sixfold fermion can be understood as the superposition of two threefold fermions that do not mix due to symmetry constraints. The low-energy quasiparticles near the fourfold crossing have spin-3/2, and the Chern numbers of the bands are $C = 3, 1, -1, -3$.

we refer to as space groups (SGs). Out of those 230 SGs, only 65 are chiral, and we refer to them as chiral space groups. In the chiral space groups, isolated point degeneracies at high-symmetry points in the Brillouin zone are generically monopoles of Berry curvature, similar to Weyl crossings. In fact, the simplest degeneracy behaving as a monopole we can find in chiral systems are Weyl nodes at a time-reversal invariant momentum[85] (TRIM) in a material with spin-orbit coupling such as Te. Additional symmetries can lead to the protection of nonlinear twofold degeneracies[86,87] or higher-fold degeneracies with higher Chern numbers. The latter are the so-called multifold fermions and are the focus of this thesis.

Multifold fermions can only exist as two-, three-, four-, six-, or eightfold degeneracies. Unlike their lower-fold partners, eightfold degeneracies cannot be assigned a nonzero Chern number and, in this sense, they are not topological. In this thesis, we will focus on two-, three-, four-, and sixfold fermions, and we will refer to them as *chiral* multifold fermions (see Fig. 2.1). However, for the sake of conciseness, we will frequently use simply the term multifold fermions.

The low-energy degrees of freedom near chiral multifold crossings of degeneracy larger than two can be described by a generalization of a Weyl Hamiltonian (see Eq. 2.1) of the form $H = -\hbar v_F \mathbf{k}\cdot\mathbf{S}_\alpha$, where $\mathbf{S}_\alpha$ is

Multifold	C_n	No So	SO
Double-Weyl (doubled spin-1/2)	$(-1, 1) \times 2$	19,92,96,198,212,213	18,19,90,92,94,96,198,212,213
Threefold (spin-1)	$-2, 0, 2$	195–199,207–214	199,214
Sixfold (doubled spin-1)	$(-2, 0, 2) \times 2$	–	198,212,213
Fourfold (spin-3/2)	$(-3, -1, 1, 3)$	–	195–199,207–214

Table 2.1: Complete classification of multifold fermions in the 65 chiral space groups. The quantity in parenthesis indicates the effective spin for the symmetric case of each multifold fermion. C_n corresponds to the Chern number of the bands (see Eq. 2.12). The last two columns list all space groups where each multifold fermion can occur with and without spin-orbit coupling. Table adapted from Ref. [71].

a vector of three matrices that depend on a material-specific parameter α. For particular values $\alpha = \alpha_0$, the matrices S_α take the rotationally symmetric form of a higher-spin representation of SU(2). In such cases, the multifold fermions have an effective spin given by $\mathbf{S}_0$.

The complete classification of chiral multifold fermions in the 65 chiral space groups, originally presented in Ref. [71], is here presented in Table 2.1. This table contains the Chern number for the bands of each type of multifold fermion, together with the space groups where each multifold fermion appears for finite and zero spin-orbit coupling.

In the remainder of this chapter, we will study each type of multifold fermion and compute the low-energy $k \cdot p$ Hamiltonians describing them. Lastly, to connect with real materials, we will study two symmetry-based tight-binding models that describe materials featuring different multifold crossings in their band structure.

2.2.1 Double-Weyl fermion

The first chiral multifold fermion in the classification presented in Table 2.1 is a fourfold degeneracy at a TRIM at the corners of the Brillouin zone when the material possesses a twofold screw axis. This axis, combined with time-reversal symmetry, can enforce a doubling of the twofold degeneracy.

When we consider finite spin-orbit coupling, a double-Weyl crossing can exist at the R and S points in space groups 18 and 19, the A and M points in space groups 90, 92, 94, and 96, and at the M point in

space groups 198, 212, and 213. If the spin-orbit coupling is zero, the double-Weyl fermion can exist at the R point in space groups 19, 198, 212, and 213, and at the A point in space groups 92 and 96.

This fourfold crossing can be understood as a superposition of two Weyl fermions with the same chirality, which means that the linear $k \cdot p$ Hamiltonian describing the degrees of freedom near this degeneracy can be brought to a block-diagonal form with a Weyl Hamiltonian in each block. As an example, the $k \cdot p$ Hamiltonian of SG90 features a double-Weyl crossing in the zone corner[71], which can be expressed as:

$$H_{2\times\text{Weyl}} = \begin{pmatrix} H_{\text{Weyl}}(\mathbf{k}, b) & 0 \\ 0 & H^*_{\text{Weyl}}(\mathbf{k}, -b) \end{pmatrix}, \tag{2.13}$$

where $H_{\text{Weyl}}(\mathbf{k}, b)$ is parametrized as

$$H_{\text{Weyl}}(\mathbf{k}, b) = \hbar v_F \begin{pmatrix} ak_z & (k_x + ik_y)(c + ib) \\ (k_x - ik_y)(c - ib) & -ak_z \end{pmatrix} \tag{2.14}$$

where a, b, and c are real numbers. This means that, generically, both Weyl fermions have a different Fermi velocity, and do not overlap completely (see Fig. 2.1).

The existence of double-Weyl fermions was known for some space groups[70,85,88], but the full classification of double-Weyl fermions was introduced in Ref. [71]. For a more detailed description of the construction of the low-energy $k \cdot p$ and the symmetries involved in the example for SG90 see Appendix G of Ref. [71].

This decomposition implies that it is not necessary to consider explicitly the double-Weyl Hamiltonian in the calculation of observables using the linear $k \cdot p$ models. Instead, we will use our calculations for the Weyl fermion to obtain the result for the double-Weyl case as an addition of two separated Weyl fermions.

2.2.2 Threefold fermion

So far, we have only considered the Weyl fermion and a superposition of two Weyl fermions. The next multifold degeneracy we consider here is a threefold crossing. Unlike the Weyl fermion, this provides the first case of a new quasiparticle in crystals with no high-energy counterpart. This degeneracy can happen at the Γ point of space groups 195–199,207–214, the H point in space groups $199, 211$, the R point in space groups $195, 207$, and 208, and the P point in space groups 197 and 211 without spin-orbit coupling. For finite spin-orbit coupling, we can find this threefold crossing at the P and $-P$ points of space groups 199 and 214.

The Berry curvature of the threefold fermion corresponds to that of a spin-1 moment in a magnetic field[9]. The most general Hamiltonian describing a threefold fermion is[70,71]

$$H_{3f}(\mathbf{k},\phi) = \hbar v_F \begin{pmatrix} 0 & \mathrm{e}^{\mathrm{i}\phi}k_x & \mathrm{e}^{-\mathrm{i}\phi}k_y \\ \mathrm{e}^{-\mathrm{i}\phi}k_x & 0 & \mathrm{e}^{\mathrm{i}\phi}k_z \\ \mathrm{e}^{\mathrm{i}\phi}k_y & \mathrm{e}^{-\mathrm{i}\phi}k_x & 0 \end{pmatrix}, \tag{2.15}$$

where v_F is the Fermi velocity and ϕ is a material-dependent parameter[70,71].

In the absence of spin-orbit coupling the value of ϕ is constrained to be $\phi_0 = \pi/2 \mod (\pi/3)$[77]. For $\phi = \phi_0$ the Hamiltonian takes the form $H_{3f}^{\phi_0}(\mathbf{k}) \equiv H_{3f}(\mathbf{k},\phi_0) = \hbar v_F \mathbf{k}\cdot\mathbf{S}_1$, where $\mathbf{S}_1 = (S_{1,x}, S_{1,y}, S_{1,z})$ is a vector of three spin-1 matrices which form a representation of SU(2)

$$S_{1,x} = \begin{pmatrix} 0 & \mathrm{i} & 0 \\ -\mathrm{i} & 0 & 0 \\ 0 & 0 & 0 \end{pmatrix}, \quad S_{1,y} = \begin{pmatrix} 0 & 0 & -\mathrm{i} \\ 0 & 0 & 0 \\ \mathrm{i} & 0 & 0 \end{pmatrix}, \quad S_{1,z} = \begin{pmatrix} 0 & 0 & 0 \\ 0 & 0 & \mathrm{i} \\ 0 & -\mathrm{i} & 0 \end{pmatrix}, \tag{2.16}$$

with commutation relations $[S_{1,i}, S_{1,j}] = -i\epsilon_{ijk}S_{1,k}$.

The threefold fermions described by $H_{3f}^{\phi_0}$ have full rotational invariance and effective spin $S = 1$, and we refer to them as symmetric threefold fermions (see Fig. 2.2).

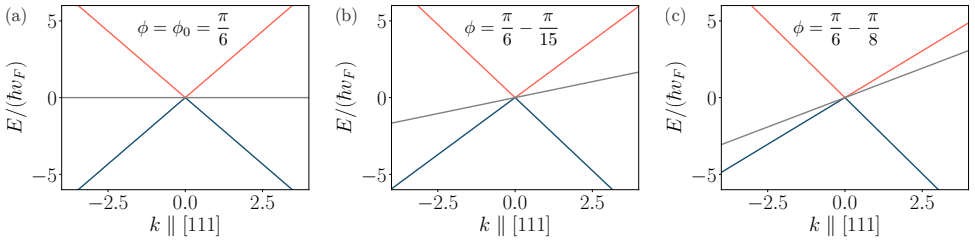

Figure 2.2: Band dispersion for symmetric and non-symmetric threefold fermions. (a) For $\phi = \phi_0 = \pi/2 \mod (\pi/3)$, the threefold Hamiltonian in Eq. 2.15 recovers the full rotational symmetry, and we refer to this case as symmetric threefold fermion. (b) For $\phi \neq \phi_0$ we are no longer in the symmetric case, and the Hamiltonian loses full-rotational symmetry. This leads to an asymmetry in the band structure, which becomes more asymmetric (c) as $|\phi - \phi_0|$ grows.

The eigenfunctions and eigenvalues for this Hamiltonian can be computed analytically[70,71],

$$\psi_s = \frac{1}{\sqrt{(3E_s^2 - k^2)(E_s^2 - k_z^2)}} \begin{pmatrix} E_s^2 - k_z^2 \\ E_s k_x e^{-i\phi} + k_y k_z e^{2i\phi} \\ E_s k_y e^{i\phi} + k_x k_z e^{-2i\phi} \end{pmatrix}, \tag{2.17}$$

where the energies E_s are given by[71]

$$E_s = \frac{2|\mathbf{k}|}{\sqrt{3}} \cos\left(\frac{1}{3}\arccos\left(3\sqrt{3}k_x k_y k_z \cos 3\phi\right) - \frac{2\pi(n-1)}{3}\right). \tag{2.18}$$

In the case $\phi = \phi_0$ the energies read $E_s = s\hbar v_F |\mathbf{k}|$, where $s = +1, 0, -1$ corresponds to the effective spin of the multifold fermion.

Following a similar procedure to the calculation of the topological charge of the Weyl fermion in Eqs. 2.6–2.11, we obtain the Berry curvature for each band[‡], which reads[70]

$$\Omega_\pm = i\nabla \times \langle \psi_\pm | \nabla \psi_\pm \rangle = \pm \frac{\mathbf{k}}{|\mathbf{k}|^3} \tag{2.19}$$

$$\Omega_0 = i\nabla \times \langle \psi_0 | \nabla \psi_0 \rangle = 0. \tag{2.20}$$

[‡]This calculation is done for $\phi = \pi/6$ as a representative value of $0 < \phi < \pi/3$. The results of the Chern number of the bands are valid for every $\phi \in (0, \pi/3)$. If we choose the sector $\pi/3 < \phi < 2\pi/3$, the result is the opposite, with $C_\pm = \mp 2$, and the threefold crossing acts as a sink of Berry flux.

We can integrate now the Berry curvature over a surface enclosing the threefold degeneracy in momentum space to obtain the Chern number

$$C_{\pm} = \frac{1}{2\pi} \int \Omega_{\pm} \cdot dS_{\mathbf{k}} = \pm 2. \tag{2.21}$$

This means that the threefold degeneracy is a monopole of Berry curvature with charge +2. Due to the nonzero topological charge, the surface Brillouin zone of the material hosting this threefold crossing will feature two Fermi arcs emanating from the projection of the degeneracy point $\mathbf{k}_0$ on the surface. Since we are considering systems with time-reversal symmetry, a time-reversal conjugate source of Berry curvature is placed at the time-reversed point in the Brillouin zone $-\mathbf{k}_0$. This time-reversal partner has the same monopole charge. The Nielsen-Ninomiya theorem requires the net topological charge in the Brillouin zone to be zero. Thus, two sinks of Berry curvature must exist to compensate the topological charge of the threefold crossings located at $\mathbf{k}_0$ and $-\mathbf{k}_0$. The projections of the sinks of Berry curvature on the surface are the termination of the Fermi arcs emanating from the threefold fermions, providing the first example of the existence of Fermi arcs without the presence of Weyl crossings[70].

2.2.3 Sixfold fermion

It is possible to have a sixfold crossing composed of two threefold fermions sitting at the same place protected by cubic symmetry, in the same way that we can find a fourfold degeneracy that consists of two Weyl fermions sitting at the same position with the same chirality. These sixfold crossings can happen at the R point in primitive cubic space groups 198, 212, and 213. The linear $k \cdot p$ Hamiltonian for these sixfold fermions can always be brought to a block-diagonal form, where the diagonal blocks are composed of threefold Hamiltonians (Eq. 2.15) and has the form

$$H_{6f} = \begin{pmatrix} H_{3f}\left(\mathbf{k}, \pi/2 - \phi\right) & 0 \\ 0 & H_{3f}\left(\mathbf{k}, \pi/2 + \phi\right) \end{pmatrix}. \tag{2.22}$$

The difference in the value of the ϕ parameters between both blocks translates into a generically different Fermi velocity for each of the two threefold fermions (see Fig. 2.1), similar to the case of the double-Weyl fermion.

2.2.4 Fourfold fermion

The last multifold fermion in the classification presented in Table 2.1 is the fourfold fermion. Unlike the double-Weyl fermion in Sec. 2.2.1, the linear $k \cdot p$ Hamiltonian of this fourfold degeneracy cannot be decomposed in terms of simpler multifold crossings. These fourfold degeneracies can be found only in materials with finite spin-orbit coupling, and can happen in points with tetrahedral or octahedral symmetry. The Berry curvature of the fourfold fermion corresponds to that of a spin-3/2 moment in a magnetic field. We start with the most general $k \cdot p$ Hamiltonian for the octahedral case,

$$H_{4f}(\mathbf{k}, a, b) = \begin{pmatrix} ak_z & 0 & -\frac{a+3b}{4}k_+ & \frac{\sqrt{3}(a-b)}{4}k_- \\ 0 & bk_z & \frac{\sqrt{3}(a-b)}{4}k_- & -\frac{3a+b}{4}k_+ \\ -\frac{a+3b}{4}k_- & \frac{\sqrt{3}(a-b)}{4}k_+ & -ak_z & 0 \\ \frac{\sqrt{3}(a-b)}{4}k_+ & -\frac{3a+b}{4}k_- & 0 & -bk_z \end{pmatrix}, \tag{2.23}$$

where $k_\pm = k_x \pm ik_y$, and a, b are two material-dependent parameters expressed in units of $\hbar v_F$, whose ratio we define as $\chi = \arctan(b/a)$.

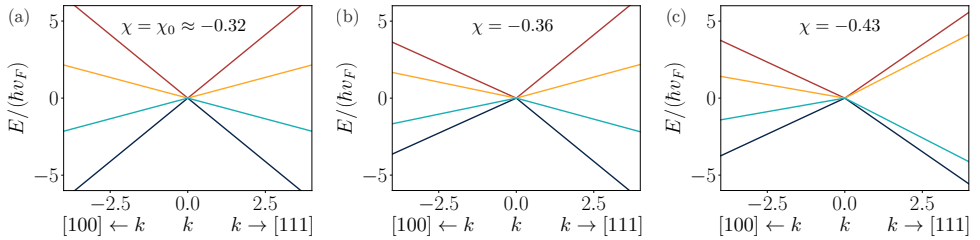

Figure 2.3: Band dispersion for symmetric and non-symmetric fourfold fermions. (a) For $\chi = \chi_0 = \arctan(-1/3)$, the fourfold Hamiltonian in Eq. 2.23 has full rotational symmetry. We refer to this case as symmetric fourfold fermion. (b) For $\chi \neq \chi_0$ the Hamiltonian loses full-rotational symmetry, leading to an asymmetry in the band structure, which becomes more asymmetric (c) as $|\chi - \chi_0|$ grows.

This Hamiltonian recovers the full rotational symmetry when $\chi = \chi_0 = \arctan(-3)$ ($b = -3a$) or $\chi = \chi_0 = \arctan(-1/3)$ ($b = -a/3$), for which the Hamiltonian takes the form $H_{4f}^{\chi_0}(\mathbf{k}) \equiv H_{4f}(\mathbf{k}, \chi_0) = \hbar v_F \mathbf{k} \cdot \mathbf{S}_{3/2}$, where $\mathbf{S}_{3/2}$ are three matrices that form a spin-3/2 representation of SU(2):

$$
\begin{aligned}
S_{3/2,x} &= \begin{pmatrix} 0 & 0 & 0 & \sqrt{3} \\ 0 & 0 & \sqrt{3} & -2 \\ 0 & \sqrt{3} & 0 & 0 \\ \sqrt{3} & -2 & 0 & 0 \end{pmatrix}, \\
S_{3/2,y} &= \begin{pmatrix} 0 & 0 & 0 & -\mathrm{i}\sqrt{3} \\ 0 & 0 & -\mathrm{i}\sqrt{3} & -2\mathrm{i} \\ 0 & \mathrm{i}\sqrt{3} & 0 & 0 \\ \mathrm{i}\sqrt{3} & 2\mathrm{i} & 0 & 0 \end{pmatrix}, \\
S_{3/2,y} &= \begin{pmatrix} 3 & 0 & 0 & 0 \\ 0 & -1 & 0 & 0 \\ 0 & 0 & -3 & 0 \\ 0 & 0 & 0 & 1 \end{pmatrix},
\end{aligned}
\tag{2.24}
$$

with commutation relations $\left[S_{3/2,i}, S_{3/2,j}\right] = 2\mathrm{i}\epsilon_{ijk} S_{3/2,k}$.

The fourfold fermions described by $H_{4f}^{\chi_0}(\mathbf{k})$ have full rotational invariance and effective spin $S = 3/2$, and we refer to them as symmetric fourfold fermions (see Fig. 2.3).

The energies of the fourfold Hamiltonian in Eq. 2.23 are given by[71]

$$E_1(\mathbf{k}) = \sqrt{\frac{\mathbf{k}^2 + \sqrt{\mathbf{k}^4 - 4f(\mathbf{k},\chi)}}{2}}, \qquad E_2(\mathbf{k}) = \sqrt{\frac{\mathbf{k}^2 - \sqrt{\mathbf{k}^4 - 4f(\mathbf{k},\chi)}}{2}},$$
$$E_3(\mathbf{k}) = -\sqrt{\frac{\mathbf{k}^2 - \sqrt{\mathbf{k}^4 - 4f(\mathbf{k},\chi)}}{2}}, \quad E_4(\mathbf{k}) = \sqrt{\frac{\mathbf{k}^2 + \sqrt{\mathbf{k}^4 - 4f(\mathbf{k},\chi)}}{2}}, \tag{2.25}$$

with

$$\begin{aligned} f(\mathbf{k},\chi) =& \frac{1}{8}(1-\cos 4\chi)(k_x^4 + k_y^4 + k_z^4) \\ &+ \frac{1}{8}(\frac{11}{4} + \frac{7}{4}\cos 4\chi + 3\sin 2\chi)(k_x^2 k_y^2 + k_x^2 k_z^2 + k_y^2 k_z^2). \end{aligned} \tag{2.26}$$

In the symmetric case $\chi = \chi_0$ the energies read $E_s = 2s\hbar v_F |\mathbf{k}|$, with $s = -3/2,\ -1/2,\ 1/2,\ 3/2$ corresponding to the effective spin of the multifold fermion.

We can identify distinct phases of the Hamiltonian depending on the value of χ in the range $[-\pi/2, \pi/2]$[70]. For values $-\pi/2 < \chi < -\pi/4$ the Chern number (Eq. 2.12) of the four bands is $C = 3, 1, -1, -3$ ordered in decreasing energy. For $-\pi/4 < \chi < 0$ the order is reversed, and the bands have Chern numbers $C = -3, -1, 1, 3$ in decreasing order of energy. For $\chi = -\pi/4$ the bands are degenerate in pairs, allowing for the Chern numbers to reverse their ordering in energy at this transition. Finally, for $0 < \chi < \pi/2$, $\chi \neq \pi/4$ the bands have Chern numbers $C = -3, 1, -1, 3$ ordered in decreasing energy. This phase of the Hamiltonian was first described in Ref. [70] and had no precedent in prior experimental or theoretical work. It is interesting to note that for $\chi = 0$ and $\chi = \pi/2$ the two middle bands are degenerate at zero energy, and for $\chi = \pi/4$ the degeneracies between the bands are not necessarily stable if we include higher-order terms in the $k \cdot p$ Hamiltonian[70].

Finally, in the tetrahedral case, an extra linear term is allowed, and the Hamiltonian for the most general fourfold fermion in this case is

$$H_{4f,T} = H_{4f} + \hbar v_T \begin{pmatrix} 0 & k_z & -\sqrt{3}k_x & ik_y \\ k_z & \frac{2k_z}{\sqrt{3}} & ik_y & \frac{k_x - 2ik_y}{\sqrt{3}} \\ -\sqrt{3}k_x & -ik_y & 0 & -k_z \\ -ik_y & \frac{k_x + 2ik_y}{\sqrt{3}} & -k_z & -\frac{2k_z}{\sqrt{3}} \end{pmatrix}, \quad (2.27)$$

where H_{4f} is the octahedral fourfold Hamiltonian given in Eq. 2.23, and the parameter v_T is proportional to the strength of the fourfold rotational symmetry breaking. Thus, this additional term can become relevant when v_T is large, and must be taken into account to obtain the correct result when computing physical observables.

The Chern number calculations for the different values of χ indicate that the fourfold (spin-3/2) crossing acts as a monopole of Berry curvature with topological charge three. Thus, this is the highest topological charge of a single multifold crossing that cannot be decomposed in simpler multifold crossings, and constitutes the second example of a fermion with no high-energy counterpart in the traditional classification of fermions.

With the fourfold fermion, we have introduced all chiral multifold fermions and the linear $k \cdot p$ models describing them. In the following chapters, these models will constitute the basis to compute multifold-specific properties and fingerprints in physical observables. However, we are also interested in more complex models that describe multifold fermions in realistic band structures. To this end, in the following section, we will build two material-specific tight-binding models that describe different multifold fermions in a single band structure, thus providing us with more realistic models to study materials candidates to host multifold fermions.

2.3 Material-oriented tight-binding models of chiral multifold fermions

All non-magnetic materials in nature crystallize in one of the 230 space groups. However, if we are interested in finding suitable materials, we need to consider materials that feature multifold crossings near the Fermi level, and we need these multifold crossings to be as isolated as possible in energy from other bands. A significant challenge is the synthesis of the candidate materials. As we will discuss in the experiment-oriented chapters of this thesis, the impurities and scattering lifetimes in the samples play a crucial role in masking the signatures of each multifold fermion in the physical observables. It is crucial, thus, to find materials that can be synthesized as clean single crystals to have a suitable sample for experimental detection.

2.3.1 Space group 199

The first tight-binding model that we consider describes a material in SG199 without spin-orbit coupling, which captures the adequate band connectivity and chirality. Materials in SG199 have body-centered cubic structures with Bravais lattice vectors

$$R_1 = \frac{a}{2}(-\hat{\mathbf{x}} + \hat{\mathbf{y}} + \hat{\mathbf{z}}), \qquad R_2 = \frac{a}{2}(\hat{\mathbf{x}} - \hat{\mathbf{y}} + \hat{\mathbf{z}}), \qquad R_3 = \frac{a}{2}(\hat{\mathbf{x}} + \hat{\mathbf{y}} - \hat{\mathbf{z}}).$$

To describe adequately the position of the atoms in the unit cell, we include the orbital embedding, *i.e.* the position of the orbitals within the unit cell, as described in Ref. [71] by conjugating the tight-binding Hamiltonian with a unitary matrix parametrized by x, with $|x| < 1/2$. This places the spinless $s-$orbitals in the positions $\mathbf{q}_i$, given by

$$\begin{aligned} \mathbf{q}_1 &= (x, x, x), & \mathbf{q}_2 &= (\frac{1}{2} - x, \frac{1}{2}, 0), \\ \mathbf{q}_3 &= (0, \frac{1}{2} - x, \frac{1}{2}), & \mathbf{q}_4 &= (\frac{1}{2}, 0, \frac{1}{2} - x), \end{aligned} \tag{2.28}$$

where $\mathbf{q}_i$ is expressed in reduced coordinates, *i.e.*, in units of R_i. A generic value in the range $-1/2 < x < 1/2$ sets the model to be in SG199. Choosing $x = 1/4$ increases the symmetry from tetrahedral to octahedral, provided the hoppings do not break this symmetry, describing a material in SG214. These requirements are satisfied by the tight-binding model and thus it can interpolate between SG199 and 214 depending on the value of u.

Then, we can write the tight-binding Hamiltonian for a material in SG199 as $H_{199}(x, \mathbf{k}) = U^\dagger(x, \mathbf{k}) H_0(\mathbf{k}) U(u, \mathbf{k})$, where

$$H_0(\mathbf{k}) = \begin{pmatrix} 0 & 1 & 1 & 1 \\ 1 & 0 & e^{-i\mathbf{k}\cdot\mathbf{R}_3} & e^{i\mathbf{k}\cdot\mathbf{R}_2} \\ 1 & e^{i\mathbf{k}\cdot\mathbf{R}_3} & 0 & e^{-i\mathbf{k}\cdot\mathbf{R}_1} \\ 1 & e^{-i\mathbf{k}\cdot\mathbf{R}_2} & e^{i\mathbf{k}\cdot\mathbf{R}_1} & 0 \end{pmatrix}, \tag{2.29}$$

and

$$U(x, \mathbf{k}) = \begin{pmatrix} e^{i\mathbf{k}\cdot\mathbf{q}_1} & 0 & 0 & 0 \\ 0 & e^{i\mathbf{k}\cdot\mathbf{q}_2} & 0 & 0 \\ 0 & 0 & e^{i\mathbf{k}\cdot\mathbf{q}_3} & 0 \\ 0 & 0 & 0 & e^{i\mathbf{k}\cdot\mathbf{q}_4} \end{pmatrix}. \tag{2.30}$$

In Fig. 2.4 we show the band structure of the tight-binding model for SG199 $H_{199}(x, \mathbf{k})$. This model features protected threefold nodes at the Γ point at energy $\mu_\Gamma/t = -1$ and at the $H = (-\pi, \pi, \pi)$ point at energy $\mu_H/t = 1$. It also hosts two Weyl nodes at the $P = (\pi/2, \pi/2, \pi/2)$ point, and two Weyl nodes with opposite chirality at $-P$, at energies $\mu_{W_1}/t = -1.732$ and $\mu_{W_2}/t = 1.732$.

Although the band structure of this model features threefold and Weyl crossings, at the moment of writing this thesis, no material has been found in this space group with only multifold fermions near the Fermi level. The lack of isolated multifold fermions in the band structure complicates the experimental detection, since the effect of the multifold degeneracies near the Fermi level can be masked by the contribution of trivial bands in the same range of energies. However, the tight-binding

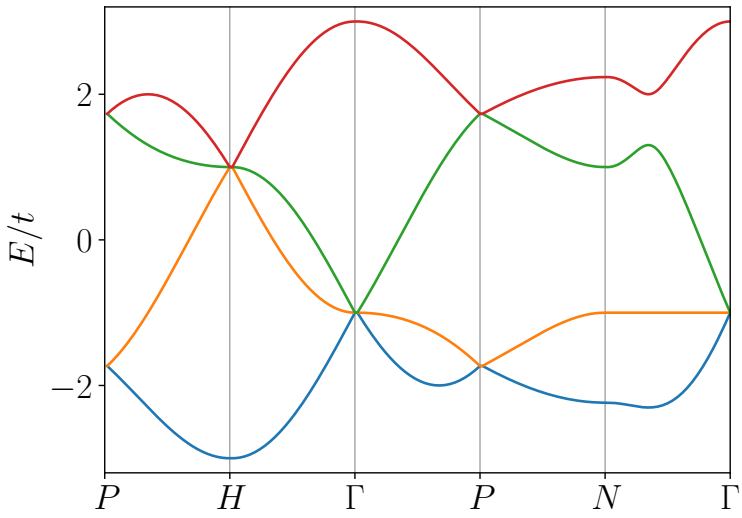

Figure 2.4: Band structure of the tight-binding model for SG199 in Eqs. 2.29–2.30. This model features a threefold crossing at the Γ point with energy $\mu_\Gamma/t = -1$ and at the $H = (-\pi, \pi, \pi)$ point at energy $\mu_H/t = 1$. Additionally, it hosts two Weyl nodes at the $P = (\pi/2, \pi/2, \pi/2)$ point with energies $\mu_{W_1}/t = -1.732$ and $\mu_{W_2}/t = 1.732$, and two Weyl crossings with opposite charge at $-P$.

model described in this section is a good platform to explore the effect of multifold fermions in physical observables.

2.3.2 Space group 198 and candidate materials

The next model describes a material in SG198. A variety of materials in this space group are candidates to host chiral multifold excitations[70,72,73,78]. The corresponding band crossings have been observed in angle-resolved photoemission experiments in RhSi[89], CoSi[90,91], or AlPt[92]. This model was originally introduced in Ref. [78], constructed with the most general terms allowed by the crystal symmetries of SG198. In the original tight-binding Hamiltonian $\mathcal{H}(\mathbf{k})$ the atoms are located in the positions

$$\mathbf{q}_A = (0,0,0)\,, \qquad \mathbf{q}_B = \left(\frac{1}{2},\frac{1}{2},0\right), \tag{2.31}$$

$$\mathbf{q}_C = \left(\frac{1}{2},0,\frac{1}{2}\right), \qquad \mathbf{q}_D = \left(0,\frac{1}{2},\frac{1}{2}\right), \tag{2.32}$$

given in reduced coordinates.

We include the orbital embedding following the same procedure described in the previous section for SG199, with $x = 0.3959$ for RhSi[71]. This leads to the new atomic positions

$$\begin{aligned} \mathbf{q}_A &= (x,x,x)\,, & \mathbf{q}_B &= \left(\frac{1}{2}+x,\frac{1}{2}-x,-x\right), \\ \mathbf{q}_C &= \left(\frac{1}{2}-x,-x,\frac{1}{2}+x\right), & \mathbf{q}_D &= \left(-x,\frac{1}{2}+x,\frac{1}{2}-x\right), \end{aligned} \tag{2.33}$$

The transformed tight-binding Hamiltonian takes the form $H_{198}(x,\mathbf{k}) = U_x(\mathbf{k})^\dagger \mathcal{H}(\mathbf{k}) U_x(\mathbf{k})$ with

$$U_x(\mathbf{k}) = \exp\left[\begin{pmatrix} ix(k_1+k_2+k_3) & 0 & 0 & 0 \\ 0 & ix(k_1-k_2-k_3) & 0 & 0 \\ 0 & 0 & ix(k_3-k_2-k_1) & 0 \\ 0 & 0 & 0 & ix(k_2-k_1-k_3) \end{pmatrix}\right], \tag{2.34}$$

and $\mathcal{H}(\mathbf{k})$ the tight-binding Hamiltonian without spin-orbit coupling presented in Ref. [78], which reads

$$\begin{aligned} \mathcal{H}(\mathbf{k}) =& v_1\Bigg[\tau^x\mu^0\cos\left(\frac{k_x}{2}\right)\cos\left(\frac{k_y}{2}\right) + \tau^x\mu^x\cos\left(\frac{k_y}{2}\right)\cos\left(\frac{k_z}{2}\right) \\ &\qquad + \tau^0\mu^x\cos\left(\frac{k_z}{2}\right)\cos\left(\frac{k_x}{2}\right)\Bigg] \\ &+ v_p\Bigg[\tau^y\mu^z\cos\left(\frac{k_x}{2}\right)\sin\left(\frac{k_y}{2}\right) + \tau^y\mu^x\cos\left(\frac{k_y}{2}\right)\sin\left(\frac{k_z}{2}\right) \\ &\qquad + \tau^0\mu^y\cos\left(\frac{k_z}{2}\right)\sin\left(\frac{k_x}{2}\right)\Bigg] \\ &+ v_2\Big[\cos(k_x)+\cos(k_y)+\cos(k_z)\Big]\tau^0\mu^0, \end{aligned} \tag{2.35}$$

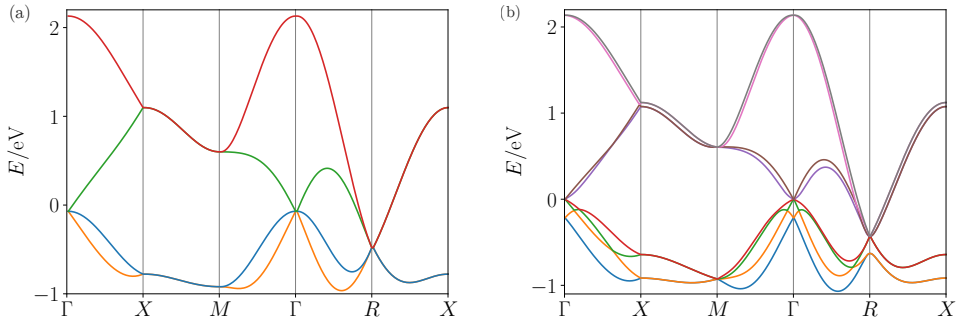

Figure 2.5: Band structure of the tight-binding model for SG198 with and without spin-orbit coupling. (a) When spin-orbit coupling is neglected, the band structure of the tight-binding model for SG198 (Eqs. 2.35–2.34) features a threefold fermion at the Γ point and a double-Weyl fermion at the R point. (b) When spin-orbit coupling is included, the threefold fermion at the Γ point splits into a fourfold fermion and a single Weyl fermion. The double-Weyl fermion at the R point splits into a sixfold fermion and a twofold Kramers pair. The tight-binding model with spin-orbit coupling can be found in Refs. [71,78].

where τ^i and μ^i, $i = x, y, z$, are the three Pauli matrices for spin-1/2, $\tau^0 = \mu^0 = \mathbb{I}_{2\times 2}$ is the 2×2 identity matrix, and $\tau^i\mu^j \equiv \tau^i \otimes \mu^j$ is a short-hand notation for the Kronecker product.

In Fig. 2.5 we show the band structure of the tight-binding model for SG198. When we include spin-orbit coupling, the threefold fermion at the Γ point decomposes in a fourfold (spin-3/2) and a single Weyl crossing separated proportionally to the spin-orbit coupling energy scale. We will devote part of the analysis in Chapter 4 to search signatures of the spin-3/2 fourfold fermion in a real material. Additionally, the double-Weyl crossing at the R point transforms into a sixfold degeneracy and a twofold Kramers pair. The details of the tight-binding model with spin-orbit coupling can be found in Refs. [71,78]. Thus, SG198 features all possible chiral multifold fermions when considering the spin-orbit coupled and spinless cases, making it an excellent platform to look for candidate materials.

Two of the materials crystallizing in SG198, RhSi and CoSi, feature threefold and double-Weyl degeneracies near the Fermi level and have been synthesized as single crystals. This makes them outstanding candidates to study the multifold fermions and their effect in the physical observables of multifold semimetals.

2.4 Conclusions

In this chapter, we introduced the concepts of Berry curvature and topological charge of band degeneracies in crystalline systems. We studied the complete classification of chiral multifold fermions in all possible crystal structures, providing a detailed catalog of where to find them in the Brillouin zone of each space group.

We built the most general low-energy $k \cdot p$ model for each type of multifold fermion. Using these models, we studied their topological features and the effective spin for the symmetric cases, which will play a fundamental role in the optical responses computed in the next chapter. We described two quasiparticles — the threefold and fourfold fermions — with no counterpart in the traditional classification of fermions. The $k \cdot p$ models constitute the starting point for characterizing the optical response of multifold fermions in the next chapter and will be crucial to understand the effect of the topological charge of multifold fermions in nonlinear responses in Chap. 5.

Finally, we constructed two tight-binding models based on the crystal symmetries of space groups 199 and 198. While no candidate materials are known at the moment for SG199, in SG198 we find RhSi and CoSi. In the following chapters we will focus on the study of RhSi and CoSi, the detection of chiral multifold fermions, and the impact of the topological charge of the multifold degeneracies in the optical responses of multifold semimetals.

3

Linear optical conductivity of chiral multifold fermions

$k \cdot p$ and tight-binding models

In this chapter we will derive the general expressions for the optical conductivity in the length gauge. The formalism presented here constitutes the building block for computing the linear and nonlinear responses throughout the following chapters. Using the expressions derived here, we will compute the linear optical conductivity of the low-energy $k \cdot p$ models for all chiral multifold fermions and identify fingerprints for each type of multifold fermion.

To obtain a more realistic optical conductivity of real materials, we will use the tight-binding models for SG198 and SG199 described in Sec. 2.3. We will compare our theoretical calculations with experimental data for materials crystallizing in SG198 in the next chapter.

3.1 Linear optical response in the length gauge

We will calculate the optical responses in the approximation where electrons do not interact with each other and behave as independent particles interacting with the electromagnetic field in the long-wavelength limit.

In order to provide a self-contained approach we will derive the expression for the optical conductivity in the length-gauge that we will use throughout the following chapters. In this formalism, and considering the approximations in the previous paragraph, we can neglect the position dependence of the electric field and write the coupling of the bare Hamiltonian H_0 for the electrons in a crystal to the electric field as

$$\hat{H} = \hat{H}_0 + \hat{V}(t), \qquad \hat{V}(t) = -e\mathbf{E}(t) \cdot \hat{r}. \tag{3.1}$$

Here $\hat{r}$ is the position operator, $\mathbf{E}(t)$ is the time-dependent external electric field, and $e < 0$ is the elementary charge. We will consider a monochromatic source in what follows, meaning that we only have one frequency.

The non-interacting term of the Hamiltonian H_0 has eigenstates $|n\mathbf{k}\rangle$ associated with eigenvalues $\hbar\omega_n(\mathbf{k})$, labeled by the band index n and the crystalline momentum $\mathbf{k}$.

In the interacting term of the Hamiltonian, the time-dependent electric field can be parametrized as*

$$\mathbf{E}(t) = \frac{1}{2} E^a_\omega e^{-i\omega t} \hat{e}_a + \text{c.c.}, \tag{3.2}$$

where E^a_ω is the amplitude of the field for the frequency ω in the direction a, $\hat{e}_a$ is the corresponding unitary vector, and c.c. indicates the complex conjugate. The remaining element to define in Eq. 3.1 is the position operator $\hat{r}$. We can express the matrix elements of the position operator between two Bloch states as[93]

$$\langle m\mathbf{k}| \hat{r} |n\mathbf{k}'\rangle = i\delta_{mn}\nabla_{\mathbf{k}}\delta_{\mathbf{k},\mathbf{k}'} + \delta_{\mathbf{k},\mathbf{k}'}\mathcal{A}_{mn}(\mathbf{k}), \tag{3.3}$$

where $\mathcal{A}_{mn}(\mathbf{k})$ is the non-Abelian Berry connection for two bands m, n

$$\mathcal{A}_{mn}(\mathbf{k}) = i \langle u_m(\mathbf{k})| \nabla_{\mathbf{k}} |u_n(\mathbf{k})\rangle . \tag{3.4}$$

The form of $\hat{r}_{mn}$ leads to a separation of the intraband ($\hat{r}^{(i)}$) and interband ($\hat{r}^{(e)}$) matrix elements of the position operator. We define these two terms as

$$\hat{r}^{(e)} \equiv \sum_{\mathbf{k}\mathbf{k}'} \sum_{m\neq n} \hat{r}^{(e)}_{mn} |m\mathbf{k}\rangle \langle n\mathbf{k}'| , \tag{3.5}$$

$$\hat{r}^{(i)} \equiv \sum_{\mathbf{k}\mathbf{k}'} \sum_{m} \hat{r}^{(i)}_{mn} |m\mathbf{k}\rangle \langle m\mathbf{k}'| . \tag{3.6}$$

*Alternatively, in some parametrizations the factor 1/2 is absent, which must be taken into account when comparing our expressions with other works or with experimental results.

Since the matrix elements read

$$\langle m\mathbf{k}|\,\hat{r}\,|n\mathbf{k}'\rangle = \begin{cases} i\nabla_{\mathbf{k}}\delta_{\mathbf{k},\mathbf{k}'} + \delta_{\mathbf{k},\mathbf{k}'}\mathcal{A}_{mn}(\mathbf{k}) & , m = n \\ \delta_{\mathbf{k},\mathbf{k}'}\mathcal{A}_{mn}(\mathbf{k}) & , m \neq n \end{cases}, \tag{3.7}$$

the inter- and intra-band matrix elements are

$$\langle m\mathbf{k}|\,\hat{r}^{(e)}\,|n\mathbf{k}'\rangle = (1-\delta_{mn})\,\delta_{\mathbf{k},\mathbf{k}'}\mathcal{A}_{mn}\,(\mathbf{k})\,, \tag{3.8}$$

$$\langle m\mathbf{k}|\,\hat{r}^{(i)}\,|n\mathbf{k}'\rangle = \delta_{mn}\left(\delta_{\mathbf{k},\mathbf{k}'}\mathcal{A}_{mn}\,(\mathbf{k}) + i\nabla_{\mathbf{k}}\delta_{\mathbf{k},\mathbf{k}'}\right). \tag{3.9}$$

In the remainder of this section we will build a perturbative approach that allows us to compute the conductivity as a series of terms proportional to increasing powers of the electric field. The first object we need to define is the density matrix for the system

$$\hat{\rho}(t) \equiv \sum_{mn} \rho_{mn}(t)\,|m\rangle\,\langle n|\,, \tag{3.10}$$

where $|m\rangle$ are the eigenstates of $\hat{H}_0$ and we have omitted the $\mathbf{k}$-dependence in the notation. In the Schrodinger representation, the density matrix ρ obeys the quantum Liouville equation

$$i\hbar\frac{\mathrm{d}\rho}{\mathrm{d}t} = \left[\hat{H},\rho\right], \tag{3.11}$$

where $\hat{H}$ is the total Hamiltonian of the system.

To simplify the derivation, we will change from the Schrodinger picture, where operators do not carry time dependence and the evolution of the system is contained in the states, to the interaction picture, where the operators evolve in time. We will denote the operators in the interaction picture by $\tilde{\theta} = \hat{U}\hat{\theta}\hat{U}^{\dagger}$, where $\hat{U} = e^{i\hat{H}_0 t}$ is the time evolution operator. The wave functions in the interaction

picture have the form $|\tilde{\psi}\rangle = \hat{U}_0^\dagger |\psi\rangle$, and the density matrix is expressed as $\tilde{\rho} = \hat{U}_0^\dagger \rho U_0$.

Introducing the expressions for $\tilde{\rho}$ and $\hat{H}$ in Eq. 3.11 we obtain the Liouville equation for the density matrix in the interaction picture

$$i\hbar \frac{\partial \tilde{\rho}(t)}{\partial t} = -\left[e\hat{\tilde{r}} \cdot \mathbf{E}(t), \tilde{\rho}(t) \right]. \tag{3.12}$$

Integrating this equation and using Eqs. 3.8–3.9 we obtain

$$\begin{aligned} i\hbar\tilde{\rho}_{mn}(t) &= i\hbar\rho^{(0)}_{mn} - \int_{-\infty}^{t} \mathrm{d}t' \, \langle m| \left[e\hat{\tilde{r}}(t) \cdot \mathbf{E}(t), \tilde{\rho}(t') \right] |n\rangle & (3.13) \\ &= i\hbar\rho^{(0)}_{mn} - e\int_{-\infty}^{t} \mathrm{d}t' e^{i\omega_{mn}t'/\hbar} \Bigg(\sum_l \left[(1-\delta_{ml})\, \mathcal{A}^a_{ml}\rho_{ln} \right. \\ &\qquad \left. - (1-\delta_{ln})\, \rho_{ml}\mathcal{A}^a_{ln} \right] + (\rho_{mn})_{;k_a} \Bigg) E_a(t'), & (3.14) \end{aligned}$$

where $\omega_{mn} = (\epsilon_m - \epsilon_n)/\hbar$, and

$$(\rho_{mn})_{;k_a} = \rho_{mn}\left(\mathcal{A}^a_{mm} - \mathcal{A}^a_{nn}\right) + i\nabla_{k_a}\rho_{mn}. \tag{3.15}$$

We can proceed now to solve Eq. 3.13 recursively. In the absence of the external field $\mathbf{E}(t)$, the unperturbed density matrix describes a system in equilibrium, and the density matrix reads $\rho^{(0)}_{mn} = \delta_{mn} f_m$, where f_m is the Fermi-Dirac distribution for band m. Using this expression for the zeroth order, we can build the first order solution for the density matrix:

$$\begin{aligned} i\hbar\tilde{\rho}_{mn}(t) &= i\hbar\delta_{mn}f_m \\ &\quad - \frac{e}{2}\int_{-\infty}^{t} \mathrm{d}t' e^{i\omega_{mn}t'} e^{-i\omega t'} \left[i\delta_{mn}\partial_{k_a} f_m E^a_\omega + (1-\delta_{mn})\mathcal{A}^a_{mn} f_{nm} E^a_\omega \right]. \end{aligned} \tag{3.16}$$

where $f_{nm} = f_n - f_m$, and we have introduced the explicit form of the electric field (Eq. 3.2).

We consider an adiabatic turn-on of the external perturbation, this is, we assume that the interaction is turned on at $t = -\infty$. This translates into a shift $\omega \to \omega + i\eta$, where η is a positive infinitesimal, allowing us to perform the time integration in the previous equation as follows:

$$\begin{aligned}
&\int_{-\infty}^{t} \mathrm{d}t' e^{i(\omega_{mn}-\omega)t'} = \left.\frac{e^{i(\omega_{mn}-\omega)t'}}{i\left(\omega_{mn}-\omega\right)}\right|_{-\infty}^{t} \\
&= \lim_{\eta\to 0^+} \frac{1}{i\left(\omega_{mn}-\omega-i\eta\right)} \left[e^{i\omega_{mn}t}e^{-i\omega t}e^{\eta t} - \lim_{t'\to\infty} e^{i(\omega_{mn}-\omega)t'}e^{\eta t'}\right] \\
&= \lim_{\eta\to 0^+} \frac{1}{i\left(\omega_{mn}-\omega-i\eta\right)} e^{i\omega_{mn}t}e^{-i(\omega+i\eta)t}.
\end{aligned} \tag{3.17}$$

Now, omitting the explicit limit $\eta \to 0^+$, the dynamic equation for the density matrix reads

$$\begin{aligned}
&i\hbar\tilde{\rho}_{mn}(t) = i\hbar\delta_{mn}f_m \\
&-\frac{e}{2}\left[i\delta_{mn}\left(\partial_{k_a}f_m\right)E^a_\omega + \left(1-\delta_{mn}\right)\mathcal{A}^a_{mn}f_{nm}E^a_\omega\right]\frac{e^{i\omega_{mn}t}e^{-i(\omega+i\eta)t}}{i\left(\omega_{mn}-\omega-i\eta\right)}.
\end{aligned} \tag{3.18}$$

This expression constitutes the first iterative solution of the Liouville equation for the density matrix in the interaction picture (Eq. 3.12), where can identify the terms proportional to E^a_ω:

$$\tilde{\rho}^{(1)}_{mn}(t) = -\frac{e}{2\hbar}\left[\left(1-\delta_{mn}\right)\mathcal{A}^a_{mn}f_{nm} + i\delta_{mn}\left(\delta_{k_a}f_m\right)\right]\frac{E^a_\omega e^{i\omega_{mn}t}e^{-i(\omega+i\eta)t}}{i\left(\omega_{mn}-\omega-i\eta\right)}. \tag{3.19}$$

For later convenience, we will rewrite the linear term of the density matrix in the Schrodinger representation using the relation $\tilde{\rho} = \hat{U}_0^\dagger \rho U_0$ as

$$\rho^{(1)}_{mn}(t) = -\frac{e}{2\hbar}\left[(1-\delta_{mn})\,\mathcal{A}^a_{mn} f_{nm} + i\delta_{mn}\left(\delta_{k_a} f_m\right)\right]\frac{E^a_\omega e^{-i(\omega+i\eta)t}}{\omega-\omega_{mn}+i\eta}. \tag{3.20}$$

Since we are interested in computing the conductivity, we recall that when an electromagnetic wave with electric field given by Eq. 3.2 acts on an electronic system, the induced current density can be expressed as a sum of contributions proportional to increasing powers of the field magnitude

$$J_a(t) = \sum_{N=1}^{\infty}\sum_{\omega_1=\pm\omega}\cdots\sum_{\omega_N=\pm\omega}\sigma^{(N)}_{ab\ldots c}(\omega_1,\ldots,\omega_N)\,\frac{E^b_{\omega_1}\ldots E^c_{\omega_N}}{e^{i(\omega_1+\cdots+\omega_N)t}}, \tag{3.21}$$

where $\sigma^{(N)}_{ab\ldots c}(\omega_1,\ldots,\omega_N)$ is the $N-$th order frequency-dependent conductivity described by a rank $N+1$ tensor that determines the cartesian component a of the current $J_a(t)$ as a function of the electric field. It is important to note that we have summed over each $\omega_m = \pm\omega$ to account for the negative frequency component in the definition of the electric field (Eq. 3.2).

We can compute the current density in terms of the density matrix as

$$\begin{aligned} J(t) \equiv \mathrm{Tr}\left[\hat{\rho}(t)\hat{j}\right] &= -\frac{ge}{\Omega}\sum_{mn} v_{nm}\rho_{mn}(t) \\ &= -\frac{ge}{\Omega}\sum_{N=0}^{\infty}\sum_{\omega_1=\pm\omega}\cdots\sum_{\omega_N=\pm\omega}\sum_{mn} v_{nm}\rho^{(N)}_{mn}(t), \end{aligned} \tag{3.22}$$

where $g=2$ accounts for the spin degeneracy, Ω is the $D-$dimensional volume of the system, $\rho^{(N)}_{mn}(t)$ is the N-th order solution of Eq. 3.12 in the Schrodinger picture, and v_{mn} are the matrix elements of the single-particle velocity operator, defined as

$$\hat{v} \equiv \frac{i}{\hbar}\left[\hat{H},\hat{r}\right]. \tag{3.23}$$

We can now identify the $N-$th order conductivity with the N-th order term of the density matrix:

$$\sigma^{(N)}_{ab\ldots c}(\omega_1,\ldots,\omega_N)\frac{E^b_{\omega_1}\ldots E^c_{\omega_N}}{e^{i(\omega_1+\cdots+\omega_N)t}} = -\frac{ge}{\Omega}\sum_{mn} v^a_{nm}\rho^{(N)}_{mn}(t). \tag{3.24}$$

We introduce the first-order density matrix (Eq. 3.20) in the right-hand side of Eq. 3.24 to obain

$$\begin{aligned}
&-\frac{ge}{\Omega}\sum_{mn} v^a_{nm}\rho^{(1)}_{mn}(t) \\
&= \frac{ge^2}{2\Omega\hbar}\sum_{mn} v^a_{mn}\left[(1-\delta_{nm})\,\mathcal{A}^b_{mn}f_{nm} + i\delta_{mn}\left(\partial_{k_b}f_m\right)\right]\frac{1}{\omega-\omega_{mn}+i\eta}\frac{E^b_\omega}{e^{i(\omega+i\eta)t}}.
\end{aligned} \tag{3.25}$$

Comparing this with the left-hand side of Eq. 3.24 we arrive to the final expression for the linear optical condutivity

$$\sigma^{(1)}_{ab}(\omega) = \frac{ige^2}{2\Omega\hbar}\sum_{mn}\left[(1-\delta_{mn})\frac{v^b_{mn}}{\omega_{mn}}f_{nm} + \delta_{mn}\left(\partial_{k_b}f_m\right)\right]\frac{v^a_{nm}}{\omega-\omega_{mn}+i\eta}, \tag{3.26}$$

where we have used the relation $\mathcal{A}^a_{mn} = iv^a_{mn}/\omega_{mn}$, obtained from combining Eq. 3.8 and Eq. 3.23.

It is now easy to separate the interband and intraband contributions by considering explicitly the δ_{mn} functions involved:

$$\sigma^{\text{inter}}_{ab}(\omega) = \frac{ige^2}{2\Omega\hbar}\sum_{m\neq n}\omega_{nm}\frac{r^a_{nm}r^b_{mn}}{\omega-\omega_{mn}+i\eta}f_{nm}, \tag{3.27}$$

$$\sigma^{\text{intra}}_{ab}(\omega) = \frac{ige^2}{2\Omega\hbar}\sum_{m}\frac{v^a_{mm}}{\omega+i\eta}\partial_{k_b}f_m. \tag{3.28}$$

where we have used the relation $v_{nm} = ir_{nm}\omega_{nm}$ for $m \neq n$. These expressions constitute the building blocks for the computation of linear and nonlinear optical responses in this work.

The interband optical conductivity in Eq. 3.27 corresponds to transitions of electrons from an occupied state to an empty state with the same momentum separated by the energy of the incoming photon $\hbar\omega$. The interband contribution depends on the matrix elements r_{nm} connecting the occupied and empty bands involved in the electronic transition. Since $\sum_{m\neq n}$ implicitly involves an integration over **k**-space, the joint density of states (JDOS) gives information about which photons of a particular energy are more effective in producing an interband transition. For example, if the energy separation between the occupied and empty bands is nearly constant over many **k** values there are many initial and final states which can be coupled by the same photon energy, resulting in a large contribution to the JDOS.

The intraband optical conductivity in Eq. 3.28 accounts for electronic transitions within the same band from an occupied to an empty state. The real part of the intraband response can be modeled by the Drude formula[94,95]

$$\mathrm{Re}\left[\sigma_{ab}^{intra}(\omega)\right] = \frac{2\pi}{Z_0}\frac{\Omega_p^2}{\tau\left(\omega^2+\tau^{-2}\right)}, \tag{3.29}$$

a Lorentzian distribution centered at $\omega = 0$ with width $1/\tau$, where Ω_p is the plasma frequency, τ is the scattering rate in the material, and Z_0 is the electric impedance of vacuum.

In the next section we will focus in the interband optical conductivity (Eq. 3.27) to identify signatures of multifold fermions in the optical conductivity. In the next chapter we will study the optical response of real materials. To identify the fingerprints of multifold fermions in a real experiment it will be necessary to model the intraband response and extract the interband optical conductivity from the experimental data.

The goal of this section is to calculate the interband contribution to the optical conductivity of all chiral multifold fermions. Since multifold crossings occur in cubic space groups, the three diagonal elements σ_{xx}, σ_{yy}, and σ_{zz} are equal and we can focus on a single component, σ_{xx} [†].

In the main body of this chapter we compute the real part of the interband optical conductivity, and obtain its imaginary part using standard Kramers-Kronig relations[94] in Appendix C. There is an additional Fermi surface contribution to the conductivity, the intraband Drude-like term in Eq. 3.29, that scales as $1/\omega$ when $\omega \to 0$ and will be dominant at small frequencies. Since this contribution is not different from any other metal[95] we omit it in the discussion that follows, and we will come back to it in the next chapter.

3.2.1 Optical conductivity of fully rotationally symmetric models

The lowest-degeneracy multifold fermion is the twofold described by the Weyl Hamiltonian (Eq. 2.1). A simple dimensional analysis of Eq. 3.27 using the Weyl Hamiltonian shows that the optical conductivity of Weyl fermions must have a linear dependence on the frequency ω[24,55,97] (see Sec. 1.1.3), and its explicit computation gives as a result[57]

$$\sigma_W(\omega) = \frac{\omega e^2}{24\pi\hbar v_F} \frac{\sinh(\hbar\omega\beta/2)}{\cosh(\mu\beta) + \cosh(\hbar\omega\beta/2)}. \tag{3.30}$$

In the limit of zero temperature Eq. 3.30 takes the known form[24,55,57,97] $\sigma_W(\omega) = \frac{\omega e^2}{24\pi v_F \hbar}\Theta(\hbar\omega - 2\mu)$, where $\Theta(x)$ is the Heaviside step function. The optical conductivity grows linearly as the frequency increases above the frequency threshold $\omega = 2\mu$. The value of this threshold is determined by the activation frequency of optical transitions from the lower band to the upper band, set by the distance between the Weyl node and the Fermi level μ.

[†]There is a type of double spin-1/2 fermion that can occur in non-cubic space groups[96]. Since our results will not change qualitatively and RhSi and CoSi — the materials studied in this thesis — are cubic, we restrict our analysis to cubic space groups.

	Symmetric Hamiltonian	$\sigma\left(\frac{e^2}{\hbar v_F}\right)$
Weyl (spin-1/2)	$\mathrm{k}\cdot\sigma$	$\sigma_{2f}=\frac{\omega}{24\pi}$ for $\hbar\omega>2\mu$
Threefold (spin-1)	$\mathrm{k}\cdot\mathrm{S}_1$	$\sigma_{3f}=\frac{\omega}{6\pi}$ for $\hbar\omega>\mu$
Fourfold (spin-3/2)	$\mathrm{k}\cdot\mathrm{S}_{3/2}$	$\sigma_{4f}=\begin{cases}\frac{\omega}{8\pi} \text{ for } \frac{2}{3}\mu<\hbar\omega<2\mu\\ \frac{\omega}{6\pi} \text{ for } \hbar\omega>2\mu\end{cases}$
Double-Weyl ($2\times$ spin-1/2)	$\begin{pmatrix}\mathrm{k}\cdot\sigma & 0\\ 0 & \mathrm{k}\cdot\sigma\end{pmatrix}$	$\sigma_{4f}^{2\times\frac{1}{2}}=2\times\sigma_{2f}$
Sixfold ($2\times$ spin-1)	$\begin{pmatrix}\mathrm{k}\cdot\mathrm{S}_1 & 0\\ 0 & \mathrm{k}\cdot\mathrm{S}_1\end{pmatrix}$	$\sigma_{6f}=2\times\sigma_{3f}$

Table 3.1: Effective Hamiltonians (in units of $1/\hbar v_F$) and their corresponding optical conductivities for all symmetric chiral multifold fermions. The optical conductivity of the effective models for the Weyl, threefold, and fourfold fermions are defined piecewise for each region delimited by their characteristic frequencies. The effective Hamiltonian of the double-Weyl fermion is a direct sum of two Weyl Hamiltonians, and its optical conductivity is twice that of the Weyl fermion. Similarly, the effective Hamiltonian of the sixfold fermion is the direct sum of two threefold Hamiltonians, and its optical conductivity is two times that of the threefold fermion.

The double-Weyl fermion consists of two decoupled copies of the Weyl Hamiltonian (see Sec. 2.2.1) and thus its optical conductivity is twice the optical conductivity of the Weyl fermion given by Eq. 3.30. We express it as $\sigma_{4f}^{2\times1/2}(\omega)=2\sigma_W(\omega)$ (see Table 3.1 and Fig. 3.1 (c)). If the Weyl bands are tilted, the characteristic frequency $\hbar\omega_W=2\mu$ at which the optical conductivity changes from being zero to being linear in ω depends on the magnitude of the tilt, but its linear dependence remains unaltered[98].

The next multifold fermion we consider is the spin-1 threefold fermion. The most general low-energy Hamiltonian $H_{3f}(\mathbf{k},\phi)$ for a threefold fermion was obtained in Eq. 2.15. In the symmetric case, $\phi=\phi_0\equiv\pi/2$ mod $(\pi/3)$) and the Hamiltonian takes the form $H_{3f}^{\phi_0}(\mathbf{k})\equiv H_{3f}(\mathbf{k},\phi_0)=\hbar v_F\mathbf{k}\cdot\mathbf{S}_1$, where $\mathbf{S}_1=(S_{1,x},S_{1,y},S_{1,z})$ is a vector of three spin-1 matrices which form a representation of SU(2).

The band energies for the spin-1 symmetric threefold fermion are $E_s=s\hbar v_F\left|\mathbf{k}\right|$ (see Fig. 3.1 (a)), where $s=-1,0,1$ correspond to the three possible values of the effective spin of the fermion. In this case, the velocity matrix elements between states $s,s^{'}$ satisfy $v_{s,s'}=\langle s|\,\hat{v}\,|s^{'}\rangle=0$ if $s-s^{'}\neq\pm1$. This results in an optical selection rule: a photon can excite an electron from a filled band s to an unoccupied band s' only if the selection rule $\Delta s=s'-s=\pm1$ is satisfied, as depicted in Fig. 3.1 (a).

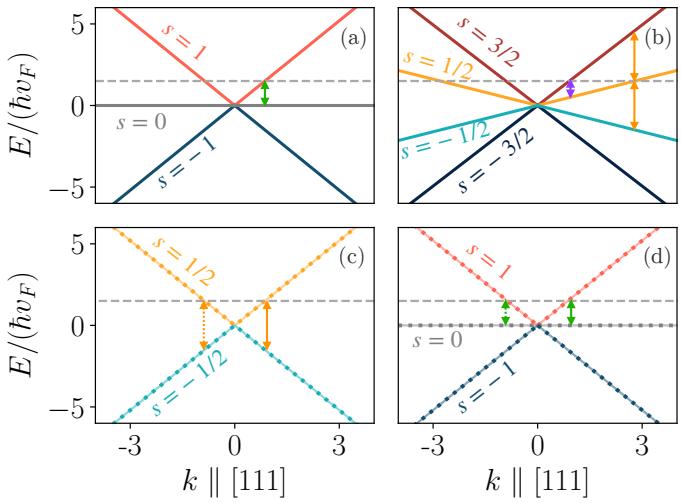

Figure 3.1: Band structures of the rotationally symmetric multifold fermions in the high-symmetry direction $\mathbf{k}^{111} = k(1,1,1)/\sqrt{3}$. (a) Threefold fermion (spin-1), (b) spin-3/2 fourfold fermion, (c) double spin-1/2 fourfold fermion and (d) sixfold fermion (double spin-1). The labels indicate the effective spin quantum number s of each band. The vertical arrows indicate the only allowed interband transitions, those that satisfy $\Delta s = s - s' = \pm 1$, with characteristic frequencies $\hbar\omega = 2\mu/3$ (purple), $\hbar\omega = \mu$ (green) and $\hbar\omega = 2\mu$ (orange).

By inserting the analytic energies and the eigenfunctions of $H_{3f}^{\phi_0}$ (Eqs. 2.17–2.18), in Eq. 3.27 we obtain the optical conductivity

$$\sigma_{3f}^{\phi_0}(\omega,\mu,\beta) = \frac{\omega e^2}{6\pi\hbar v_F}\frac{\sinh(\hbar\omega\beta)}{\cosh(\hbar\omega\beta)+\cosh(\mu\beta)}, \tag{3.31}$$

where ϕ_0 refers to the symmetric case, $\phi = \phi_0 = \pi/2 \mod (\pi/3)$. Taking the $T \to 0$ ($\beta \to \infty$) limit, the optical conductivity simplifies to

$$\sigma_{3f}^{\phi_0}(\omega,\mu,\beta) = \frac{\omega e^2}{6\pi\hbar v_F}\Theta(\hbar\omega-\mu). \tag{3.32}$$

From Eq. 3.32 we see that the optical conductivity of the threefold fermion is linear with ω as for the Weyl fermion, yet four times larger given the same Fermi velocity v_F (see Table 3.1). Also, the characteristic frequency at which the optical conductivity starts to grow linearly with the frequency is $\hbar\omega_{3f} = \mu$, which is different from the characteristic frequency of the Weyl fermion $\hbar\omega_W = 2\mu$. At $\omega = \omega_{3f}$ the only allowed interband transition is activated (green arrow in Fig. 3.1 (a)), connecting a filled and an empty band with $\Delta s = s' - s = \pm 1$.

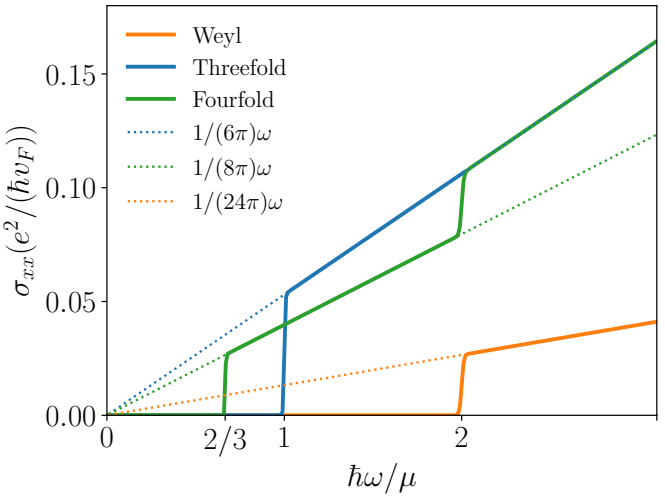

Figure 3.2: Comparison between the optical conductivities of the symmetric multifold fermions for which all cases in Table 3.1 are built. A single threefold or fourfold fermion has a larger conductivity than a Weyl fermion, normalized per node and by their Fermi velocity. The possible activation frequencies are $\hbar\omega = 2\mu/3, \mu$ or 2μ, and characterize each type of multifold fermion.

Since the low-energy Hamiltonian describing the sixfold fermion can be brought to a block-diagonal form with two copies of the threefold Hamiltonian in the diagonal (see Sec. 2.2.3), its optical conductivity is twice that of the threefold fermion (see Table 3.1 and Fig. 3.1 (d)).

We now carry out a similar analysis to obtain the optical conductivity for the symmetric fourfold fermion. As discussed in Sec. 2.2.4, a fourfold fermion recovers the full rotational symmetry when $\chi_0 = \arctan(-3)$ or $\arctan(-1/3)$, for which the Hamiltonian (Eq. 2.23) takes the form $H_{4f}^{\chi_0}(\mathbf{k}) \equiv H_{4f}(\mathbf{k}, \chi_0) = \hbar v_F \mathbf{k} \cdot \mathbf{S}_{3/2}$, where $\mathbf{S}_{3/2}$ are three matrices that form a spin-3/2 representation of SU(2). In this case, the energies are given by $E_s = s\hbar v_F |\mathbf{k}|$, with $s = -\frac{3}{2}, -\frac{1}{2}, \frac{1}{2}, \frac{3}{2}$ corresponding to the effective spin of the multifold fermion (see Fig. 3.1 (b)). Similar to the threefold case, the selection rules only allow transitions between a band s and a band s' such that $\Delta s = s' - s = \pm 1$.

Inserting the energies (Eqs. 2.25–2.26) and the eigenfunctions of the symmetric fourfold fermion[‡] in the expression for the optical

[‡]Although the eigenfunctions can be obtained analytically, their form is too cumbersome to show them here.

conductivity (Eq. 3.27) we obtain

$$\sigma_{4f}^{\chi_0}(\omega,\mu,\beta) = \frac{\omega e^2}{8\pi\hbar v_F}\left[\frac{\sinh(\hbar\omega\beta/2)}{\cosh(\hbar\omega\beta/2)+\cosh((\mu-\hbar\omega)\beta)} + \frac{4}{3}\frac{\sinh(\hbar\omega\beta/2)}{\cosh(\hbar\omega\beta/2)+\cosh(\mu\beta)}\right]. \tag{3.33}$$

Taking the zero temperature limit $T \to 0$ Eq. 3.33 simplifies considerably to

$$\sigma_{4f}^{\chi_0}(\omega,\mu) = \frac{\hbar\omega e^2}{8\pi\hbar v_F}\left[\frac{1}{3}\Theta(\hbar\omega-2\mu)+\Theta(\hbar\omega-\frac{2}{3}\mu)\right]. \tag{3.34}$$

The conductivity depends linearly on the frequency ω of the photon. In this case we find two characteristic frequencies due to the multiple possible optical transitions between the fourfold bands, $\hbar\omega_{4f,1} = 2\mu/3$ and $\hbar\omega_{4f,2} = 2\mu$ (see Fig. 3.1 (b)), defining two separate regions in the optical conductivity with different linear dependence on ω. As in the threefold case, the velocity matrix elements between states $s, s^{'}$ satisfy $v_{s,s'} = \langle s|\,\hat{v}\,|s^{'}\rangle = 0$ if $s - s^{'} \neq \pm 1$. When $\omega_{4f,1} < \omega$ the transition with $\Delta s = \pm 1$ from the intermediate-upper band to the upper band is allowed, until it vanishes at $\omega = \omega_{4f,2}$. When $\omega > \omega_{4f,2}$ the transition between the two intermediate bands is activated (lower orange arrow in Fig. 3.1 (b)).

Finally, for tetrahedral groups an extra linear term is allowed and the Hamiltonian is expressed in Eq. 2.27, and its optical conductivity is discussed in Appendix A.

In Fig. 3.2 we compare the optical conductivities of the Weyl fermion and the symmetric threefold and fourfold fermions discussed in this section at zero temperature. For $2\mu/3 < \hbar\omega < 2\mu$ the optical conductivity of the spin-3/2 fourfold is larger than that of the Weyl for a given v_F, but smaller than that of the threefold, while in the region $\hbar\omega > 2\mu$ the optical conductivity of the threefold and the fourfold are equal. Thus, per node, the linear optical conductivity of threefold and fourfold fermions is larger than that of a Weyl fermion.

The characteristic frequencies that activate the interband transitions are different for each symmetric multifold fermion, and they do not depend on dimensionality[99]. Thus, their characteristic frequencies constitute a unique fingerprint for each type of multifold fermion, and can be used to distinguish each type of multifold fermion regardless of the dimension of the system.

Temperature controls the abruptness of the jump in the optical conductivity at the characteristic frequencies. Thermally activated carriers will populate states above the Fermi level and empty states below it, broadening the step function in Eq. 3.32 (see Appendix B, Fig. B.1).

3.2.2 Optical conductivity of non-symmetric low-energy models

In real materials, the material-dependent parameter ϕ is pinned to the symmetric value ϕ_0 only if spin-orbit coupling is absent[77]. Spin-orbit coupling splits a particular multifold into other multifolds at the same high-symmetry point but with different degeneracy. For example, in space group 198 a threefold at Γ splits into one fourfold fermion and one Weyl fermion.

In particular, for a generic threefold fermion occurring in the presence of spin orbit coupling the material-dependent parameter is no longer restricted to $\phi = \phi_0$, and can take values in the range $\pi/3 < \phi < 2\pi/3 \mod \pi/3$[70]. A change in ϕ will tilt the bands, breaking the full rotational symmetry (see Fig. 2.2). In this case, the selection rules of the symmetric model no longer apply and more excitations are allowed, as depicted in Fig. 3.3 (a), since the effective spin is no longer a good quantum number. The characteristic frequencies $\omega_i(\phi)$ associated to each transition depicted in Fig. 3.3 (a) can be obtained analytically[96]. For a threefold fermion described by Eq. 2.15 with an arbitraty value of ϕ, the activation frequencies are given by

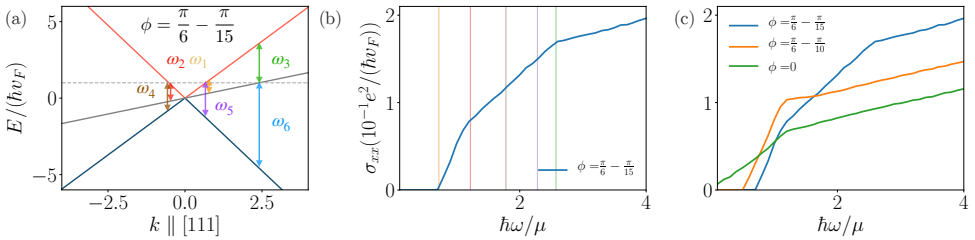

Figure 3.3: Band structure and optical conductivity of the non-symmetric ($\phi \neq \phi_0$) threefold fermion. (a) Band structure for $\phi = \pi/6 - \pi/15$ and the corresponding transitions allowed with their characteristic frequencies (Eq. 3.35). (b) Optical conductivity for the non-symmetric threefold fermion depicted in (a). The characteristic frequencies are represented by vertical lines with colors corresponding to the transitions depicted in (a). The frequencies ω_4 and ω_5 have little effect on the optical conductivity since they correspond to transitions with $\Delta s \neq \pm 1$, which are forbidden for the symmetric case $\phi = \phi_0$, and typically have smaller matrix elements than those with $\Delta s = \pm 1$. (c) Optical conductivities of non-symmetric threefold fermions for different values of the material-dependent parameter ϕ.

$$
\begin{aligned}
\omega_0 &= \mu \frac{\sqrt{3}\cos(\phi + \pi/6)}{\cos(\phi)}, & \omega_1 &= \mu \frac{\sqrt{3}\cos(\phi + \pi/6)}{\cos(\phi - 2\pi/3)}, \\
\omega_2 &= \mu \frac{\sqrt{3}\cos(-\phi + \pi/2)}{\cos(-\phi + \pi/3)}, & \omega_3 &= \mu \frac{\sqrt{3}\cos(\phi - \pi/6)}{\cos(\phi)}, \\
\omega_4 &= \mu \frac{\sqrt{3}\cos(-\phi + \pi/6)}{\cos(-\phi + \pi/3)}, & \omega_5 &= \mu \frac{\sqrt{3}\sin\phi}{\cos(\phi - 2\pi/3)}.
\end{aligned} \tag{3.35}
$$

The activation of new transitions at each ω_i in Eq. 3.35 results in a change in the linear dependence on ω of the optical conductivity, as depicted in Fig. 3.3 (b). Some transitions have a large effect on the slope, while others barely affect it. This is consistent with other optical effects in multifold fermions[96] and is rooted in the fact that the matrix elements for transitions with $\Delta s \neq \pm 1$ are typically smaller than those with $\Delta s = \pm 1$. In Fig. 3.3 (c) we plot the optical conductivity for different values of ϕ. Changing the value of ϕ shifts the characteristic frequencies according to their analytic expression $\omega_i(\phi)$, given in Eq. 3.35. As apparent in Fig. 3.3 (c), the slope of the optical conductivity also depends on ϕ, yet we find no closed analytic form for arbitrary ϕ.

We find a similar behavior in the fourfold case. For an arbitrary value of $\chi \neq \chi_0$ we lose full rotational symmetry (see Fig. 2.3) and the

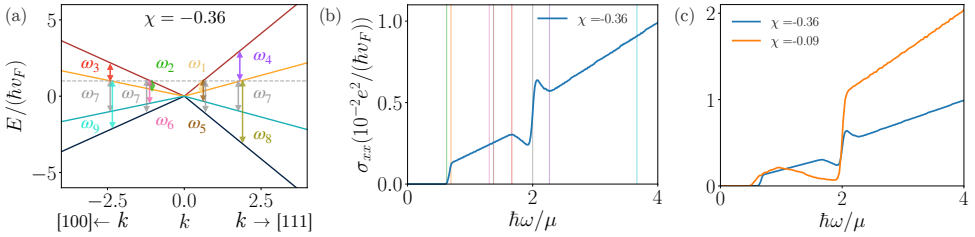

Figure 3.4: Band structure and optical conductivity of the non-symmetric ($\chi \neq \chi_0$) fourfold fermion. (a) Band structure for $\chi = -0.36$ and the corresponding transitions allowed with their characteristic frequencies (Eq. 3.36). (b) Optical conductivity for the non-symmetric fourfold fermion depicted in (a). The characteristic frequencies are represented by vertical lines with colors corresponding to the transitions depicted in (a). The frequencies that affect less the optical conductivity correspond to transitions with $\Delta s \neq \pm 1$, which are forbidden for the symmetric case $\chi = \chi_0$, and typically have smaller matrix elements than those with $\Delta s = \pm 1$. (c) Optical conductivities of non-symmetric fourfold fermions for different values of the material-dependent parameter χ.

spin-3/2 picture breaks down, allowing for new electronic excitations in the system (see Fig. 3.4 (a)). The characteristic frequencies for these excitations are given by[96]

$$\begin{aligned}
\omega_0 &= \mu\frac{E_1(\mathbf{k}^{111}) - E_2(\mathbf{k}^{111})}{E_1(\mathbf{k}^{111})}, & \omega_1 &= \mu\frac{E_1(\mathbf{k}^{100}) - E_2(\mathbf{k}^{100})}{E_1(\mathbf{k}^{100})},\\
\omega_2 &= \mu\frac{E_1(\mathbf{k}^{100}) - E_2(\mathbf{k}^{100})}{E_2(\mathbf{k}^{100})}, & \omega_3 &= \mu\frac{E_1(\mathbf{k}^{111}) - E_2(\mathbf{k}^{111})}{E_2(\mathbf{k}^{111})},\\
\omega_4 &= \mu\frac{E_1(\mathbf{k}^{100}) - E_3(\mathbf{k}^{100})}{E_1(\mathbf{k}^{100})}, & \omega_5 &= \mu\frac{E_1(\mathbf{k}^{111}) - E_3(\mathbf{k}^{111})}{E_1(\mathbf{k}^{111})},\\
\omega_6 &= \mu\frac{E_1(\mathbf{k}^{111}) - E_4(\mathbf{k}^{111})}{E_1(\mathbf{k}^{111})}, & \omega_7 &= \mu\frac{E_2(\mathbf{k}^{111}) - E_4(\mathbf{k}^{111})}{E_2(\mathbf{k}^{111})},\\
\omega_8 &= \mu\frac{E_2(\mathbf{k}^{100}) - E_4(\mathbf{k}^{100})}{E_2(\mathbf{k}^{100})},
\end{aligned} \tag{3.36}$$

where $\mathbf{k}^{100} = k(1,0,0)$ and $\mathbf{k}^{111} = k(1,1,1)/\sqrt{3}$. The activation of optical transitions at these frequencies can produce a change in the linear dependence on ω of the optical conductivity, as we see in Fig. 3.4 (b) and (c). However, the transitions with $\Delta s \neq \pm 1$, forbidden by the selection rules in the symmetric case, do not affect the optical conductivity for small deviations from the symmetric case, similar to what we observe in the threefold case.

We find that it is possible to identify generic threefold and fourfold

fermions in an optical experiment by their activation frequencies and linear dependence on ω, provided ϕ or χ and v_F are known (for example either from first-principle calculations or photemission data). The characteristic frequencies at which the optical conductivity changes and its linear dependence on ω are different for each multifold also in the non-symmetric cases, allowing us to identify them by their optical conductivity regardless of the value of ϕ or χ.

3.3 Imaginary part of the optical conductivity and sum rules

Before discussing realistic tight-binding models we note that so far we have calculated only the absorptive (real) part of the optical conductivity. Using the Kramers-Kronig transformations[94] we have obtained the dispersive (imaginary) of the optical conductivity in Appendix C, where we derive a general expression applicable to all symmetric and non-symmetric cases, and we compute it explicitly for the symmetric cases.

For completeness, in Appendix D we compute the conductivity sum rule, known as f-sum rule. The sum rule relates the integral over all frequencies of the real part of the optical conductivity, $\langle\sigma\rangle$, to the total number of particles. Since low-energy linearly dispersing bands, such as those of Weyl or multifold fermions, are unbounded, the f-sum rule explicitly depends on the cut-off scale Λ, similar to what is known for the low-energy model of graphene[52,100]. Leaving the closed form and details to Appendix D, we simply mention that for symmetric multifolds the sum rule of the interband part of the conductivity takes the form $\langle\sigma\rangle \propto (\Lambda^2 - c\mu^2)$ where c is a factor that depends on the type of multifold. Specifically $c = 1$ and $c = 4/3$ for the symmetric threefold and fourfold cases respectively. Thus, the sum rule provides another way to identify each multifold fermion by measuring their optical conductivity.

3.4 Optical conductivity of realistic tight-binding models

In the previous section we identified fingerprints of chiral multifold fermions in the optical conductivity using low-energy $k \cdot p$ models. To move one step closer to real materials, in this section we will use the tight-binding models of space groups SG199 and SG198[73,78,96] discussed in Sec. 2.3. We choose these two groups because, combined, they realize all types of chiral multifold fermions.

The tight-binding models that we consider here are built considering the crystal symmetries of the material, thus capturing the specific properties we are interested in such as the energy scales, the band connectivity and multifold crossings, and the orbital embedding. The latter describes the spatial position (or embedding) of the orbitals in real space. A change in the orbital embedding acts as a momentum dependent unitary transformation of the tight-binding Hamiltonian: it does not modify the band structure of the material, but modifies its eigenfunctions[96]. It is thus necessary to take it into account to give accurate predictions of observables, in particular the optical responses, and the details of this transformation depend on the space group. What these models do not capture is the orbital character of the material. In the next chapter we will discuss in more details how this affects our predictions for the optical conductivity of materials in SG198.

3.4.1 Space Group 199

The first tight-binding model that we consider describes a material in SG199 without spin-orbit coupling (see Sec. 2.3.1). At the moment of writing this thesis, no material has been found in this space group with only multifold fermions near the Fermi level[70]. Since we are interested in investigating the fingerprints of the multifold fermions in realistic models we present the results for this model in units of the characteristic hopping scale $t > 0$ and the lattice constant a.

In Fig. 3.5 (a) we show a representative band structure of a material in SG199. It features protected threefold nodes at the Γ point at energy $\mu_\Gamma/t = -1$ and at the $H = (-\pi, \pi, \pi)$ point at $\mu_H/t = 1$. It also

hosts two Weyl nodes at the $P = (\pi/2, \pi/2, \pi/2)$ point, and two Weyl nodes with opposite chirality at $-P$, at energies $\mu_{W_1}/t = -1.732$ and $\mu_{W_2}/t = 1.732$.

To focus on the optical conductivity of the threefold fermion in SG199, we can place the chemical potential slightly above the threefold node at the Γ point, at $\mu/t = -0.93$. We present the conductivity for this case in Fig. 3.5 (b). It has a linear dependence on the frequency ω and exhibits a change in the slope at $\hbar\omega_\Gamma/t = 0.07$. This result matches exactly the analytic results obtained for a threefold fermion in Eq. 3.31 in two ways. First the activation frequency $\hbar\omega_{3f}/t = \mu/t = 0.07$ exactly matches the distance from the node to the Fermi surface. Second, the numerical slope coincides with the slope determined by the effective Fermi velocity that we obtain by projecting the tight-binding Hamiltonian on the three eigenstates corresponding to the Γ point. This projection can be brought to the form of the threefold model in Eq. 2.15 with a unitary transformation[77], with an effective Fermi velocity $v_F = at/(2\hbar)$, where a is the lattice constant and t is the hopping parameter in the tight-binding model.

If we instead place the chemical potential at $\mu/t = -1.7$, near the lower Weyl node at energy μ_{W2} around P, we can focus on the optical conductivity of this Weyl node. We can see in Fig. 3.5 (c) that it has a linear dependence on the frequency ω and a change in the slope at $\hbar\omega_P/t = 0.064$. This energy scale matches that of a Weyl fermion (see Table 3.1) with an activation frequency of $\hbar\omega_W/t = 2\mu/t = 0.064$, corresponding to twice the distance from the node to the Fermi surface. The slope matches that of Eq. 3.30 using the effective Hamiltonian around the P point. We obtain this model by projecting the Hamiltonian on the corresponding eigenstates near the Weyl node and bringing it to a Weyl Hamiltonian form $H = \hbar v_F \mathbf{k}\cdot\boldsymbol{\sigma}$ with a unitary transformation, where $v_F = at/(2\sqrt{3}\hbar)$[77].

3.4.2 Space Group 198: RhSi

The next model that we consider describes a material in SG198 (see Sec. 2.3.2). In the next chapter we will compute the optical conductivity of RhSi and CoSi using tight-binding parameters fitted to *ab-initio*

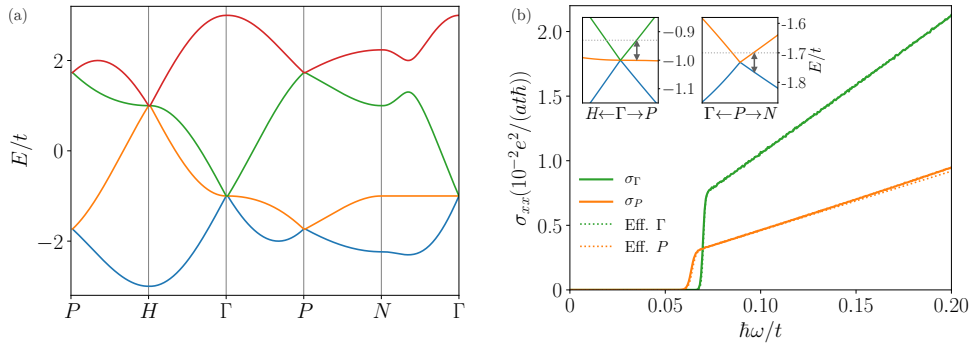

Figure 3.5: Band structure and optical conductivity of the tight-binding model for a material in SG199. (a) Band structure of the tight-binding model used in Sec. 3.4.1 (Eqs. 2.29–2.30). (b) Optical conductivity of the tight-binding model calculated with a chemical potential $\mu/t = -0.93$ (solid green line), separating by 0.07 the threefold node at the Γ point and the Fermi level (left inset). In solid orange the optical conductivity calculated for the tight-binding model with $\mu/t = -1.7$, separating by 0.032 the lower Weyl node at the P point and the Fermi level (right inset). We present the optical conductivity of the effective models described in 3.4.1 for the Γ point (dashed green) obtained with Eq. 3.31, and for the P point (dashed orange) obtained with Eq. 3.30. In the frequency range $0 < \hbar\omega/t < 0.2$ the optical conductivity is well described by the linear effective model, *i.e.* the solid and dashed lines fall on top of each other. The orbital embedding does not affect the results at these energy scales. These results are obtained with $1/\beta = 5 \times 10^{-4}t$.

calculations. In the remaining of this chapter we well compute the optical conductivity of the tight-binding model for SG198 with the parameters obtained for RhSi in Ref. [78], focusing on the response of different multifold fermions in the Brillouin zone, setting the first understanding to build a more complete description in the next chapter.

In Fig. 3.6 (a) we present the band structure for the tight-binding model of SG198 (Eqs. 2.34–2.35) — without spin-orbit coupling — for the tight-binding parameters in Ref. [78]. It exhibits a protected threefold crossing at the Γ point at $\mu_{3f} = -0.07$ eV and a protected fourfold crossing (double spin-1/2) at the $R = (\pi, \pi, \pi)$ point at $\mu_{4f} = -0.48$ eV.

It is instructive to place the chemical potential close to the threefold at Γ ($\mu = 0.065$ eV) to compare it with the optical conductivity of the linear low-energy model. In Fig. 3.6 (b) we present the results obtained numerically choosing the orbital embedding for RhSi ($x = 0.3959$), the results without orbital embedding ($x = 0$) and the analytic results for the effective model obtained following the projection procedure described for SG199 in the previous section. As for SG199 the projection around Γ results in the effective Hamiltonian Eq. 2.15 with $v_F = at/(2\hbar)$, where $a = 4.6$ Å for RhSi and with $t = v_p = 0.76$ eV extracted from the tight-binding fit to the DFT bands in Ref. [78]. Fig. 3.6 (b) shows that the numerical results match the optical conductivity of the effective model for $\omega \lesssim 12$ meV, they grow linearly with ω and have a step at $\omega_\Gamma = 5$ meV, which is the energy separation from the node to the Fermi surface. For $\omega \gtrsim 12$ meV the quadratic corrections become important, and the optical conductivity calculated with the tight-binding model departs from the linear dependence obtained for the effective model. At the same scale, the results obtained for $x = 0$ and $x = 0.3959$ do not match exactly, which indicates that the higher-order corrections are sensitive to the orbital embedding unlike the linear approximation.

We now consider the natural position of the Fermi level with chemical potential $\mu = 0$ and the orbital embedding for RhSi $x = 0.3959$. We recall that for $\mu = 0$, the Fermi level lies 0.07 eV above the threefold fermion at Γ, and 0.48 eV above the fourfold node at the R point.

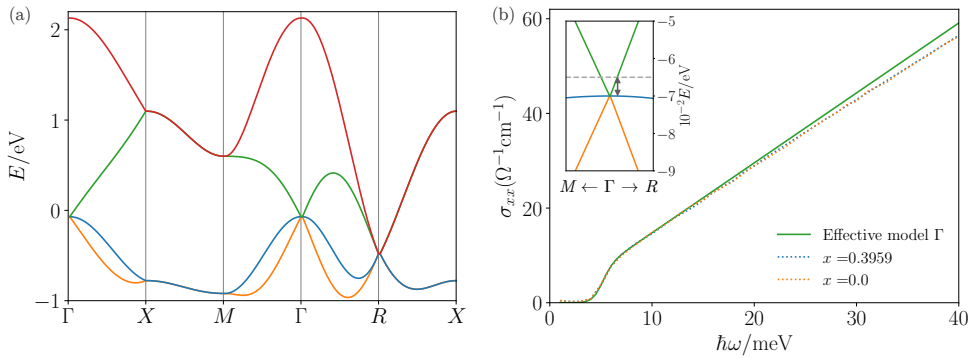

Figure 3.6: Band structure and optical conductivity of the tight-binding model for a material in SG198. (a) Band structure of the tight-binding model of RhSi used in Sec. 3.4.2 (Eqs. 2.34–2.35). (b) Optical conductivity corresponding to excitations near the Γ point calculated for $1/\beta = 0.5$ meV ($T = 5.8$ K), including the spin degeneracy and $\mu = 65$ meV. The latter sets an energy difference of 5 meV between the threefold node at the Γ point and the Fermi level (inset). The results without taking into account the orbital embedding (dashed orange line) and with the orbital embedding for RhSi (dashed blue line) are close in the range of frequencies plotted, $0 < \omega < 40$ meV. The numerical results obtained for the tight-binding model (dashed lines) are similar to the optical conductivity of the effective model at Γ (green line) discussed in Sec. 3.4.2 for $\omega \lesssim 12$ meV, and exhibit a jump at $\omega = 5$ meV, a characteristic of the threefold fermion. For higher frequencies the linear effective model fails to capture the curvature of the bands where higher-order terms become important, causing the optical conductivity to deviate from that of the tight-binding model.

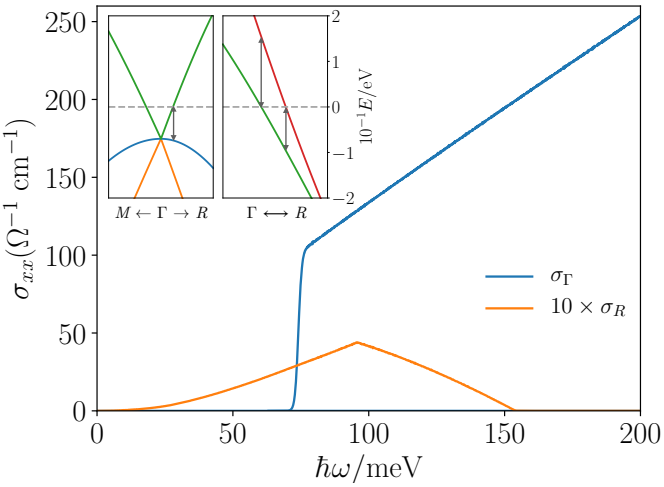

Figure 3.7: Optical conductivity of the tight-binding model for SG198 fitted to RhSi[78,96] including the spin degeneracy, with $\mu = 0$ eV and $1/\beta = 0.5$ meV ($T = 5.8$ K). The contribution of the Γ point (blue line) is activated by excitations between the intermediate band (left inset, blue line) to the upper band (left inset, green line), and exhibits a jump near $\omega = 74$ meV, which is larger than $|\mu_{3f}| = 70$ meV, set by the concavity of the intermediate band. The contribution due to excitations near the R point (orange line) is magnified by a factor 10 for comparison. This contribution is activated by transitions between the intermediate-upper (green) and upper band (red), depicted in the right inset. The characteristic frequencies, represented by vertical arrows in the right inset, correspond to the maximum value of σ_R at $\omega = 96$ meV and it vanishes at $\hbar\omega = 154$ meV.

For these material parameters, and in the $0 < \hbar\omega < 200$ meV frequency range, the interband optical conductivity has contributions from transitions close to the Γ and R points, that we present separately in Fig. 3.7. The contribution to the conductivity near the Γ point exhibits a jump at a frequency $\hbar\omega_\Gamma = \mu_{3f} = 74$ meV, which is slightly larger than the corresponding characteristic frequency of a threefold fermion $\hbar\omega_{3f} = 70$ meV (see Table 3.1). This is due to the curvature of the intermediate band, which results in a higher activation frequency for the allowed transition near the Γ point (see left inset in Fig. 3.7).

Near the R point, the only transitions that contribute below $\hbar\omega < 4\mu_f \sim 1$ eV are the interband transitions from the intermediate-upper band (green) to the upper band (red), that we depict in Fig. 3.7, right inset. Their contribution to the conductivity is two orders of magnitude smaller compared to that associated to the Γ point (see Fig. 3.7). This small magnitude is to be expected once we recall that at low energies, near the node at R, these two bands correspond to two decoupled Weyl fermions (see Fig. 3.6 (a)), and the transitions between them are forbidden. As we increase the energy, the matrix elements grow as the bands separate. Since the separation is small, the matrix elements are small. The two extremal energies, depicted by the arrows in the right inset of Fig. 3.7, correspond to the frequencies $\hbar\omega = 96$ meV and $\hbar\omega = 154$ meV, which match the scales where the R point conductivity reaches its maximum and vanishes, respectively (see Fig. 3.7).

In summary, the interband optical conductivity of this model for the tight-binding parameters in Ref. [78] in the frequency range $\hbar\omega < 200$ meV is determined by that of the threefold fermion at the Γ point, since the contribution of the fourfold at the R point is two orders of magnitude lower.

This study of the features of the tight-binding for SG198 model will be crucial to understand and explain the experimental data of the optical conductivity of RhSi and CoSi in the next chapter.

3.5 Conclusions

In this chapter we have derived the expression for the linear optical conductivity in the length gauge. Using that expression and the $k \cdot p$ models in Chapter 2, we have shown that, per node, multifold semimetals have larger optical conductivity than Weyl semimetals. They also feature characteristic activation frequencies that are specific to each class of multifold degeneracy. These activation frequencies, as well as the slope of the conductivity as a function of frequency, can be used as a fingerprint to distinguish each chiral multifold crossing. We have considered multifold fermions in rotationally symmetric and non-symmetric cases, and realistic hamiltonians in space groups 199 and 198. We have used tight-binding parameters that allowed us to explore the properties of both models. In the next chapter we will use the tight-binding model for SG198 to characterize the optical conductivity of RhSi and CoSi.

4

Linear optical conductivity of CoSi and RhSi

Experimental fingerprints of chiral multifold fermions in real materials

4.1 Introduction

Two of the most promising candidates to host multifold fermions near the Fermi level are RhSi and CoSi, both crystallizing in SG198 (Fig. 4.1). The presence of multifold fermions near the Fermi level is responsible for many interesting optical phenomena, such as gyrotropy[101,102] and the quantized circular photogalvanic effect (CPGE)[62,71,85,103,104]. However, a solid understanding of the effect of multifold fermions on the optical responses of RhSi and CoSi is still lacking.

The first experimental evidence of the existence of multifold fermions was based on band structure measurements, such as ARPES[90,91,105]. However, accessing the energy ranges involved in the fine details of the band structure, such as SOC band-splitting, usually in the range of meV (see Fig. 4.2), is challenging. As discussed in Chapter 3, the optical conductivity can reveal details at small energy scales, and it provides information about the band structure and the wave functions of occupied and unoccupied states. These features make it an excellent physical observable to probe multifold fermions in real materials. Furthermore, in order to understand and interpret the second-order optical responses in topological semimetals, such as second-harmonic generation[66,67] and photogalvanic effects [106–112], a precise measurement of the optical conductivity is crucial, together with precise knowledge of the chemical potential in the sample, the carrier lifetime, and the energy range where topological crossings are activated[75,111,113].

The two materials studied in this chapter — RhSi and CoSi — have the same symmetries and the same multifold fermions at the same high-symmetry points. However, both materials are different in some key aspects. The first of them is the bandwidth involved in the

optical excitations between topological bands, which is considerably larger in RhSi than in CoSi (see Fig. 4.1). Another difference is the energy separation between the threefold node at the Γ point and the double-Weyl crossing at the R point. While in CoSi this energy difference is of $\sim$ 0.2 eV, in RhSi they are separated by $\sim$ 0.4 eV (Fig. 4.1). This gives a much larger energy window where the dominating contributions to the optical conductivity are transitions coming from the threefold fermion at the Γ point. In this chapter we study of the optical conductivity of these materials to determine their chemical potential, their carrier lifetime, and to identify signatures of chiral multifold fermions.

In Chapter 3 we obtained an expression for the optical conductivity and studied the signatures of each type of multifold fermion using low-energy $k \cdot p$ models. After identifying the fingerprints of each multifold fermion in the optical conductivity using the simplest model, we studied the main characteristics of the generic tight-binding models for SG198 and SG199. In this chapter we will analyze the experimental optical conductivity of CoSi[114] and RhSi[75]. We will base our comprehensive analysis on the theoretical calculations with the $k \cdot p$ model and tight-binding model for SG198, complemented with *ab-initio* results, to explain the experimental behaviour of the optical conductivity in CoSi and RhSi. This will allow us to gain a deeper understanding of the mechanisms involved in the optical responses of multifold fermions, and remark the advantages and limitations of the different models that can describe them.

4.2 CoSi

In this section we present a comprehensive study of the optical conductivity of CoSi. This material has some features that make it an ideal platform for revealing the signature of multifold fermions in an optical conductivity experiment. It has a low carrier density, a large energy window where only optical transitions between topological bands are involved — Lifshitz energy — of ~ 0.6 eV[72,74,90,91,105], and the energy separation between the multifold nodes at Γ and R is ≈ 0.2 eV, with no other bands expected at the Fermi level[90,91,105] (see Fig. 4.1 (b)).

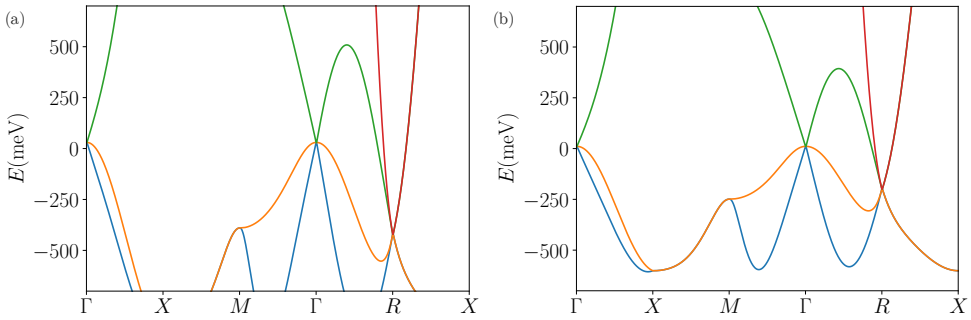

Figure 4.1: Band structures of RhSi and CoSi. Both materials crystallize in SG198, thus exhibiting a threefold fermion at the Γ point and a double-Weyl fermion at the R point. However, the overall energy scale involved in RhSi (a) is larger than in CoSi (b), which translates into a larger energy window where only optical transitions between topological bands are involved (Lifshitz energy) in RhSi. The energy separation between the threefold fermion at the Γ point and the double-Weyl fermion at the R point in RhSi (a) is $\sim$ 0.4 eV, while in CoSi (b) is $\sim$ 0.2 eV. The tight-binding parameters for RhSi (a) are $v_1 = 1.95$, $v_p = 0.77$, and $v_2 = 0.4$, and for CoSi (b) $v_1 = 1.29$, $v_2 = 0.25$ and $v_p = 0.55$.

For incident light energies below 0.2 eV, interband excitations near the multifold crossing at the R point are expected to be Pauli-blocked, leaving only the linearly dispersing multifold fermions at the zone center[115,116]. The large Lifshitz energy and the separation between multifold nodes are key to observe a clean linear relation between the conductivity and frequency as predicted for multifold fermions (see Chapter 3) and to provide a good platform to understand why and how deviations could occur. The optical conductivity of CoSi was first measured more than two decades ago, but the topological properties of CoSi and their implications for the optical response were not addressed, since the topology of CoSi was not known until very recently[72,90,91,105]. The relation of the optical conductivity with the topological properties is the subject of this chapter.

4.2.1 Experimental features of the optical conductivity

The optical conductivity of CoSi was measured using Fourier-transform infrared (FTIR) spectroscopy over a range of 40 to 50000 cm^{-1} for temperatures ranging from 10 K to 300 K. The measurements were performed for two different samples, one grown using chemical vapor

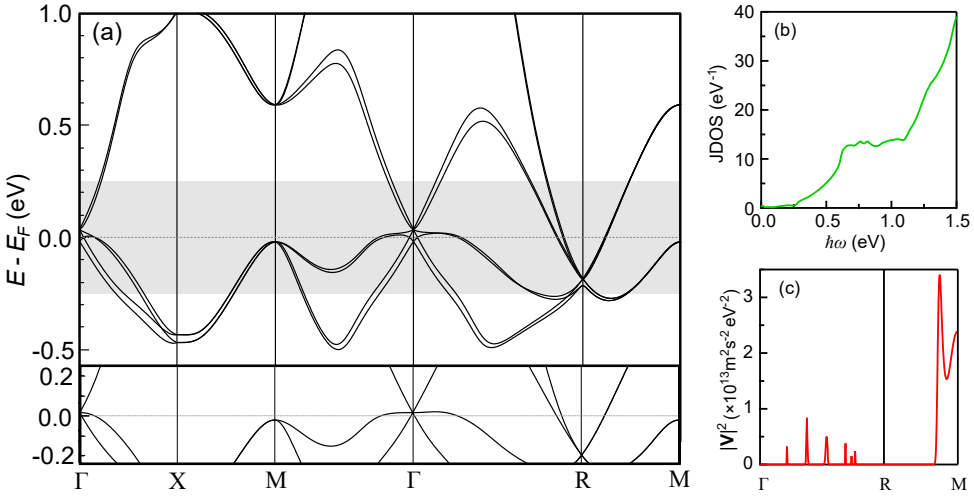

Figure 4.2: DFT band structure, JDOS, and matrix elements of CoSi. (a) Band structure of CoSi with spin-orbit coupling. The bottom inset shows the band structure without spin-orbit coupling in the same shaded energy window of (a). (b) Joint density of states as a function of energy. (c) Momentum-resolved matrix elements that contribute to the 0.62 eV interband transition along $\Gamma - R - M$ direction. Adapted from Ref. [74].

transport (CVT) method[105] and the other with a flux method[117]. In this section we will focus on explaining the experimental data for the CVT sample. The differences between both samples are discussed extensively in Ref. [74].

In Fig. 4.2 (a) we see that the multifold crossing at the zone center is close to the Fermi level, and transitions near the R point are Pauli-blocked, which means that the low-energy optical conductivity must be dominated by optical transitions near the Γ point. The spin-orbit splitting in the material is weak, approximately 18.1 meV at the zone center (Fig. 4.2 (a)). This suggests that a model without spin-orbit coupling is sufficient to describe the coarse features, broader than this energy scale, while spin-orbit coupling can explain features of the response at finer energy scales.

The measured optical conductivity of CoSi is shown in Fig. 4.3 (a) for different temperatures. In order to understand the features of the experimental data and trace back their origin to the band structure of CoSi, we reproduce in Fig. 4.2 the DFT band structure for CoSi originally presented in Ref. [74], and the corresponding predicted optical conductivity in Fig. 4.3 (b).

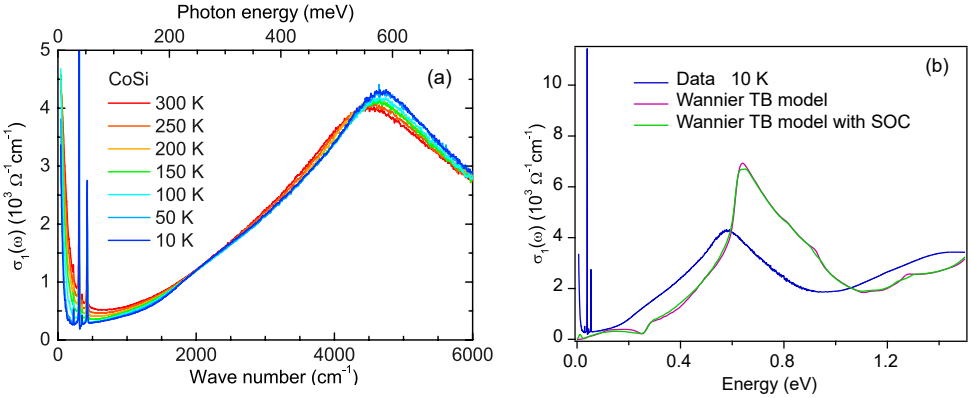

Figure 4.3: Experimental optical conductivity of CoSi. (a) Temperature-dependent optical conductivity spectra $\sigma_1(\omega)$ of a CVT-grown CoSi (001) crystal. (b) Measured optical conductivity at 10 K along with the Wannier tight-binding calculation with and without spin-orbit coupling at 10 K. Adapted from Ref. [114].

We will analyze the experimental features of the optical conductivity from high to low energies. Before studying the tight-binding model and the low-energy scale of the optical conductivity, let us first focus on the measured peak around 0.6 eV, which is only due to interband transitions. The calculated DFT optical conductivity (Fig. 4.3 (b)) shows a peak at $\omega \approx 0.62$ eV, the position of which matches well with the experimentally-observed peak. Contributions to the conductivity peak come from all transitions at the peak energy range which are not Pauli-blocked and have nonzero velocity matrix elements.

The joint density of states (JDOS), shown in Fig. 4.2 (b), is a measure of the number of transitions at a given energy, and is thus a significant indicator for the origins of the observed peak. The JDOS corresponding to two bands n, m can be expressed as[118]

$$\mathrm{JDOS}_{nm}(\hbar\omega) = \int_{\mathrm{BZ}} \frac{d\mathbf{k}}{(2\pi)^3} \delta(E_n(\mathbf{k}) - E_m(\mathbf{k}) - \hbar\omega), \tag{4.1}$$

where the delta function in the integrand gives a nonzero contribution when the bands n and m are separated by an energy $\hbar\omega$.

The JDOS shows strong variations in the neighbourhood of critical points in the band structure, and can help us identify the origin of different features in the optical conductivity. For a detailed study of

the JDOS and how it behaves at different critical points see Chap. 5 of Ref. [118].

In Fig. 4.2 (b) the JDOS exhibits a shoulder-like feature at ≈ 0.62 eV. This shoulder-like feature is characteristic of a saddle point[118], a critical point in the band structure that is neither a local maximum or minimum but has vanishing $\mathbf{k}-$derivative. This shoulder-like feature of the JDOS suggests that the interband contributions at $\hbar\omega \approx 0.62$ eV primarily originate from the M point, which is a saddle point in the band structure of CoSi. The JDOS is a momentum-integrated quantity; therefore, to unambiguously determine which interband transitions give rise to the peak, we plot the (momentum-resolved) matrix elements of Eq. 3.27 in Fig. 4.2 (c). In particular, in Fig. 4.2 (c) we show the quantity

$$|V(\mathbf{k})|^2 = \sum_{n\neq m} \frac{f_{nm}(\mathbf{k})}{E_{mn}} |v^a_{nm}(\mathbf{k})|^2 \delta(E_{mn} - \hbar\omega), \tag{4.2}$$

where $f_{nm}(\mathbf{k}) = f_n(\mathbf{k}) - f_m(\mathbf{k})$, E_{mn} is the energy difference between bands m and n, and $v^a_{nm}(\mathbf{k})$ is the velocity matrix element between bands n, m. We calculate $|V(\mathbf{k})|^2$ for fixed energy $\hbar\omega = 0.62$ eV along $\Gamma - R$ and $R - M$, which is a measure of the matrix elements of all allowed transitions at the peak energy. Fig. 4.2 (c) clearly confirms that the interband transitions giving rise to the peak originate mainly from the vicinity of the M point, which was assigned to optical transitions between the lower an upper bands of the double-Weyl fermion along the $\Gamma - R$ direction in previous works[111,116,119].

A second feature of the calculated DFT conductivity shown in Fig. 4.3 (b) is a dip at around 0.25 eV. As we will see later, this feature is present in the tight-binding model prediction as well. This is due to the curvature of the middle band in the threefold node at the Γ point. When the energy of the incoming photon is very small, the allowed transitions should occur between the lower band and the middle band at momenta right near Γ (see Fig. 4.2 (a)). Away from Γ, the middle band curves downward in energy and becomes occupied, thus blocking transitions from the lower band to the middle band and providing the downward dip in the spectrum. As the energy of the incoming photon increases further, the transitions around the R point become activated, providing

the recovery from the dip and the continuation of the spectrum upward. However, this dip is not observed in experiments, probably due to a short lifetime of the hot carriers around 0.25 eV as decreasing the quasiparticle lifetime by broadening the Dirac delta function smears out this dip feature[116].

Finally, we focus on the optical conductivity below 0.2 eV. In order to compare the calculation results with experiment below 0.2 eV accurately, we need to extract the interband contribution from the experimental data by subtracting the sharp Drude and phonon responses at low energy. To isolate the interband contribution we fit the low-energy response to the Drude model in Eq. 3.29. This fit allows us to extract a Drude width of $\approx$ 3 meV at 10K an obtain an estimation of the Fermi velocity of the carriers dominating the intraband contribution. We estimated this Fermi velocity v_F^R for the double-Weyl fermions is around 1.4×10^5 m/s, which agrees within 5 % with the DFT calculation in Fig. 4.2 (a), bottom. This agreement indicates that the narrow Drude response comes from the electron pocket with double-Weyl quasi-particles at R.

4.2.2 Low-energy regime: $k \cdot p$ and tight-binding models

After subtracting the intraband contribution, we study the low-energy features of the interband optical conductivity. The most striking feature of the interband optical conductivity is its approximately linear behavior up to $\sim$ 0.2 eV. Below $\sim$0.2 eV, vertical transitions at the R point are Pauli blocked, as is clear from Fig. 4.2 (a), except for the tiny peak at $\hbar\omega \sim 11$ meV shown in the green curve in Fig. 4.3 (b), which is associated with the interband transitions between spin-orbit split bands along the $R - M$ line. The contribution from these transitions is much smaller, however, than the vertical transitions from the multifold fermions at the Γ point (see Sec. 3.4.2). Therefore, the linear conductivity below 0.2 eV is mainly attributed to interband transitions near the Γ point.

To quantitatively understand the linear slope of the observed conductivity, and to determine whether it originates from the low-energy multifold fermions, we now analyze the low-frequency regime

of the optical conductivity in detail. As a first step, we consider the $k \cdot p$ model for the threefold spin-1 threefold fermion (Eq. 2.15) to describe the multifold crossing at the Γ point in the absence of spin-orbit coupling (see lower panel of Fig. 4.2 (a)). As discussed in Chapter 3, interband transitions are allowed from the partially occupied lower linear band to the central flat band, but are forbidden between the two linearly dispersing bands due to angular momentum selection rules. For this model, the optical conductivity is given by Eq. 3.32. The only free parameter is the Fermi velocity, which is obtained by fitting the linear model to the DFT bands near the Γ point wihout spin-orbit coupling (Fig. 4.2 (a)). We find a Fermi velocity $v_F^{\Gamma} = 1.9 \times 10^5$ m/s. The corresponding result for the linear model, shown in Fig. 4.4 (b)-(c), falls lower than the experimental curves for both samples.

To better understand the origin of the discrepancies, we go beyond the linear model and compare the optical conductivity data to that obtained by the tight-binding model for SG198 fitted for CoSi, and a Wannier tight-binding model based on the DFT calculation discussed previously in this section[114].

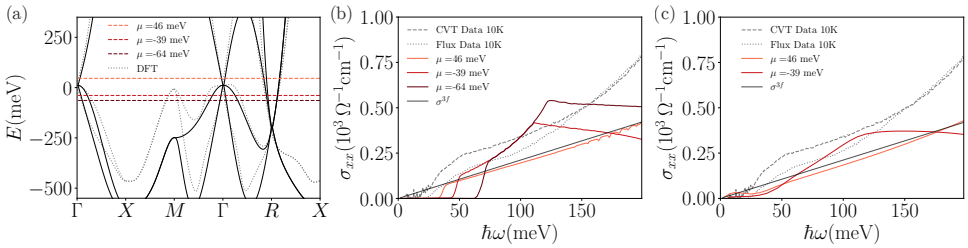

Figure 4.4: Tight-binding model for SG198 fitted to the Γ point of CoSi. (a) Band structure of CoSi obtained using the tight-binding model for SG198 (Eqs. 2.34–2.35) with $v_1 = 1.29$, $v_2 = 0.25$, and $v_p = 0.55$ compared to DFT bands (dotted grey). Fermi levels for different chemical potentials are marked as horizontal dashed lines. (b) Optical conductivity for the chemical potentials shown in (a) with no broadening. For reference we show as a solid line the optical conductivity of a threefold fermion $\sigma^{3f} = \frac{\omega}{3\pi v_F}$ with $v_F = v_p/2$. (c) Optical conductivity at two fixed chemical potentials, one above and one below the Γ node, calculated with a finite broadening of 12 meV.

To describe CoSi, we set the orbital embedding (see Sec. 2.3.2) for CoSi to $x_{\mathrm{CoSi}} = 0.3865$[120,121], and find v_1, v_p, and v_2 by fitting the tight-binding spectrum to the DFT bands. To capture the separation in energy between the multifold nodes at Γ and R, we fix it to match that found by DFT, which equals 210 meV. By expanding the tight-binding

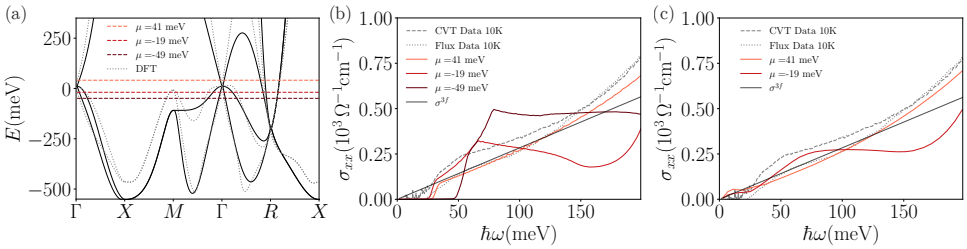

Figure 4.5: Tight-binding model for SG198 fitted to the R point of CoSi. (a) Band structure of CoSi obtained using the tight-binding model for SG198 (Eqs. 2.34–2.35) with $v_1 = 1.29$, $v_2 = 0.25$, and $v_p = 0.41$ compared to DFT bands (dotted grey). Fermi levels for different chemical potentials are marked as horizontal dashed lines. (b) Optical conductivity for the chemical potentials in (a). For reference, we show as a solid line the optical conductivity of a threefold fermion $\sigma^{3\mathrm{f}} = \frac{\omega}{3\pi v_F}$ with $v_F = v_p/2$. (c) Optical conductivity at two fixed chemical potentials, one above and one below the Γ node calculated with a finite broadening of 12 meV.

Hamiltonian for SG198 (Eq. 2.35) to linear order in momentum around Γ and R, we see that the parameter v_p sets the Fermi velocity of the threefold and double-Weyl fermion at the Γ and R points to $v_F^{\Gamma} = v_p/2$ and $v_F^{R} = v_p/(2\sqrt{3})$, respectively[77]. The fitted values of v_1, v_p, and v_2 adequately describe the band structure, but lead to an inaccurate value of the Fermi level compared to the DFT calculation. To set the right energy scale in the tight-binding model we add a constant energy shift of $E_0 = 0.551$ eV, $H = H_{198}(v_1, v_p, v_2; x) + (E_0 - \mu)\mathbb{I}_{4\times4}$. All chemical potentials are measured with respect to this energy shift.

It is illustrative then to compare two different fits, one that matches well the Fermi velocity near the Γ point, and a second one to match the Fermi velocity at the R point. The first fit sets $v_p = 0.55$ to fit the Fermi velocity of the bands near the Γ point (see Fig. 4.4 (a)). Upon closer inspection, we find that it provides a better description of the upper band of the threefold crossing at the Γ point than that of the middle and lower bands. The second fit sets $v_p = 0.41$ to fit to the Fermi velocity of the bands near the R point (see Fig. 4.5 (a)). Despite being a good fit for the R point, we observe this to be a fair description also of the lower and middle bands at the Γ point away from the Γ node. For both fits, we obtain $v_1 = 1.29$ and $v_2 = 0.25$ for the remaining tight-binding parameters.

We must note that for both sets of parameters the tight-binding model fails to capture the flatness of the middle band near the Γ

point. Additionally, the tight-binding model is constructed considering s orbitals. Due to this limitation of the orbital character considered, this model fails to capture the behavior of the M point, which is not well described by s orbitals.

In Fig. 4.4 (b) and Fig. 4.5 (b) we compare the optical conductivities obtained for different chemical potentials crossing the node with no broadening. The (c) panels show the optical conductivity for selected chemical potentials and with a finite phenomenological Lorentzian disorder broadening of 12 meV. For both values of v_p, *i.e.* both fits, we find that a chemical potential that crosses the bands below the Γ node results in a peak and dip structure. In the case of $v_p = 0.55$, which amounts to $v_\mathrm{F} = 1.23$ eV·Å, the conductivity has an increasing trend when lowering the chemical potential. Specifically, the curve with $v_p = 0.55$, $\mu = -39$ meV shown in Fig. 4.4 (c) falls closest to the Wannier tight-binding calculation.

It is interesting to note that we obtain a good agreement between the four-band tight-binding model and the flux sample data for $v_p = 0.41$ with the chemical potential above the node and a 12 meV broadening (Fig. 4.5 (c)). However, this value of the chemical potential does not agree with the rest of our observations. As discussed at length in the experimental section of Ref. [114] and in Sec. 4.2.1, we find that CoSi is a compensated semimetal with a hole pocket at the Γ, implying that the chemical potential in the sample is below the node. In this case, the curve with $\mu = -39$ meV $v_p = 0.55$ in Fig. 4.4 (c) results in the best fit to the data and first-principles calculations.

Overall, this analysis establishes that the chemical potential lies below the threefold node at Γ and highlights that deviations from a linear band structure near multifold fermions have an important impact on the optical conductivity.

4.2.3 The role of spin-orbit coupling and the spin-3/2 multifold fermion

When we consider a finite SOC, the multifold fermions in the band structure of CoSi decompose into different multifold fermions (see Sec. 2.3.2 and Fig. 2.5). In particular, the threefold fermion at the Γ

point decomposes into a spin-3/2 fourfold fermion and a Weyl fermion separated by $\approx$ 18.1 meV. To assess the role of spin-orbit coupling and the splitting of the threefold fermion into a spin-3/2 fourfold fermion and a Weyl fermion, we compare the experimental data with the optical conductivity obtained from a Wannier tight-binding model based on the DFT calculation[114] presented in Fig. 4.2. This is a 64×64 (with spin-orbit coupling) tight-binding model in the basis of maximally-localized Wannier functions contructed with the Wannier90 package. The tight-binding model is fitted to the DFT band structure shown in Fig. 4.2, obtained with the software package Quantum Espresso[122–124]. Further details about this model can be found on Appendix C of Ref. [114].

The DFT-based Wannier tight-binding model result with spin-orbit coupling is represented by the green curve of Fig. 4.6. We have subtracted the small peak feature at 11 meV shown in Fig. 4.3 (b), since it originates from the interband excitations between spin-orbit-split bands along the $R - M$ line. The optical conductivity of the Wannier tight-binding model with SOC (green line in Fig. 4.6) is in better agreement with the measured conductivity in the flux-grown sample below 0.1 eV than the Wannier tight-binding model without SOC (pink line in Fig. 4.6). The spinless model shows an activation frequency at $\sim$ 0.01 eV, approximately half of the activation frequency observed in the experimental data and the model with SOC. Furthermore, the change of slope of the optical conductivity at $\sim$ 0.05 eV is well captured by the model with SOC, while the model without SOC fails to reproduce it. The optical conductivity in this energy region ($\sim$ 0.1 eV) is dominated by the optical transitions at the Γ point (see Fig. 4.2), where we find a spin-3/2 fourfold fermion and a Weyl fermion when SOC is considered. Thus, the agreement of the model with SOC with the experimetal data indicates that the low-frequency shoulder below 0.1 eV observed in experiments arises from transitions between the spin-3/2 fourfold node and the Weyl node at the Γ point. To the best of our knowledge, this spin-3/2 fourfold fermion at the Γ point is the first example of a spin-3/2 quasiparticle in a crystal.

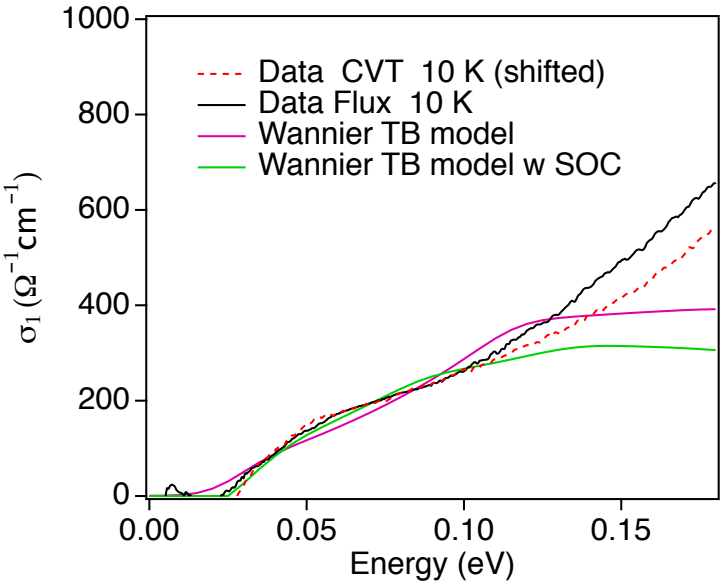

Figure 4.6: Interband optical conductivity in CoSi from measurements in both CVT- and flux-grown samples (red and black curves) along with Wannier tight-binding calculations without (pink curve) and with (green curve) spin-orbit coupling. Reproduced from Ref. [114].

4.2.4 Summary

In summary, we revealed the topological origin of the optical conductivity in CoSi. Our analysis shows that determining the location of the chemical potential accurately with respect to the central flat band is crucial to understand the optical response. We have shown that the interband optical conductivity in different frequency regimes is dominated by the existence of different topological multifold fermions and a saddle point in the band structure. Most notably, our analysis provides the evidence of the existence of the fourfold spin-3/2 quasi-particles for the first time. Our results provide a comprehensive picture of the optical conductivity of CoSi tracing back its features to the presence of multifold fermions in the band structure, and give an estimation of the scattering lifetime and chemical potential of the material. This knowledge of the optical conductivity is crucial to interpret the experimental data of second-order responses, such as the circular photogalvanic measurement in this family of

materials[62,75,103,111,113], and pave the way to study optical signatures in other chiral topological semimetals[70,85].

4.3 RhSi

In this section we will proceed in an analogous way to the case of CoSi to find the signatures of the multifold fermions in the optical conductivity, determine the position of the Fermi level and estimate the disorder scale in the sample. We will work with the tight-binding model for SG198 (Eqs. 2.34–2.35) fitted to the DFT band structure of RhSi presented in Ref. [75].

4.3.1 Experimental features of the optical conductivity

The optical conductivity of RhSi, shown in Fig. 4.7, is obtained by performing a Kramers-Kronig analysis on the frequency-dependent reflectivity $R(\omega)$ obtained by FTIR spectrometry in the frequency range from 0 to 8000 cm^{-1}(0 to 1 eV). The measurements were performed for several selected temperatures between 10K and 300K.

Let us start studying the intraband optical conductivity. We fit the optical conductivity at low frequencies with the Drude model in Eq. 3.29, similar to the procedure followed for CoSi in Sec. 4.2.1. After performing this analyisis we find the need for a broad (orange curve in Fig. 4.7) and a narrow (green curve in Fig. 4.7) Drude term to correctly account for the intraband response in RhSi, which indicates the existence of two types of charge carriers with very different transport scattering rates. This is a common scenario when describing the optical response of multiband systems, such as the iron-based superconductors[125–127].

In RhSi the threefold crossing is expected to be above the Fermi level. Examining the band structure in Fig. 4.8, the position of the Fermi level leads to the existence of a heavy hole pocket centered at the Γ point, and an electron pocket at the R point[72,103]. These two pockets are the source of the two different Drude peaks found in the intraband analysis (see

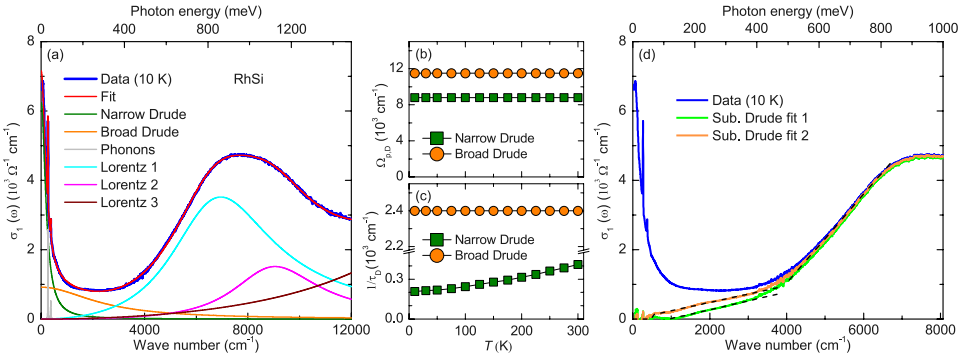

Figure 4.7: Experimental Drude and interband optical responses in RhSi. (a) Optical conductivity spectrum of RhSi up to 1.5 eV at 10 K. The thin red line through the data is the Drude-Lorentz fitting result, which consists of the contributions from a narrow Drude peak (green line), a broad Drude peak (orange line), and several Lorentz terms that account for the phonons (gray) and the interband transitions (light blue, magenta, and wine lines). Temperature dependence of (b) the plasma frequency $\Omega_{p,D}$ and (c) the transport scattering rate $1/\tau_D$ of the Drude terms. (d) Optical conductivity spectrum of RhSi at 10 K, and the corresponding spectrum after the Drude response and the sharp phonon modes have been subtracted. Black dashed lines are eye guidance for different quasi-linear regimes. Reproduced from Ref. [75].

Fig. 4.7). It is interesting to note that we could expect a third Drude peak from the pocket at the M point. Nevertheless, its contribution must be small, as the pockets at Γ and R are much larger and we do not need to include it to explain the low frequency data. We use the transport lifetime of the narrow Drude peak as the upper bound and estimate the transport lifetime $\tau_{300} \leq 13$ fs at 300 K and $\tau_{10} \leq 23$ fs at 10 K[75], consistent with previous studies[111,119]

We investigate now the interband optical conductivity. With the subtraction of two Drude peaks with transport scattering rates of 200 cm^{-1} and 2400 cm^{-1} (Drude fit 1 in Fig. 4.7 (d)), we find a quasi-linear behavior of $\sigma_1(\omega)$ in the low-frequency regime (up to about 3500 cm^{-1}). Such behavior is a strong indication for the presence of three-dimensional linearly dispersing bands near the Fermi level, as we established in Chapter 3. Indeed, from DFT band structure calculations (see Fig. 4.8), we see that this low-energy quasi-linear interband conductivity ($\omega < 3500$ cm^{-1}) could be attributed to the interband transitions around the Γ point. At higher energies, the interband contributions around the R point become allowed and can be responsible for the second quasi-linear interband conductivity region

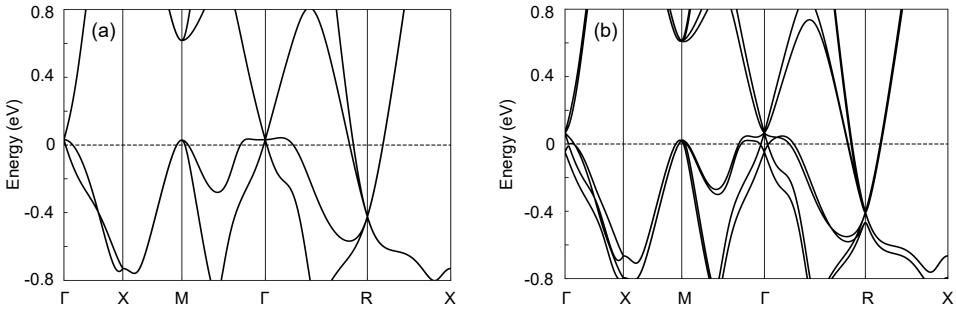

Figure 4.8: DFT band structure of RhSi (a) without spin orbit coupling, and (b) with spin orbit coupling. It hosts a threefold fermion at Γ and a double-Weyl fermion at R without spin orbit coupling. They split into a spin-3/2 fourfold node and a Weyl node at Γ, and a sixfold double spin-1 node and a twofold Kramers node at R, when spin orbit coupling is included. Reproduced from Ref. [75].

(3500 cm^{-1} $<$ ω $<$ 6500 cm^{-1}). At ω $>$ 6500 cm^{-1}, the optical conductivity flattens and forms a broad maximum around 8000 cm^{-1}. From Fig. 4.7 (a) we see that this maximum is well fitted with two Lorentzian distributions peaked around 0.85 eV (light blue) and around 1.1 eV (magenta). Following a symilar analysis to that of CoSi, we can attribute the peak around 0.85 eV to broadened interband transitions centered at the M point. This interpretation is different from previous explanations of this feature, such as that of Ref. [119].

When considering the interband optical conductivity obtained after subtracting the Drude contributions, it is important to note that the fit to the broader Drude peak might suffer from more uncertainty than that of the narrow Drude peak. Small changes in the width of the broad Drude peak might result in appreciable changes when subtracting it from the full data set to obtain the interband response. A different approach discussed in Ref. [75], where the two Drude and two phonon terms are subtracted directly, uses a smaller transport scattering rate of 1350 cm^{-1} (Drude fit 2 in Fig. 4.7 (d)). In this case, the onset frequency at which the interband conductivity emerges decreases and the magnitude of σ_1 below 4000 cm^{-1} increases with respect to the Drude fit 1. However, the resulting slope below 3500 cm^{-1} is not significantly modified as the wide Drude response contributes as a flat background in this regime. Note that another recent study used a similar method and also found that the quasi-linear behavior is robust within the uncertainty of the fit parameters[119]. Therefore, we conclude

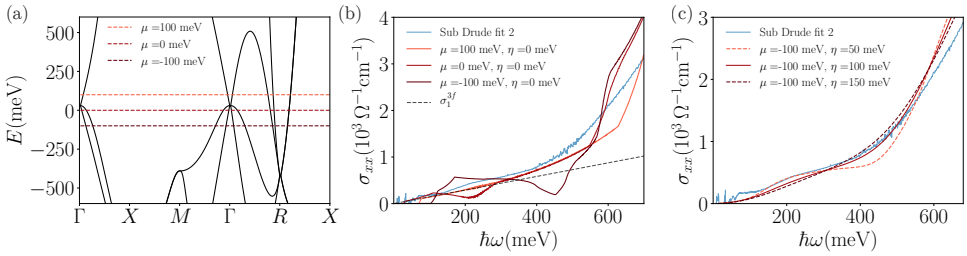

Figure 4.9: Tight-binding model for SG198 fitted to RhSi. (a) Band structure obtained using the tight-binding model (Eqs. 2.34–2.35) for RhSi without spin-orbit coupling with tight-binding parameters $v_1 = 1.95$, $v_p = 0.77$, and $v_2 = 0.4$. (b) Optical conductivity of RhSi for different chemical potentials μ without disorder broadening. The σ_1^{3f} conductivity by low-energy linear model is shown as a dashed gray line. (c) Optical conductivity of RhSi calculated with different disorder related broadenings, η, for $\mu = -100$ meV (see (b)).

that the low-frequency quasi-linear conductivity is contributed from interband excitations and will be analyzed next in our theoretical modeling.

4.3.2 Low-energy regime: $k \cdot p$ and tight-binding models

To understand better the low-frequency interband optical conductivity of RhSi, we compare the experimental results with the prediction of the $k \cdot p$ model for the threefold fermion at the Γ point (see Eq. 2.15), and the four-band tight-binding model for SG198 described in Sec. 3.4.2.

The band structure calculations of Fig. 4.8 suggest that at low frequencies $\omega \lesssim 0.4$ eV the optical conductivity is dominated by interband transitions close to the Γ point as the R point is 0.4 eV below the chemical potential. To linear order in momentum, the middle band at Γ is flat (see Fig. 4.8 (a)). The only free parameter of the optical conductivity of a threefold fermion (Eq. 3.32) is the Fermi velocity v_F, which can be obtained by fitting the linear model for a threefold fermion (Eq. 2.15) to the bands near the Γ point. The resulting optical conductity is shown in Fig. 4.9 (b). We observe that the low-energy σ_1^{3f} shows a smaller average slope compared to the low-energy part of our experimental data. In addition, a purely linear conductivity is insufficient to describe a small shoulder at around 200 meV.

Fig. 4.8 indicates that the position of the chemical potential combined with the deviations from linearity of the central band at Γ can play a significant role in optical transitions. These deviations are better captured by the tight-binding model for SG198, which can capture the downward curvature of the middle band. To adequately describe RhSi, we fit the tight-binding model for SG198 (Eq. 2.35) to the DFT band structure shown in Fig. 4.8, which results in a set of tight-binding parameters $v_1 = 1.95$, $v_p = 0.77$, and $v_2 = 0.4$. The DFT fit delivers parameters that differ from those obtained in Ref. [103], which we discussed in Sec. 3.4.2. Our current parameters result in a better agreement with the observed optical conductivity. Additionally, we rigidly shift the zero of energies of the tight-binding model by 0.78 meV to facilitate comparison with the DFT calculation. We set the orbital embedding parameter to $x_{\mathrm{RhSi}} = 0.3959$ for RhSi[71,115]. The resulting tight-binding band structure is shown in Fig. 4.9 (a).

To understand the role of chemical potential, in Fig. 4.9 (b) we compare the optical conductivity for different values of μ that leave the threefold node at Γ close to the Fermi level, and the experimental optical conductivity in the interval $\hbar\omega \in [0, 0.7]$ eV (sub. Drude fit 2). By choosing different chemical potentials below and above the node without yet including a hot-carrier scattering time τ, we observe that if the chemical potential is below the threefold node (see $\mu = 0, -100$ meV curves in Fig. 4.9 (b)), a peak appears (around 200 meV for $\mu = -100$ meV), followed by a dip in the optical conductivity at larger frequencies, before the activation of the transitions centered at the R point.

The peak-dip feature observed in the optical conductivity can be traced back to the allowed optical transitions and the curvature of the middle band. When the Fermi level lies below the node, the interband transitions with the lowest activation frequency connect the lower to the middle threefold band at Γ. Increasing the frequency could activate transitions between the bottom and upper threefold bands, allowed by quadratic corrections, but these are largely suppressed due to the selection rules, as the change of angular momentum between these bands is 2 (see Sec. 3.2.1). Because of the curvature of the middle band, the transitions connecting the lower and the middle threefold bands die out as frequency is increased further, resulting in the peak-dip structure visible in Fig. 4.9 (b). Since the curvature of the middle band is absent by construction in the linear model but captured by the tight-binding

model, it is only the latter model that shows a conductivity peak-dip. As a side remark, we observe that the transitions involving the R point bands activate at lower frequencies as the chemical potential is decreased.

Although placing the chemical potential below the Γ node results in a marked peak around 0.2 eV, it is clearly sharper and overshoots compared to the data, for which the sudden drop at frequencies above the peak is also absent. It is likely that this drop is masked by the finite and relatively large disorder-related broadening $\eta = \hbar/\tau$. This scale is expected to be large for RhSi given the broad nature of the low-energy Drude peak. Note that τ is the hot-carrier lifetime, which is different from the transport lifetime τ_D estimated from the Drude peaks. In Fig. 4.9 (c) we compare different hot-carrier scattering times for $\mu = -100$ meV. Upon increasing η the sharp features in Fig. 4.9 (b) are broadened, turning the sharp peak into a shoulder, similar to that observed in the experimental data. When $\eta = 100 - 150$ meV the resulting optical conductivity falls close to our experimental data, including the upturn at 0.4 eV, associated to the activation of the broadened transitions around the R point. Note that the large disorder scale is similar to the spin-orbit coupling (≈ 100 meV) and, therefore, disorder washes out any feature narrower than 100 meV and justifies our discussion based on a tight-binding model without spin-orbit coupling.

We note that despite the general agreement below 0.5 eV, the intuitive tight-binding calculations deviate from the data above 0.5 eV. This is likely due to the known limitations of the tight-binding model, which fails to accurately capture the band structure curvature and orbital character at other high-symmetry points such as the M point, which is a saddle point as discussed extensively for CoSi.

Overall, the curves with broadening factor $\eta = 100$ meV and with chemical potential below the nodes at Γ show a good qualitative agreement with the experimentally measured curve in a wide frequency range. This observation determines approximately the hot-carrier lifetime in RhSi to be $\tau = \hbar/\eta \approx 6.6$ fs.

4.3.3 Summary

The optical conductivity measurements, combined with tight-binding and *ab-initio* calculations, show that interband transitions $\lesssim 0.4$ eV are mainly dominated by the vertical transitions near the multifold nodes at the Brillouin zone center, the Γ point. We found that the transport lifetime is relatively short in RhSi, ≤ 13 fs at 300 K and ≤ 23 fs at 10 K. Our optical conductivity experiments are reasonably well reproduced by tight-binding and first-principle calculations when the chemical potential lies below the threefold node at the Γ point, crossing a relatively flat band, and when the hot-carrier lifetime is chosen to be $\tau \approx 4 - 7$ fs.

In conclusion, we have established a consistent picture of the optical transitions in RhSi using $k \cdot p$, tight-binding, and DFT methods applied to interpret the linear and nonlinear optical responses. Our analysis illustrates the crucial role played by the curvature of the flat-band at the Γ point and the saddle point at M. The interband optical conductivity shows two quasi-linear regions where the conductivity increases smoothly with frequency and a slope change around 0.4 eV. The slope in the first region is determined by a disorder-broadened contribution associated with a threefold fermion at the Γ point, while the slope in the second region is determined by the onset of a broadened R point conductivity.

4.4 Conclusions

In this chapter we provided a detailed explanation of the origin of the peak around 0.6 eV in the optical conductivity of CoSi, attributed to the saddle point at M. Thanks to our analysis, we know that the simplicity of the orbital character considered in the tight-binding model limits its capacity to describe the M point, and the predictions made using this model are bound by the dominance of the contributions coming from the M point. Additionally, the flatness of the middle band cannot be captured by the tight-binding model, limiting its capacity to describe adequately transitions at low energy in the flat region near the Γ point.

In both materials the low-energy optical conductivity is dominated by the multifold crossing at the Γ point. The analysis of the optical conductivity for RhSi and CoSi indicate that the position of multifold crossing at the Γ point with respect to the Fermi level plays a key role in the low-energy features of the optical conductivity. In both materials the Fermi level lies below the threefold node at Γ. However, in CoSi the Drude analysis indicates that the intraband response is dominated by the double-Weyl fermion at the R point, while in RhSi both Fermi surfaces at the Γ and the R points contribute to the intraband response.

In the case of RhSi, the optical conductivity is well explained by the tight-binding model for SG198 without SOC. The larger energy scale of the band structure (compared to that of CoSi) provides a larger energy window where the optical response is dominated by the bands at the Γ and R points, making the contributions of the M point appear at larger energies than in CoSi. Thus, the tight-binding model captures well the overall features of the band structure of RhSi above the disorder-induced broadening scale, leading to a good agreement between theory and experiment. Conversely, in CoSi the smaller energy scales and the dominance of the M point limit the validity of the tight-binding model to a smaller energy region compared to that of RhSi.

In RhSi the disorder-induced broadening is estimated to be $\eta \sim 100 - 150$ meV ($\tau \sim 4 - 7$ fs), which is large enough to mask the effect of spin-orbit coupling and the discrepancies between the tight-binding model and the experimental data due to the flatness of the middle band. However, in CoSi the disorder-induced broadening is $\eta \sim 3 - 12$ meV

($\tau \sim 55 - 200$ fs), small enough compared to the spin-orbit splitting at the Γ point ($\sim$ 20 meV). After ruling out other origins, such as the curvature of the middle band at the Γ point and the position of the chemical potential, we concluded that the optical conductivity features below 20 meV in CoSi are a result of the spin-orbit splitting of the multifold crossing at the Γ point, providing the first evidence of the existence of a spin-3/2 fermion in condensed matter.

5

Nonlinear optical responses

Second-harmonic generation in RhSi

5.1 The zoo of nonlinear responses

In Chapters 3 and 4 we studied the linear optical conductivity, which is proportional to the first power of the electric field and involves single-photon processes. At higher orders optical responses are proportional to higher orders of the electric field (Eq. 3.21), and multiple-photon processes can happen.

It is useful to make a distinction between even- and odd-order responses. The current induced in the marterial is odd under inversion symmetry, while even powers of the electric field are even under inversion symmetry. This leads to a clear distinction: odd-power responses are allowed in all cases, while even-power responses are only present when the system lacks inversion symmetry. Since even-order responses are only nonzero for materials without inversion symmetry they can be used as a test for spontaneous symmetry-breaking[128–133] and to study the surfaces and interface properties of materials[134–139], which always break inversion symmetry.

In this chapter we will focus on second-order responses induced by a monochromatic source of light with frequency ω. When we consider the second-order responses — proportional to the square of the electric field — the two Fourier components of the incoming light $+\omega$ and $-\omega$ can interfere constructively or destructively. Depending on this interference, the resulting effects are radically different, allowing us to explore different material properties.

When both Fourier components have opposite sign the result is a DC current in the material ($\omega = 0$) known as the bulk photogalvanic effect (BPGE). This current can be divided into two different components:

the first of them is a non-oscillating photocurrent that grows linearly in time, known as injection current; the second component, known as the shift current, does not depend on time. In the presence of time-reversal symmetry, we can relate univoquely each of the two components with linear or circular light polarization: linearly-polarized light will give rise to the linear photogalvanic effect (LPGE), determined by the shift current, while circularly-polarized light will produce a circular photogalvanic effect (CPGE), determined by the injection current*.

When both Fourier components are equal the generated current oscillates at frequency 2ω, known as second-harmonic generation (SHG). The SHG is at the core of the technologies for generating light sources at different wavelengths[140,141]. Therefore, finding materials where the second-harmonic response is large is not only a quest for understanding this phenomenon, but also a contemporary material science challenge with solid technological interest.

Beyond the potential technological applications, the microscopic origin of large second-harmonic responses is an open scientific question. Two recent studies[66,67] reported a giant SHG response in the topological semimetal TaAs at $\omega \sim 1.5$ eV (800 nm)[66], reaching a maximum value one order of magnitude larger than the benchmark materials GaAs[142] and ZnTe[143]. The incoming photon energy scales involved in these responses ($\sim$ eV) are considerably larger than the ~ 60 meV associated with the topological band crossings, the Weyl nodes, present in TaAs. Therefore, the existence of topological band degeneracies alone cannot explain the giant second-harmonic response, and a general microscopic origin has yet to be uncovered. In fact, the role of topological band crossings with linear dispersion, such as Weyl nodes, in the SHG is experimentally unclear.

In this chapter we study the second-harmonic generation in RhSi. The intricate combination of linear and topological bands of TaAs when probed at large frequencies[66,67,144] makes it difficult to separate the contributions of trivial and topological bands to SHG. In RhSi the topological multifold crossings at Γ and R are separated in energy (~ 0.4 eV) and the topological bands are isolated from trivial bands. Our analysis of the optical conductivity of RhSi in Sec. 4.3 manifest

*When time-reversal symmetry is absent, both shift and injection currents can be nonzero for any light polarization.

the dominance of the threefold fermion in the linear response at low energies as a consequence of the energy separation between bands. The dominance of the threefold crossing at low energy and the isolation of the topological bands from trivial bands makes RhSi a promising material to study the effect of topological bands in the second-harmonic generation.

To interpret correctly the experimental results and understand the origin of the features observed in the second-harmonic response it is necessary to characterize the material, this is, have an accurate estimation of the scattering lifetime τ and the chemical potential in the sample. It is thus convenient to have an input independent from the second-harmonic experiment where we can estimate these quantities, and compare them against the results obtained for the linear optical conductivity in the previous chapter. To do so we will rely on the other second-order response described in this chapter: the CPGE. The particular form of the dependence of the CPGE reponse on τ makes it a suitable observable to obtain an estimation of the scattering lifetime τ from the experiment. Building up on our study of the optical conductivity of RhSi and the estimation of τ obtained from the CPGE experimental data we will study the SHG in RhSi.

5.2 The circular photogalvanic effect in RhSi

The CPGE has been the focus of recent studies that led to the prediction that this response would be quantized for chiral Weyl semimetals[62]. However, chiral Weyl semimetals with the required node separations to observe this quantization have not been synthesized as single crystals[†]. The two materials studied in this thesis, CoSi and RhSi, are good candidates to study the signatures of topological excitations in CPGE due to the energy separation between the nodes at Γ and R and the Lifshitz energy (see Fig. 4.1), of the order of 1 eV, in contrast with previous Dirac and Weyl semimetals, such as Cd_3As_2[149], Na_3Bi[150], TaAs[27,151] with Lifshitz energies < 100 meV.

[†]A promising candidate material to display a quantized CPGE was $SrSi_2$[145,146], but the first experimental works on $SrSi_2$ revealed that it is in fact a topologically trivial semiconductor[147,148].

In this section we will reproduce the results presented in Ref. [75], where we reported the experimental measurement of the CPGE response in RhSi and compared it with predictions based on DFT calculations and the tight-binding model for SG198 discussed in the previous chapters of this thesis. We will present the necessary background to understand the CPGE in RhSi. We focus on the material analysis that will tell us about the chemical potential and the hot-carrier lifetime in the sample, as we will use it as a reference to study the second-harmonic generation in the next section. Other details about the CPGE quantization in Weyl and multifold semimetals can be found in Refs. [62,96], and the details of the experiment presented in this section in Ref. [75].

In materials with time-reversal symmetry — like RhSi — the CPGE is directly determined by the injection current: when circularly-polarized light interacts with RhSi it induces a time-dependent current density, the injection current, given by[62,96,152]

$$\frac{dj_a}{dt} = \beta_{ab}(\omega)\left(\mathbf{E}(\omega)\times\mathbf{E}^*(\omega)\right)^b, \tag{5.1}$$

where $\mathbf{E}(\omega)$ is the electric field as described in Eq. 3.2, and $\beta_{ab}(\omega)$ is the CPGE tensor. This current grows linearly in time for times $t \ll \tau$, and the the CPGE response β_{ab} can be expressed as[75]

$$\beta_{ab}(\omega) = \frac{i\pi e^3}{4\hbar}\int_{BZ}\frac{d\mathbf{k}}{(2\pi)^3}\sum_{n>m} f_{nm}\epsilon^{bcd}\Delta^a_{nm}\mathrm{Im}\left(r^d_{nm}r^c_{mn}\right)\mathcal{L}_\tau\left(\epsilon_{nm}-\hbar\omega\right), \tag{5.2}$$

where $\Delta^a_{nm} \equiv \partial_{k_a}\omega_{mn}$, $r^a_{mn} = v_{nm}/(i\omega_{mn})$ (see Eq. 3.23), $f_{nm} = f_n - f_m$ is the difference of Fermi-Dirac distributions that accounts for the chemical potential and temperature, and $\mathcal{L}_\tau$ is a Lorentzian function that accounts for a finite hot-carrier scattering time τ in the sample.

5.2.1 Experimental features of the circular photogalvanic effect

In Fig. 5.1 we reproduce the experimental result presented in Ref. [75]. The CPGE response was obtained by THz emission spectroscopy.

The measurements were performed for circularly-polarized light with opposite helicities, and the CPGE contribution was extracted by taking the difference between the two emitted THZ pulses for incident photon energies between 0.2 and 1.1 eV.

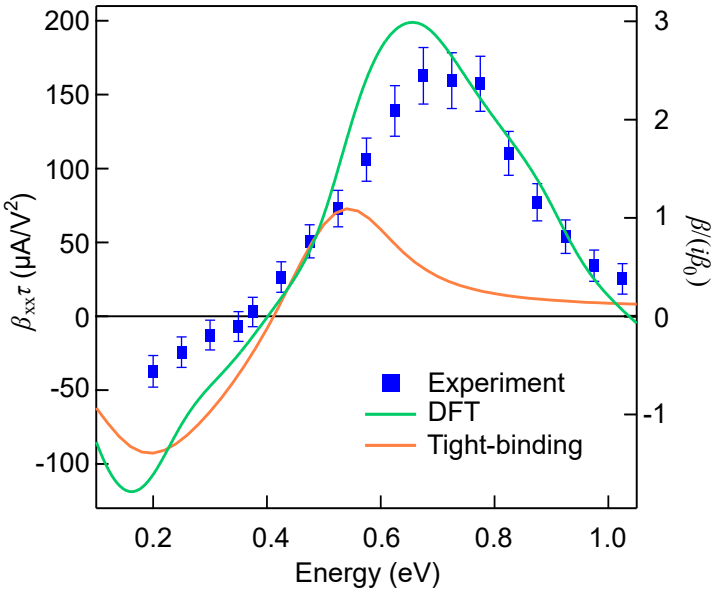

Figure 5.1: Experimental CPGE spectrum of RhSi (blue squares) compared to the DFT calculation for $\mu = -30$ meV and temperature $T = 300$ K (solid green line), and the tight-binding model (Eqs. 2.34–2.35) presented in Sec. 3.4.2 (solid orange line) for the parameters $v_1 = 1.95$, $v_p = 0.77$, and $v_2 = 0.4$. Both theoretical calculations are computed with a constant broadening $\eta = 100$ meV. Reproduced from Ref. [75].

In Fig. 5.1 we see that as the incident photon energy decreases from 1.1 to 0.7 eV, there is a rapid increase of the CPGE response with a peak value of 163(±19) μA/V^2 at 0.7 eV. Similar features were observed previously in Ref. [111]. As the incident photon energy decreases further from 0.7 to 0.2 eV, the CPGE response shows a sharp drop with a marked sign change at 0.4 eV. Noticeably, the peak response at 0.7 eV is one order of magnitude larger than a previous study on RhSi[111], probably due to a larger hot-carrier lifetime. Additionally, the sign change was absent in previous theory studies[96,103,104] and was not observed in previous experimental works since the lowest photon energies measured were around 0.5 eV[111]. Conversely, the quantized CPGE below 0.7 eV predicted in previous works[96,103,104] is absent in the experiment.

To extract the hot-carrier lifetime τ from this experimental data we rely on the tight-binding model for RhSi presented in Sec. 3.4.2 and a DFT calculation orignally presented in Ref. [75]. From the analysis performed in the previous chapter using the optical conductivity, we know that the hot-carrier lifetime τ in this sample is short compared to the pulse width used for the CPGE measurements[75]. Under these conditions, the total photocurrent is given by $\beta_{xx}\tau$[104]. As for the optical conductivity calculations, we assume the lifetime τ to be constant, and it is the only fitting parameter to match both the peak and width of the measured CPGE current with the theoretical predictions.

5.2.2 DFT calculation of circular photogalvanic effect in RhSi

In Fig. 5.1 we reproduce the results of the DFT calculation for $\mu = -30$ meV and $\eta = \hbar/\tau = 100$ meV ($\tau \approx 6.6$) fs . The DFT calculation captures quantitatively the features of the experimental CPGE data: the existence of a peak around 0.7 eV, its height and width, and the sign change of the response. This is consistent with the analysis of the optical conductivity in the previous chapter, and supports the estimation of the hot-carrier lifetime $\tau \approx 6.6$ fs and the conclusion that the chemical potential lies below the Γ node.

To understand how different regions in the Brillouin zone contribute to the CPGE, in Fig. 5.2 we show the momentum-resolved contribution to the CPGE response for different photon energies. Below 0.6 eV the main contributions come from the R and Γ points. The M point contributions are activated for energies higher than 0.75 eV. This indicates that the sign change observed at 0.4 eV is due to the activation of the excitations at the R point contributing to the CPGE with opposite sign with respect to Γ, which was also observed in a recent work studying a $k \cdot p$ model[113].

It is interesting to note that at 0.4 eV the R point is already active due to the large broadening $\eta \sim 100$ meV in this material. The differences observed between the theoretical calculation and the experimental measurements suggest that considering a constant, energy-independent hot-carrier scattering time τ might be

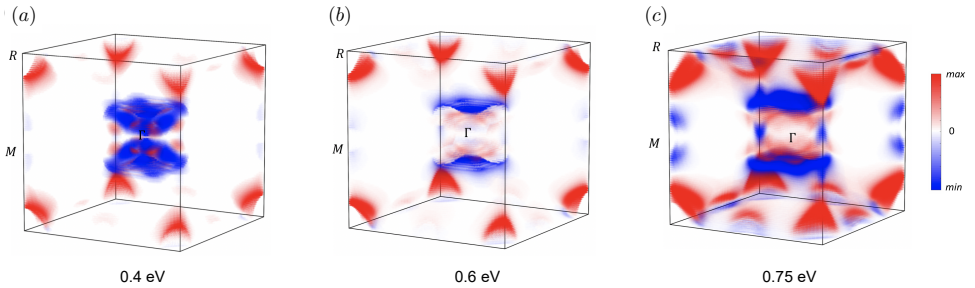

Figure 5.2: CPGE contributions from different regions in the Brillouin zone. Momentum-resolved contribution to the CPGE photocurrent shown in Fig. 5.1 (solid green line) for incident photon energies 0.4 (a), 0.6 eV (b), and 0.75 eV (c). The contribution is indicated in the red-blue color scale, where red indicates a positive contribution and blue a negative contribution. Adapted from Ref. [75].

an oversimplified phenomenological model for the disorder. Including energy and momentum dependence in the hot-carrier scattering time might give an even better agreement between theory and experiment. However, to the best of our knowledge, no work has studied the energy and momentum dependence of τ for RhSi so far.

5.2.3 Circular photogalvanic effect calculation with a tight-binding model for RhSi

As discussed in the previous chapters, the tight-binding model for SG198 presented in Sec. 3.4.2 is the simplest model to capture the multifold fermions at Γ and R points. It is illustrative to compare the results obtained for the tight-binding model with the DFT results described in this section. In Fig. 5.1 (a) we reproduce the results for the CPGE using the tight-binding model for SG198[‡ 75] with parameters $\eta = 100$ meV and $\mu = -100$ meV, obtained in the analysis of the optical conductivity in the previous chapter. This calculation underestimates the position of the peak and the overall magnitude of the CPGE. This discrepancy can be attributed to the failure of the tight-binding model to capture the M point, as was extensively discussed in Sec. 4.2.1. It shows, however, the overall peak-dip structure of the response and the sign change around 0.4 eV, consistent with the chemical potential placed under the threefold

[‡]The tight-binding parameters are those obtained in Chapter 4 for the optical conductivity calculation: $v_1 = 1.95$, $v_p = 0.77$, and $v_2 = 0.4$.

node at Γ. This manifests the crucial relevance of the curvature of the flat band at the Γ point and the important contributions of the saddle point at M, missing in the tight-binding model.

The comparsion between experimental data and theory indicate that the chemical potential is placed below the node at Γ in RhSi, with values between -30 and -100 meV, and agree well for hot-carrier lifetime $\tau \sim 6.6$ fs, equivalent to a broadening of $\eta \sim 100$ meV. This is consistent with the results obtained analyzing the optical conductivity of RhSi (Sec. 4.3), giving us a solid estimation of the position of the Fermi level and the hot-carrier scattering lifetime that we will use to compute the SHG of RhSi in the next section.

5.3 Second-harmonic generation in RhSi

After studying the CPGE and the optical conductivity, we have a good estimation of the position of the Fermi level and the hot-carrier scattering lifetime. This is crucial to obtain an accurate prediction for the SHG in RhSi and to correctly interpret the experimental results, and to attribute the origin of the SHG features to material properties implemented in the theoretical models.

To study the SHG in RhSi we will compute the second-harmonic response using a low-energy $k \cdot p$ model describing the threefold crossing at the Γ point and a DFT calculation in a wider energy range with a large number of bands. We will discuss the results of the theoretical calculations in comparison with the experimental data, originally reported in Ref. [76].

5.3.1 Second-harmonic generation in the length gauge

To compute the second-harmonic generation for both the low-energy $k \cdot p$ model and the DFT, our first task is to write the expression for the second-harmonic response. In Sec. 3.1 we discussed how we can express the current induced in a material by a light source as a series

on increasing powers of the eletric field (see Eq. 3.21). At second order, we can express the contribution to the induced current as

$$J_a^{(2)}(t) = \sigma_{abc}^{(2)}(\omega_1, \omega_2)\, E_{\omega_1}^b E_{\omega_2}^c e^{-i(\omega_1+\omega_2)t}. \tag{5.3}$$

Since we are considering a monochromatic light source, the only possible combinations are $\omega_1 = -\omega_2$ and $\omega_1 = \omega_2$. In the first scenario we find $\omega_1 + \omega_2 = 0$, a DC response that we already studied in the CPGE section. In the second scenario, the system will show a response at $\omega_1 + \omega_2 = 2\omega$, which we refer to as second-harmonic response and label as $\sigma^{abc}(2\omega; \omega, \omega) \equiv \sigma_{abc}^{(2)}(\omega, \omega)$.

In Eq. 3.24 we showed how the responses in the perturbative expansion (Eq. 3.21) are related to the density matrix order by order. The solution to the density matrix equation is iterative, and we can use the first-order solution of the density matrix in Eq. 3.20 to compute the second-order response $\sigma^{abc}(2\omega; \omega, \omega)$.

For later convenience we will work with the second-order susceptibility $\chi^{abc}(2\omega; \omega, \omega)$, which is related to the second-order conductivity $\sigma^{abc}(2\omega; \omega, \omega)$ by $\sigma^{abc}(2\omega; \omega, \omega) = -i2\omega\chi^{abc}(2\omega; \omega, \omega)$. We can separate the second-harmonic response into terms involving one photon and two photons as[153]

$$\chi^{abc}(2\omega; \omega, \omega) = \chi_{\text{2ph}}^{abc}(\omega) + \chi_{\text{1ph}}^{abc}(\omega), \tag{5.4}$$

where the labels 2ph and 1ph denote two- and one-photon transitions, respectively, $\chi_{\text{2ph}}^{abc} = \chi_{\text{2ph,inter}}^{abc} + \chi_{\text{2ph,intra}}^{abc}$, and $\chi_{\text{1ph}}^{abc} = \chi_{\text{1ph,inter}}^{abc} + \chi_{\text{1ph,intra}}^{abc} + \Sigma^{abc}$. The above terms of $\chi^{abc}(2\omega; \omega, \omega)$ are

$$\chi_{\text{2ph,inter}}^{abc}(\omega) = C \int_k \sum_{nml} \frac{r_{nm}^a \{r_{ml}^b r_{ln}^c\}}{(\omega_{ln} - \omega_{ml})} \frac{2f_{nm}}{(\omega_{mn} - 2\omega)}, \tag{5.5}$$

$$\chi_{\text{1ph,inter}}^{abc}(\omega) = C \int_k \sum_{nml} \frac{r_{nm}^a \{r_{ml}^b r_{ln}^c\}}{(\omega_{ln} - \omega_{ml})} \left[\frac{f_{ml}}{\omega_{ml} - \omega} + \frac{f_{ln}}{\omega_{ln} - \omega}\right], \tag{5.6}$$

$$\chi^{abc}_{\text{2ph,intra}}(\omega) = C\int_k \sum_{nm} \frac{r^a_{nm}\{\Delta^b_{mn} r^c_{mn}\}}{\omega^2_{mn}} \frac{-8i f_{nm}}{(\omega_{mn}-2\omega)} + C\int_k \sum_{nml} \frac{r^a_{nm}\{r^b_{ml} r^c_{ln}\}}{\omega^2_{mn}} \frac{2f_{nm}(\omega_{ml}-\omega_{ln})}{(\omega_{mn}-2\omega)}, \tag{5.7}$$

$$\chi^{abc}_{\text{1ph,intra}}(\omega) = C\int_k \sum_{nml} r^a_{nm}\{r^b_{ml} r^c_{ln}\} \frac{\omega_{mn} f_{nl}}{\omega^2_{ln}(\omega_{ln}-\omega)} - C\int_k \sum_{nml} r^a_{nm}\{r^b_{ml} r^c_{ln}\} \frac{\omega_{mn} f_{ml}}{\omega^2_{ml}(\omega_{ml}-\omega)}, \tag{5.8}$$

$$\Sigma^{abc}(\omega) = \frac{iC}{2}\int_k \sum_{nml} \omega_{nl} r^a_{lm}\{r^b_{mn} r^c_{nl}\} \frac{f_{nm}}{\omega^2_{mn}(\omega_{mn}-\omega)} - \frac{iC}{2}\int_k \sum_{nml} \omega_{lm} r^a_{nl}\{r^b_{lm} r^c_{mn}\} \frac{f_{nm}}{\omega^2_{mn}(\omega_{mn}-\omega)} + \frac{iC}{2}\int_k \sum_{nm} \frac{f_{nm}\Delta^a_{nm}\{r^b_{mn} r^c_{nm}\}}{\omega^2_{mn}(\omega_{mn}-\omega)}, \tag{5.9}$$

where $C = e^3/\hbar^2$, the wave vector k is defined in the Brillouin zone, $\int_k = \int \mathrm{d}^3k/(4\pi^3)$, lmn subscripts denote band indices, the energy of band n is $\hbar\omega_n$, and the frequency difference is $\omega_{mn} = \omega_m - \omega_n$. We recall that $r^a_{mn} = iv^a_{nm}/\omega_{mn}$, and $\Delta^a_{mn} = \partial_{k_a}\omega_{mn} = v^a_{mm} - v^a_{nn}$, where v^a_{nm} denotes the velocity matrix elements (see Eq. 3.23). The curly brackets impose symmetrization with respect to the Cartesian coordinates such that $\{A^a_{ml}B^b_{ln}\} = \frac{1}{2}(A^a_{ml}B^b_{ln} + B^a_{ml}A^b_{ln})$.

5.3.2 Second-harmonic generation of the threefold fermion at Γ: low-energy $k \cdot p$ model

As a first step in understanding the second-harmonic response of RhSi we will focus on the threefold fermion at the Γ point. In the analysis of the optical conductivity of RhSi (Sec. 4.3) we observed that the curvature of the middle band of the threefold fermion plays an important role in the behaviour of the optical transitions near the Γ point. Since the threefold model presented in Eq. 2.15 has only linear terms in momentum $\mathbf{k}$, it cannot capture the curvature of the middle band. Thus, in this section we use the three-band $k\cdot p$ model with up-to-second order

terms in momentum, originally presented in Ref. [113] for CoSi, which, as we know, crystallizes in the same space group as RhSi.

The $k{\cdot}p$ Hamiltonian is built based on the point group T at the Γ point of SG198. To build this model we consider first a higher-symmetry point group, O, and we add the necessary terms to break down the symmetry to T. Thus, we can express the $k \cdot p$ Hamiltonian as $H_{3f}^{k^2} = H_O + H_T$. The first term

$$H_O = \begin{pmatrix} ak^2 + \frac{2c}{3}(k^2 - 3k_z^2) & ivk_x + bk_yk_z & -ivk_y + bk_xk_z \\ -ivk_x + bk_yk_z & ak^2 + \frac{2c}{3}(k^2 - 3k_y^2) & ivk_z + bk_xk_y \\ ivk_y + bk_xk_z & -ivk_z + bk_xk_y & ak^2 + \frac{2c}{3}(k^2 - 3k_x^2) \end{pmatrix}, \tag{5.10}$$

is the most general Hamiltonian allowed by the point group symmetry O. Here $k = \sqrt{k_x^2 + k_y^2 + k_z^2}$, and a, v_F, b, and c are the parameters corresponding to the terms coming from A_1, T_1, T_2, and E symmetries, respectively.

The second contribution, which breaks down the symmetry to the point group T, is written as

$$H_T = \frac{2d}{\sqrt{3}} \begin{pmatrix} k_y^2 - k_x^2 & 0 & 0 \\ 0 & k_x^2 - k_z^2 & 0 \\ 0 & 0 & k_z^2 - k_y^2 \end{pmatrix}. \tag{5.11}$$

Together, they form the most general symmetry-allowed Hamiltonian $H_{3f}^{k^2} = H_O + H_T$ up to second order in momentum for the threefold degeneracy at the Γ point.

In previous calculations using this model[113] the effect of the parameter d proved to be negligible in other optical responses like the circular photo-galvanic effect. Nevertheless, to study the second-harmonic response it is crucial to include the symmetry breaking term with a finite d parameter since the SHG response is forbidden for the point group O, but generically finite for the point group T[113,154].

The eigenvectors and eigenvalues of the $k \cdot p$ model do not depend on d up to second order in $\mathbf{k}$[113,154], and thus we cannot use their analytical expressions to fit the value of d. To obtain the low-energy model parameters, we fit the the $k \cdot p$ parameters by fitting the $k \cdot p$ model to the tight-binding model for RhSi described in Sec. 4.3. The resulting values for the parameters are $(a, b, c, d, v_F) = (-0.0438344, -0.01, 0.131377, 0.1874, 0.385)$. This choice of parameters sets the threefold node at $E = 0$ eV. As we saw in the previous chapters, the chemical potential, and thus the position of the Fermi level E_f, plays a crucial role in the optical responses of RhSi. To test the different values of E_f we add a term to the Hamiltonian $H = H_{3f}^{k^2} - E_{f3\times3}$.

To account for the broadening induced by the finite scattering in the sample we consider a constant broadening η by replacing $\omega \to \omega + i\eta$ in Eq. 5.4 in a similar fashion to the optical conductivity and CPGE calculations. This increases considerably the computational cost of the second-harmonic response calculation. To obtain results in reasonable time scales we wrote a parallelized code in Julia[155]. More information about the code can be found in Appendix E.

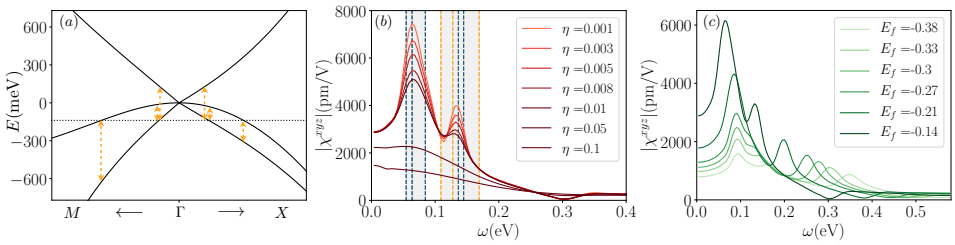

Figure 5.3: Second-harmonic generation of the $k \cdot p$ model for the threefold fermion at the Γ point of RhSi. (a) Band structure of the $k \cdot p$ model along the $\Gamma \to X$ and $\Gamma \to M$ directions with parameters $(a, b, c, d, v_F) = (-0.0438344, -0.01, 0.131377, 0.1874, 0.385)$. The threefold node is placed at $E_\Gamma = 0$ eV, and the Fermi level is placed at $E_f = -0.14$ eV. The vertical dashed arrows indicate the most relevant one-photon activation energies. (b) Nonlinear susceptibility (solid lines) of the $k \cdot p$ model shown in (a) for different values of disorder η. The energy regions where the most relevant transitions are activated are indicated in shaded grey. The vertical dashed lines indicate the two-photon activation frequencies (blue) and the one-photon activation frequencies (ocher). (c) Nonlinear susceptibility for different values of E_f shown in different shades of green with a disorder $\eta = 0.005$ eV.

In Fig. 5.3 we show the second-harmonic response of the $k \cdot p$ model. As we see in Fig. 5.3 (b) the response features a two-peak structure at

low energies. The energy regions where these peaks appear are delimited by the activation frequencies of the transitions from the lowest to the middle band and from the lowest to the upper band. The first peak is dominated by the two-photon transitions from the lowest to the middle band (see Fig. 5.3 (b), vertical dashed blue lines and shaded grey region). The lower, second peak in Fig. 5.3 (b) appears in the energy region (shaded gray) delimited by one-photon transitions from the lower to the middle band (vertical ocher lines) and the two-photon transitions from the middle to the upper band (vertical blue lines).

As the disorder broadening η is increased, the features of the nonlinear response are broadened, and the two-peak structure is no longer distinguishable at $\eta = 0.05$ eV (Fig. 5.3 (b)) for $E_f = 0.14$ eV. For higher η, the nonlinear response features a single, wider and smoother peak, with contributions from one- and two-photon optical tranistions.

The activation frequencies, and thus the position and width of the peaks, depend on the Fermi level. As the threefold node at Γ is separated from the Fermi level, the activation frequencies and the difference between them becomes larger. As a result, the peak positions are shifted towards higher energies. The peaks also become wider because the energy regions delimited by the activation frequencies are spread over a larger range of energies (see Fig. 5.3 (c)). For large values of E_f the one-photon transitions are suppressed due to the Pauli blocking at low energies, and the two-photon response becomes dominant.

Of course, this model is limited to a small energy range. This model is useful to understand the behaviour of the second-harmonic response coming from the optical transitions near the threefold crossing under different values of disorder and chemical potential. Nevertheless, we know that in RhSi the energy separation between the threefold node at Γ and the double-Weyl at R is around 0.4 eV. Since we are considering two-photon processes, a two-photon excitation with photons of energy $\omega \sim 0.2$ eV could explore the excitations coming from the R point. Thus, the energy range in which the $k \cdot p$ model is suitable for potentially describing the experiment is very limited compared to the linear optical conductivity. This type of two-photon process also leads to a smaller energy scope of the tight-binding model used previously for RhSi, which we would expect to be reduced from a good agreement up to ~ 0.5 eV in the optical conductivity (Fig. 4.9) to less than 0.25 eV in the SHG.

5.3.3 Experimental features of the second-harmonic generation in RhSi: characterization with DFT calculations

The limitations expected for the $k \cdot p$ and tight-binding models lead naturally to the need for a DFT calculation capable of describing multiple bands above and below the Fermi level, providing a large energy range where the theoretical prediction is suitable for describing the experimental results.

In Fig. 5.4 we reproduce the experimental and DFT results originally reported in Ref. [76] for the second-harmonic susceptibility of RhSi in the energy range $0.27-1.5$ eV. To understand the SHG features observed in the experiment we compare the results with a DFT calculation performed using the EXCITING package[156]. In this calculation the lattice parameters of RhSi were chosen based on previous experimental measurements[103,157], and the computations were performed using a $40 \times 40 \times 40$ **k**-mesh. As band splitting due to the spin-orbit coupling is of the order of meV[103] — much smaller than the estimated scattering strength $\eta \sim 100$ meV[75,111] (see Sec. 4.3) — and including SOC is computationally expensive, this effect is neglected in the DFT calculation.

In Fig. 5.5 we show the electronic band structure for RhSi. This DFT calculation considers a larger number of bands and higher energies than the previous DFT calculation used in this thesis for the optical conductivity (see Sec. 4.3). For the pristine system with Fermi energy $E_f = 0$ the threefold node is located slightly above the Fermi level, and the double-Weyl node at R is located around 0.4 eV below the Fermi level, consistent with the analysis of the optical conductivity of RhSi in Sec. 4.3. Since the DFT considers multiple bands, we see that degenerate threefold crossings also exist at different energies at the Γ point, e.g., around $E \approx -1.57$ eV, a region magnified in Fig. 5.5 (c).

In Fig. 5.4 we reproduce the results for the SHG of RhSi using the DFT calculations. In order to compare the theoretical prediction with the experiment, the SHG response is calibrated with that of GaAs[142] in a similar fashion to the procedure followed in the experiment[76].

To account for the effects of disorder and finite temperature the

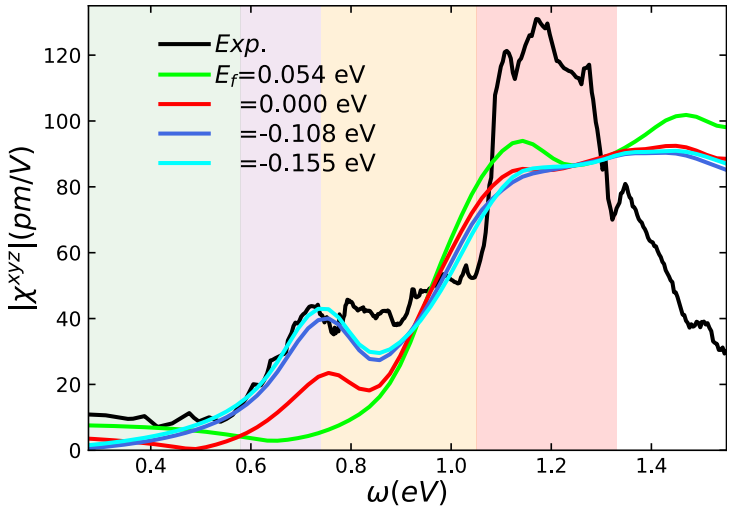

Figure 5.4: Experimental SHG response of RhSi compared to the DFT calculation. Experimentally measured (black line) and theoretically calculated (colored lines) SHG susceptibilities. Fermi energies are indicated by colors $E_f = 0.054$ (green), 0.00 (dark red), -0.108 (royal blue), -0.155 (cyan) eV. The scissors potential is $\Delta = 1.23$ eV. Shaded areas represent the photon energies at which different transitions from the valance to conduction bands occur. See also Fig. 5.5 (a) for examples of these transitions. Shaded areas span $\omega \in [0.276, 0.58]$ (green), $[0.58, 0.74]$ (purple), $[0.74, 1.05]$ (orange), and $[1.05, 1.33]$ (red) eV. Reproduced from Ref. [76].

calculation includes a constant broadening $\eta = 100$ meV obtained from the analysis of the optical conductivity and CPGE experiments in Sec. 4.3 and Sec. 5.2, respectively. The DFT calculation includes a scissors shift[153] of $\Delta = 1.23$ eV to account for inaccurate energy differences between the occupied and unoccupied bands. This correction modifies the energy differences between bands ω_{mn}, modifying the activation frequencies of the optical transitions. To see how this correction is implemented see Appendix F.

The SHG yield for RhSi (Fig. 5.4) is computed for one Fermi energy that lies above the threefold node ($E_f = 0.054$, green line), and three that lie below this node ($0.0, -0.108, -0.155$ eV). We see that for $\omega \lesssim 0.45$ eV, theory and experiment agree better when $E_f = 0.054$ eV, while for $\omega > 0.45$ eV, it is the $E_f = -0.108, -0.155$ eV (cyan and royal blue lines) curves that better reproduce the experimental data.

The small SHG yield in the green frequency window $\omega \in [0.276, 0.58]$ in Fig. 5.4 (c) is a result of the suppressed optical transitions between

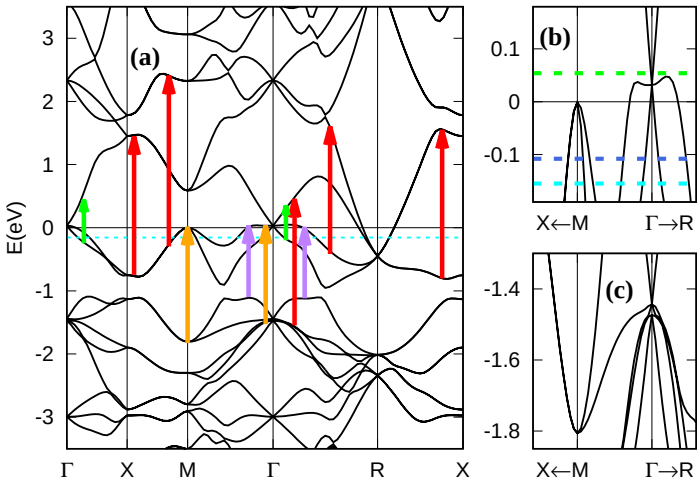

Figure 5.5: DFT band structure of RhSi and optical transitions. (a) First-principles band structure of RhSi without spin-orbit coupling. Arrows indicate representative two-photon electronic transitions in SHG, and their color code corresponds to that of the shaded areas representing different frequency windows in Fig. 5.4 (c). (b) Zoom to the low-energy bands between Γ and M points close to the Fermi level. Dashed lines indicate the Fermi energies at which the theoretical curves in Fig. 5.4 (c) are plotted, namely $E_f = 0.054$ (green), -0.108 (royal blue), and -0.155 (cyan) eV. (c) Same as (b) but close to energy -1.6 eV. The zero of energy scale represents the Fermi energy of the pristine system. Reproduced from Ref. [76].

low-energy linearly dispersing bands close to the Γ point (see green arrows in Fig. 5.5). To support this conclusion in Fig. 5.6 we show separate one-photon (ω) and two-photon (2ω) transitions contributing to χ^{xyz}. We observe that two-photon transitions dominate the green frequency region, regardless of whether the threefold Γ node is occupied ($E_f = 0.054$ eV) or unoccupied ($E_f = -0.155$ eV). Next, we compare this result to the two-photon and one-photon JDOS (see Eq. 4.1) in Fig. 5.7 (a) and (b), respectively. In the green frequency window, the one-photon JDOS dominates, compared to the two-photon JDOS (see Fig. 5.7 (a)–(b)). Comparing with Fig. 5.6, this indicates that the optical matrix elements suppress the one-photon contribution to χ^{xyz}, reducing the overall SHG for $\omega < 0.58$ eV. The band structure in Fig. 5.5 suggests that the contribution to one-photon processes in this frequency region arises from linear bands around Γ, whose matrix elements therefore do not contribute strongly to the SHG.

We move on to analyze the purple frequency window in Fig. 5.4 (c),

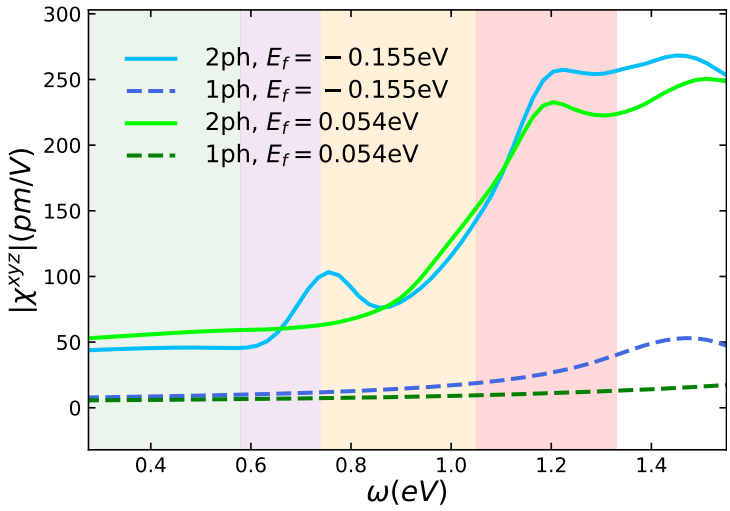

Figure 5.6: Calculated different components of SHG from two-photon (solid sky blue line) and one-photon (dashed royal blue line) transitions with Fermi energy $E_f = -0.155$ eV, as well as two-photon (solid green line) and one-photon (dashed dark green line) transitions with Fermi energy $E_f = 0.054$ eV and scissors potential $\Delta = 1.23$eV. The total SHG susceptibility is plotted in Fig. 5.4 (c). Reproduced from Ref. [76].

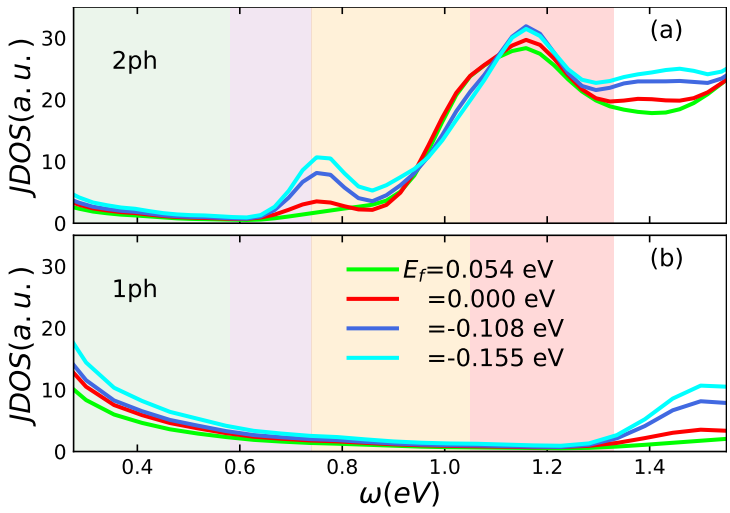

Figure 5.7: Optical JDOS for SHG from two-photon (a) and one-photon (b) contributions. The parameters and colors are the same as Fig. 5.4. Reproduced from Ref. [76].

i.e., $\omega \in [0.58, 0.74]$ eV. The SHG increases in this region, a feature which is captured in the DFT calculation only if $E_f < 0$ eV. Separately plotting one- and two-photon contributions as before in Fig. 5.6 reveals that the two-photon response in the purple energy window is dominant. Consistent with our discussion in the previous paragraph, the rise of the two-photon contributions occurs around $\omega \approx \Delta/2$ in the JDOS. When compared to the band structure, the observation of a dominant two-photon transition in Fig. 5.6 suggests that two partially flat bands close to the Γ point, separated by approximately 1.3 eV, and connected by two-photon excitations (purple arrows in Fig. 5.5), are responsible for enhancing χ^{xyz} in the purple energy window. The width of this energy window is comparable to the broadening $\eta = 0.1$ eV, supporting their flat band origin.

At photon energies $\omega \in [0.74, 1.05]$ eV, *i.e.*, in the orange window in Fig. 5.4 (c), the data exhibits a plateau-like structure. The DFT calculations show that this feature is reproduced better for $E_f = -0.108, -0.155$ eV. Naively, one would expect that in this frequency window the one-photon electronic transitions from linear bands close to the R point are activated. However, Figs. 5.6 and 5.7 reveal that the one-photon contribution (dashed lines) is small compared to the dominant two-photon transitions. The small contribution of the linearly dispersing bands close to the R point is expected by dimensional analysis and confirmed by the DFT results. The two-photon transitions responsible for SHG in this region likely involve dispersing valance bands around the M and Γ points, as indicated by the orange arrows in Fig. 5.5.

Lastly, there is a drastic increase of χ^{xyz} measured within the red energy window of $\omega \in [1.05, 1.33]$ eV in Fig. 5.4 (c). The DFT results also report an increased SHG yield in this energy range. Once more we can identify the substantial role of two-photon transitions compared to the smaller one-photon contribution (see Figs. 5.6 and 5.7). The large photon energies that define this energy window enable electrons to reach a considerable number of bands exemplified by red arrows in Fig. 5.5. As frequency increases, we observe quantitative differences between the DFT results and the experimental measurements, especially when $\omega > 1.33$ eV. These deviations could be attributed to the insufficient many-body corrections in the first-principle calculations.

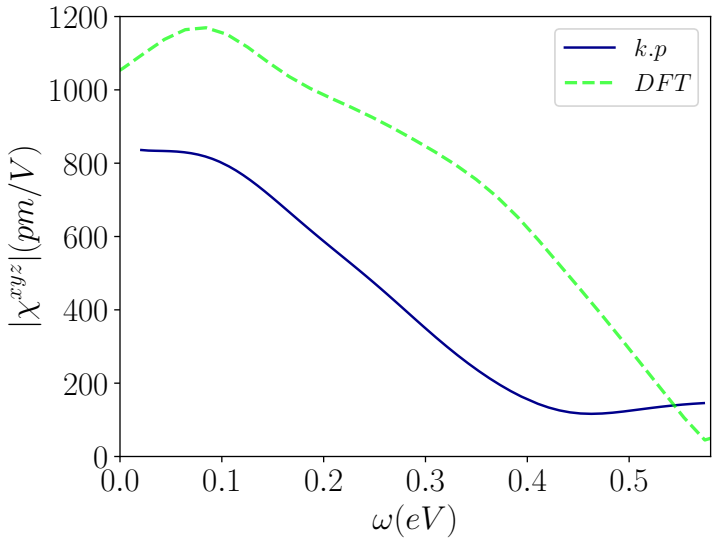

Figure 5.8: Comparison between the second-harmonic response obtained for the $k \cdot p$ model (blue line) at $E_f = -0.27$ eV and DFT calculations (dashed green line) at $E_f = -0.14$ eV. Both curves are calculated with $\Delta = 0$ eV and $\eta = 0.1$ eV. Reproduced from Ref. [76].

5.4 Comparing low-energy second-harmonic generation using first-principles and $k \cdot p$ calculations

The analysis of the SHG presented in the previous section is based on DFT calculations with a large scissors potential $\Delta = 1.23$ eV. To compare the SHG obtained from DFT (Sec. 5.3.3) with the SHG obtained from the $k \cdot p$ (Sec. 5.3.2), in Fig. 5.8 we show the nonlinear susceptibility of RhSi obtained for $E_f = -0.14$ eV using DFT and $E_f = -0.27$ eV using the $k \cdot p$ model. Both $k \cdot p$ and DFT are computed without many-body effects, *i.e.*, $\Delta = 0$ eV, and are calibrated with the SHG response of GaAs in a similar fashion to the procedure in the experiment[76].

Fig. 5.8 shows that the second-harmonic generation obtained from DFT and the $k \cdot p$ calculations without the scissors potential correction are similar. The broader peak in DFT compared to that of the $k \cdot p$ model can be attributed to extra electronic transitions in DFT, which are not captured by the $k \cdot p$ model.

We illustrate the influence of the scissors potential Δ on shifting the absorption energy in the nonlinear response χ^{xyz} in Fig. 5.9. The results are calculated for the pristine RhSi system ($E_f = 0$) and originally presented in Ref. [76]. The figure shows that by adjusting Δ, the energy difference between bands ω_{mn} is modified, and thus the optical transitions between bands. As we increase the value of the scissors potential Δ, the activation frequencies move to higher energies and the peak present at low energies in the DFT calculation dissapears. The shift to higher energies of the activation frequencies suppresses the one- and two-photon transitions between the topological bands of the threefold fermion at Γ point and leads to a better description of the experimental SHG data in RhSi (Fig. 5.4).

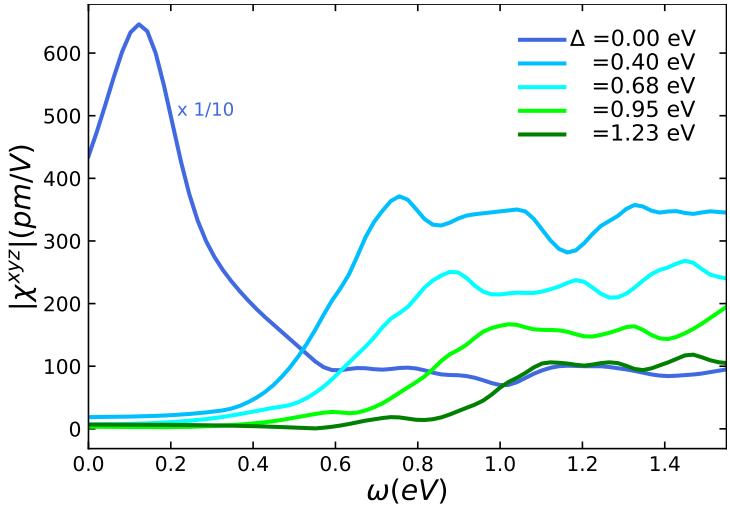

Figure 5.9: Different scissors corrections for the second-harmonic susceptibility χ in pristine RhSi ($E_f = 0$) with a disorder broadening of $\eta = 0.1$ eV. Reproduced from Ref. [76].

5.5 Conclusions

The first-principles calculations with a scissors potential $\Delta = 1.23$ eV agree with the experimental data of SHG in RhSi, both presented in Ref. [76]. However, the DFT results only match the SHG of the $k \cdot p$ model of the threefold fermion at Γ when no scissors potential is included. In this regime ($\Delta = 0$), both calculations show a strong peak in the SHG at the frequencies of the one- and two-photon optical transitions near the Γ point. However, the behavior of the DFT results of the SHG of RhSi are different from that observed experimentally.

The DFT results with $\Delta = 1.23$ show that one-photon transitions among relatively linear bands have a small contribution to SHG. Instead, two-photon transitions, including those between relatively flat bands, account for the observed SHG signal. This can be explained by the scissors potential, which separates occupied and unoccupied states and favours two-photon over one-photon transitions.

Unfortunately, there are no experimental data of the SHG of RhSi at low energies, where the $k \cdot p$ calculations and DFT calculations with $\Delta = 0$ predict a large response due to the topological bands. The current understanding of the SHG in RhSi is based on the agreement between the experimental results in the range $0.3-1$ eV and the DFT results with a large scissors potential. The scissors correction is a coarse, relatively uncontrolled approximation that works better for high energies than for low energies[76].

To shed light on the effect of optical transitions between topological bands of RhSi near the Γ point it would be helpful to perform more precise DFT calculations that can describe the low- and intermediate-energy regime ranging from 0 to 1 eV.

6

Conclusions

Since the initial predictions for the existence of Weyl fermions in condensed matter[20,21,24,25], many different experimental techniques have confirmed the existence of various Weyl semimetals[26–30,32–42]. Among these techniques, optical responses have shown a fruitful variety of effects associated with the existence of Weyl fermions, such as the linear frequency dependence of the optical conductivity[24,55–57] and the quantized circular photogalvanic effect[62] (CPGE). Additionally, the Weyl semimetal TaAs has shown the largest second-harmonic generation (SHG) measured in a material[68,158], although its relation with the existence of Weyl fermions is still unclear.

In 2016, Bradlyn *et al*[70] predicted the existence of a new type of fermion in chiral crystals, the chiral multifold fermions, protected by crystal symmetries. The threefold and fourfold multifold fermions can be thought of as a generalization of the Weyl fermion in the sense that they are described by a generalized Weyl equation with higher spin. However, unlike Weyl fermions, threefold and fourfold fermions do not have a counterpart in the traditional classification of fermions as free particles. In this thesis we have studied the optical properties of chiral multifold fermions using low-energy models and realistic tight-binding models in combination with experimental data.

In this chapter, we will give a brief overview of the main results since we already provided a detailed discussion of the results obtained in each chapter. Then, based on these results, we discuss possible avenues to fill the gaps in our current understanding of chiral multifold semimetals and a personal perspective of future research in these materials and potential applications of the optical responses in topological systems.

In Chapter 1, we provided an overview of the experimental characterization of Weyl semimetals. After this, we introduced the concept of multifold fermion as a generalization of Weyl fermion and

motivated our aim to study the optical responses of these new types of quasiparticles in real materials.

In Chapter 2, we provided a detailed classification of all chiral multifold fermions, emphasizing their topological properties and the different points in every space group (SG) where they can appear. In this chapter, we introduced the two types of models that we used throughout the thesis in increasing order of complexity: $k \cdot p$ models and tight-binding models.

In Chapter 3, we derived the general expression for the optical conductivity in the length gauge, setting the notation for our calculations of optical responses. Next, we computed the optical conductivity of *all* chiral multifold fermions. We established the optical selection rules in the symmetric cases and provided quantitative results about how these selection rules are gradually violated as the $k \cdot p$ Hamiltonians depart from the completely symmetric cases. We found that the activation frequencies are unique for each type of multifold fermion given the same chemical potential, leading to a slope change in the optical conductivity at different energies for each case. Additionally, we found that the optical conductivity of threefold and fourfold fermions are up to four times larger than that of a Weyl fermion per node, given the same Fermi velocity. Finally, we computed the optical conductivity of the tight-binding models describing the crystal symmetries of space groups 198 and 199. We identified the signatures of the multifold fermions present in each band structure, providing a quantitative explanation of the contribution of each type of multifold fermion in the band structure to the total optical conductivity.

In Chapter 4, we built on the theoretical results of the previous chapters and studied two materials candidates to host multifold fermions: RhSi and CoSi. The analysis of the experimental results with different models allowed us to trace back the features observed in the experimental optical conductivity to the existence of multifold fermions near the Fermi level and estimate the chemical potential and the scattering lifetime in both materials. We discussed extensively the crucial role of the position of the Fermi level with respect to the partially flat band of the threefold fermion at the Γ point and the importance of the transitions near the M point. By studying the joint density of states (JDOS) in the case of CoSi, we saw that the M point is a saddle point,

and the tight-binding model for SG198 does not correctly capture its contribution. This exhaustive analysis allowed us to set clear limits for the range of applicability of the tight-binding model: it cannot capture the flat region of the central band of the threefold fermion at the Γ point and is valid for energies smaller than the activation frequencies of optical transitions near the M point.

Additionally, in RhSi the disorder scale is similar to the spin-orbit splitting, washing out any spin-orbit-related features and allowing us to rely on the spinless models for its analysis. This material has a larger overall energy scale than CoSi, which leads to a better description of the optical conductivity by the spinless tight-binding model up to ~ 0.6 eV. However, in CoSi we found that the disorder scale is small enough to reveal spin-orbit splitting effects in this material compatible with the existence of a spin-3/2 fourfold fermion at the Γ point.

In Chapter 5, we introduced nonlinear responses in topological semimetals, focusing on the second-order monochromatic responses: the circular photogalvanic effect (CPGE) and second-harmonic generation (SHG). We analyzed the CPGE experiment in RhSi presented in Ref. [75] to estimate the scattering lifetime and the position of the chemical potential. The results obtained for the CPGE are consistent with those obtained from the analysis of the optical conductivity of RhSi, reinforcing the conclusion that the Fermi level lies under the threefold node at Γ and that this material has a large disorder scale of ~ 100 meV. Furthermore, the density functional theory (DFT) analysis of the contributions of different regions in the Brillouin zone confirmed the crucial relevance of the M point, in this case, for the CPGE. Armed with all the previous results obtained in this thesis, we studied the second-harmonic generation of RhSi. To do so, we implemented a parallelized code in Julia[155] language capable of computing the SHG for several values of disorder and chemical potential in a single run, separating the one- and two-photon contributions.

Due to the limited applicability of the tight-binding model used in Chap. 4 when exploring two-photon optical transitions, we relied on a three-band second-order $k \cdot p$ model describing the threefold fermion at the Γ point. The large energy difference between the threefold fermion at the Γ point and the double-Weyl fermion at the R point results in a relatively large energy window where the only relevant contributions

come from transitions near the Γ point. The SHG of the $k \cdot p$ model shows two large peaks in the low-energy regime due to the activation of the one- and two-photon optical transitions between topological bands of the threefold crossing. However, the low-energy range where this behavior is displayed is extremely challenging to access with the current experimental techniques. To analyze the experimental results in a range of energies between 0.3 eV and 1.5 eV, we relied on DFT calculations. Within the scissors approximation, the DFT calculations reproduced the reported experimental data reasonably well up to ~ 1.1 eV, tracing back the features observed in the SHG to different transitions between multiple bands across the Brillouin zone. We observed that in RhSi, the experimental data does not show an enhanced second-harmonic response due to the linear topological bands at the R point, but instead, it features a significant increase due to transitions between partially flat bands.

It is important to note that to reproduce the SHG experimental data adequately, the DFT calculations include a sizable scissors potential of 1.23 eV. The scissors approximation is a coarse approximation that shifts the energy difference between occupied and unoccupied bands independently of their energy or other properties. Thus, we do not know what is the underlying physical reason that makes necessary this large correction of the energy differences between bands to adequately describe the experimental results. This open question highlights the importance of new research to understand the effects of interactions and strong disorder in chiral multifold semimetals. A recent work[159] established that interaction effects spoil the quantization of the CPGE in Weyl semimetals. Additionally, another work[160] calculated that interaction effects in CoSi can be relevant, affecting the lifetime of multifold quasiparticles. Following this line, it would be interesting to study the effect of interactions in threefold and fourfold fermions and estimate how relevant they can be in RhSi.

Another interesting point in the landscape of optical responses of chiral multifold semimetals is the contribution of the surface states. We found discrepancies in the optical conductivity of two different samples of CoSi grown with different crystallographic orientations, which could be compatible with the contribution of surface states. A recent work[161] measured the Fermi arc surface states contribution to the linear and circular photogalvanic effects in RhSi. However, to this date, we do

not know of any quantitative prediction of the effect of surface states in CoSi.

The range of chiral multifold semimetals that can be grown as single-crystals and display multifold fermions near the Fermi level is limited. RhSi and CoSi constitute two of the few exceptions. However, growing cleaner samples could lead to the observation of stronger signatures of multifold fermions. In the case of RhSi, the large disorder scale prevents us from observing any signature in the spin-orbit coupling scale. With a cleaner sample of RhSi, the large energy scale of the band structure of RhSi, the energy difference between the multifolds at the Γ and R points, and the larger spin-orbit coupling scale compared to CoSi could lead to strong signatures of the spin-3/2 fourfold fermion at the zone center.

The optical responses presented here are not the only possible avenues to explore these materials. As we discussed in the introduction, the negative magnetoresistance of Weyl semimetals is a predicted consequence of the chiral anomaly associated with the topological charge of Weyl fermions. A recent experiment[162] measured the magnetoresistance of the multifold semimetal CoSi. However, they reported that a better characterization of the bulk electronic structure is needed to probe the mutifold crossings at the Γ point. Another effect associated with the chirality of Weyl fermions is the helical magnetic effect (HME), which predicts a photocurrent in the presence of a magnetic field in a tilted, asymmetric Weyl material[163]. However, Weyl semimetals satisfying the required conditions to display HME are rare. A recent work[164] showed that multifold semimetals are an ideal platform to observe the HME, since multifolds fermions can display a finite HME response in the low-energy symmetric case. In particular, they estimated that the size of the HME response in RhSi and CoSi would be comparable to the CPGE, and propose both materials as candidates to measure the HME.

Beyond further studies of chiral multifold semimetals, there is a second set of future avenues based on the optical responses presented in this thesis. In the course of the research presented in this thesis, I noticed a lack of efficient tools for computing linear and nonlinear responses of different models. Numerical calculations of nonlinear responses tend to be subtle due to the paramount presence of potentially

divergent terms that must be treated carefully. Therefore, it would be helpful to build a package for computing linear and quadratic optical responses in different materials. Based on the current implementation of the linear optical conductivity and second-harmonic generation presented in this thesis, the next step would be to expand the code to compute photogalvanic effects and non-monochromatic second-order responses, such as sum- and difference-frequency generation[104]. The latter two are likely the focus of the next generation of experiments. This code could take an arbitrary non-interacting Hamiltonian in momentum representation as an input, generated using the Kwant[165] package. This project would ultimately provide the community with a reliable, useful tool to compute optical responses efficiently, thus significantly accelerating the research in the field and the possibilities of studying new types of materials by providing helpful input for experimental research.

Ideally, the optical response package would not be limited to topological semimetals and insulators, being general enough to compute optical responses of Bogoliubov-de Gennes Hamiltonians. Recent works have studied the linear optical conductivity of multi-band superconductors in the clean limit, reporting significant contributions of previously overlooked interband momentum-conserving excitations[166]. Additionally, a study of nonlinear optical responses in superconductors with inversion symmetry breaking has reported a significant second-harmonic generation compared to the linear optical conductivity based on a 1D model[167]. These works open new fronts of research that can potentially lead to a new paradigm for the optical responses of superconductors.

I think it is especially interesting to investigate how to probe Majorana Zero Modes in superconducting phases using linear and nonlinear optical responses. The task of finding suitable optical responses to characterize the superconducting phases hosting Majorana states is challenging from the experimental and theoretical points of view. The small energies required to reach sub-gap resolution and the nanometer-size localization scales of the Majorana modes place the problem at the frontier of theoretical and experimental possibilities. However, the benefits of finding an optical probe that can discriminate Majorana states in fully contactless measurements, in contrast with the transport probes frequently used, could be enormous, potentially leading to a new generation of experiments.

The research developed in this thesis can be extended in multiple directions, as discussed in this chapter. Multifold semimetals are a recent addition to the family of topological materials. They display interesting effects, such as the quantized CPGE[96,111,113], and are candidates to feature other phenomena, such as the HME[164]. However, more research is needed to characterize these materials. Our work is one of the first steps in this direction. The optical responses studied throughout this thesis are not limited to multifold fermions. However, the calculation of nonlinear optical responses can be challenging, and the work developed in this thesis could be the first step to build a package capable of computing optical responses in a variety of materials, ranging from topological semimetals and insulators to superconducting phases.

Appendices

A

Optical conductivity of a tetrahedral fourfold fermion

At linear order, the $k \cdot p$ Hamiltonian of a tetrahedral fourfold fermion admits an extra term compared to the octahedral fourfold in Eq. 2.23. We recall here the expression for the tetrahedral Hamiltonian, presented in Eq. 2.27,

$$H_{4f,T} = H_{4f} + \hbar v_T \begin{pmatrix} 0 & k_z & -\sqrt{3}k_x & ik_y \\ k_z & \frac{2k_z}{\sqrt{3}} & ik_y & \frac{k_x - 2ik_y}{\sqrt{3}} \\ -\sqrt{3}k_x & -ik_y & 0 & -k_z \\ -ik_y & \frac{k_x + 2ik_y}{\sqrt{3}} & -k_z & -\frac{2k_z}{\sqrt{3}} \end{pmatrix}, \quad \text{(A.1)}$$

where H_{4f} is the octahedral fourfold Hamiltonian given in Eq. 2.23. The parameter v_T is proportional to the strength of the fourfold rotational symmetry breaking.

By changing v_T we introduce a tilt in the bands (see Fig. A.1 (a)), breaking the full rotational symmetry. For finite v_T, the optical selection

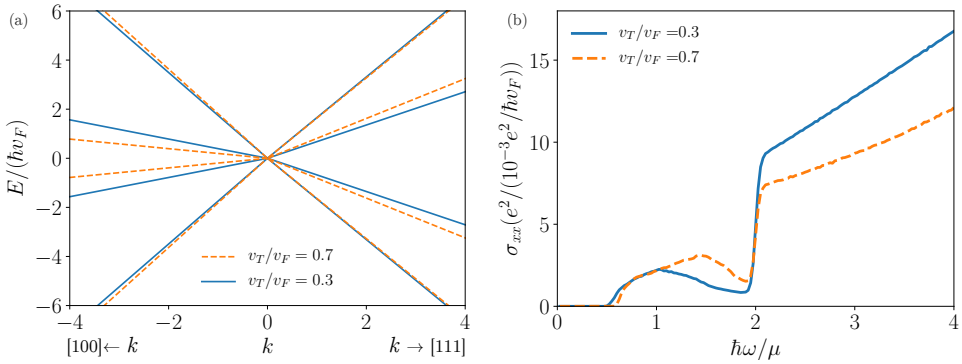

Figure A.1: Optical conductivity of a tetrahedral fourfold fermion. (a) Band structure and (b) optical conductivity corresponding to the tetrahedral fourfold fermion with two different values of the ratio v_T/v_F (see Eq. 2.27).

rules of the symmetric fourfold do not apply, leading to a different optical conductivity (Fig. A.1 (b)) compared to the symmetric fourfold case (see Eq. 3.34 and Fig. 3.2).

B

Temperature and broadening of the step function

In Chapter 3 we have derived analytic expressions for the optical conductivity of the symmetric threefold and symmetric fourfold fermions (Eqs. 3.31 and 3.33, respectively) for any temperature $T = 1/(k_B\beta)$. In Fig. B.1 we plot the optical conductivities for the Weyl, symmetric threefold and symmetric fourfold fermions at zero temperature and at a finite (unrealistic) temperature $1/\beta = 10^{-1}\mu$ to illustrate the broadening of the step functions at the characteristic frequencies. In units of μ the broadening, set by $\mu\beta$, is larger for the step function at 2μ than at μ or $2/3\mu$, which is clearly visible in Fig. B.1.

The broadening due to a finite temperature is visible as well in our calculations for realistic models in Sec. 3.4.

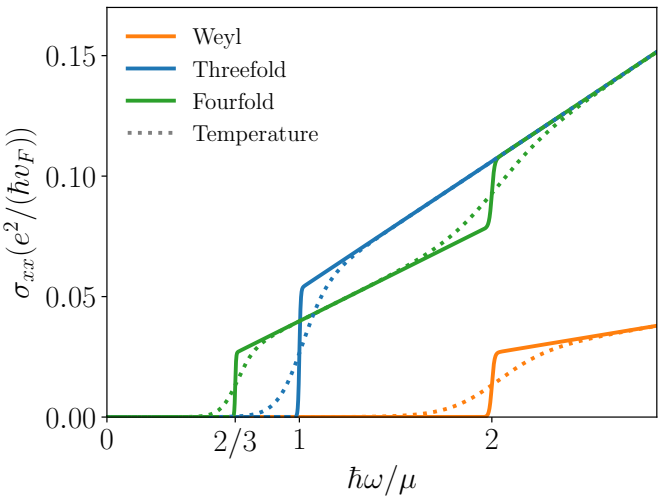

Figure B.1: Optical conductivity of symmetric models with finite temperature. The solid lines correspond to that of Fig. 3.2 and the dashed lines (with the same color coding) are calculated with the exact analytic expressions Eqs. 3.30, 3.31 and 3.33 for finite temperature with $1/\beta = 10^{-1}\mu$.

C

Imaginary part of the optical conductivity from the Kramers-Kronig relations

The optical conductivity is a complex quantity with real ($\mathrm{Re}[\sigma] \equiv \sigma_{\mathfrak{Re}}$) and imaginary ($\mathrm{Im}[\sigma] \equiv \sigma_{\mathfrak{Im}}$) parts $\sigma = \sigma_{\mathfrak{Re}} + i\sigma_{\mathfrak{Im}}$ which are related by the Kramers-Kronig relations[94]. In Chapter 3 we have calculated the absorptive (real) part of the optical conductivity. Using the Kramers-Kronig relations we can obtain the dispersive (imaginary) part of the optical conductivity. The Kramers-Kronig relations are commonly written as[94]

$$\sigma_{\mathfrak{Re}}(\omega) = \frac{1}{\pi}\mathcal{P}\int_{-\infty}^{\infty} \mathrm{d}x \frac{\sigma_{\mathfrak{Im}}(x)}{x-\omega}, \tag{C.1}$$

$$\sigma_{\mathfrak{Im}}(\omega) = -\frac{1}{\pi}\mathcal{P}\int_{-\infty}^{\infty} \mathrm{d}x \frac{\sigma_{\mathfrak{Re}}(x)}{x-\omega}, \tag{C.2}$$

where $\mathcal{P}$ denotes the Cauchy principal value. To calculate it we follow the procedure in Ref. [94] and subtract the singularity at ω

$$\sigma_{\mathfrak{Re}}(\omega) + i\sigma_{\mathfrak{Im}}(\omega) = \frac{1}{i\pi}\int_{-\infty}^{\infty} \mathrm{d}x \left(\frac{\sigma(x)-\sigma(\omega)}{x-\omega}\right)\left(\frac{x+\omega}{x+\omega}\right). \tag{C.3}$$

Using now that the real part is even and the imaginary part is odd in frequencies we obtain

$$\sigma_{\mathfrak{Re}}(\omega) = \frac{2}{\pi}\int_0^{\infty} \mathrm{d}x \frac{x\sigma_{\mathfrak{Im}}(x) - \omega\sigma_{\mathfrak{Im}}(\omega)}{x^2-\omega^2}, \tag{C.4}$$

$$\sigma_{\mathfrak{Im}}(\omega) = -\frac{2\omega}{\pi}\int_0^{\infty} \mathrm{d}x \frac{\sigma_{\mathfrak{Re}}(x) - \sigma_{\mathfrak{Re}}(\omega)}{x^2-\omega^2}. \tag{C.5}$$

Since the low-energy models that we used in Chapter 3 to calculate the real part of the optical conductivity have unbounded linearly dispersing bands, we regularize the upper limit in the integrals in Eqs. C.4 and C.5 using a cutoff frequency Λ. The real part of the optical conductivity of all chiral multifold fermions (see Table 2.1) is a piecewise function of the form $\sigma_{\mathfrak{Re}}(\omega) = \sum_{i=0}^{N-1}\sigma_i(\omega) = \sum_{i=0}^{N-1} S_i\omega\Theta(\omega_{i+1}-\omega_i)$. The subindex i is associated to each characteristic frequency ω_i where the slope of the optical conductivity changes (see Sec. 3.2.1), where $\omega_0 = 0$, $\omega_N = \Lambda/\hbar$ is the cutoff frequency, and N is the number of different frequency regions. In particular, $N = 7$ and $N = 10$ for threefold and fourfold fermions as dictated by Eqs. 3.35 and 3.36 respectively. Using this partition for the optical conductivity we can rewrite now Eq. C.5 as

$$\begin{aligned}\sigma_{\mathfrak{Im}}(\omega,\Lambda) &= -\frac{2\omega}{\pi}\left[\sum_{i=0}^{N-1}\int_{\omega_i}^{\omega_{i+1}} \frac{\sigma_i(x)}{x^2-\omega^2}\mathrm{d}x - \int_0^{\infty}\frac{\sigma_{\mathfrak{Re}}(\omega)}{x^2-\omega^2}\mathrm{d}x\right] \\ &= -\frac{1}{\pi}\left[\sigma_{\mathfrak{Re}}(\omega)\log\left|\frac{\Lambda+\hbar\omega}{\Lambda-\hbar\omega}\right| + \omega\sum_{i=0}^{N-1} S_i \log\left|\frac{\omega_{i+1}^2-\omega^2}{\omega_i^2-\omega^2}\right|\right].\end{aligned} \tag{C.6}$$

This expression can be evaluated analytically for the cases of the twofold (Weyl), the symmetric threefold, and the symmetric fourfold fermions (see Fig. C.1) presented in Table 3.1. For the Weyl fermion we obtain

$$\sigma_{\mathfrak{Im},W}(\omega) = -\frac{\omega e^2}{24\pi^2\hbar v_F}\left[\log\left|\frac{\Lambda^2-(\hbar\omega)^2}{4\mu^2-(\hbar\omega)^2}\right| + \Theta(\hbar\omega-2\mu)\log\left|\frac{\Lambda+\hbar\omega}{\Lambda-\hbar\omega}\right|\right]. \tag{C.7}$$

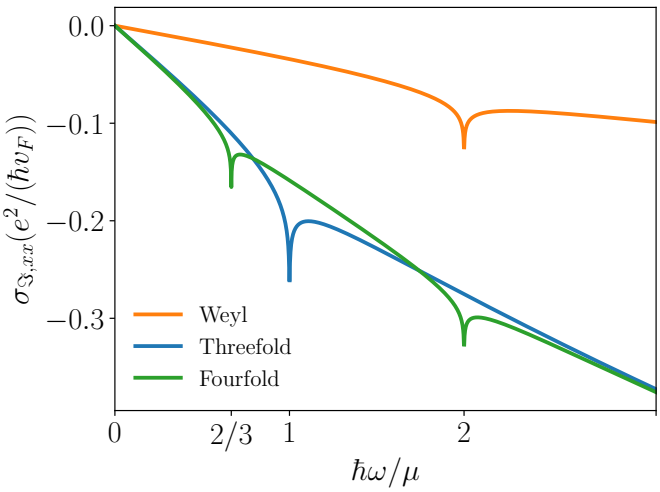

Figure C.1: Imaginary part of the optical conductivity for a Weyl fermion (orange), a symmetric threefold fermion (blue), and a symmetric fourfold fermion (green) as dictated by Eqs. C.7, C.8, C.9 with $\Lambda = 100\mu$.

We take the result obtained for the symmetric threefold in Eq. 3.32, and we obtain the corresponding imaginary part

$$\sigma^{\phi_0}_{\Im\mathfrak{m},3f}(\omega) = -\frac{\omega e^2}{6\pi^2\hbar v_F}\left[\log\left|\frac{\Lambda^2-(\hbar\omega)^2}{\mu^2-(\hbar\omega)^2}\right| + \Theta(\hbar\omega-\mu)\log\left|\frac{\Lambda+\hbar\omega}{\Lambda-\hbar\omega}\right|\right]. \tag{C.8}$$

For the symmetric fourfold fermion

$$\sigma^{\chi_0}_{\Im\mathfrak{m},4f}(\omega) = -\frac{\omega e^2}{24\pi^2\hbar v_F}\left[4\log\left|\frac{\Lambda^2-(\hbar\omega)^2}{4\mu^2-(\hbar\omega)^2}\right| + 3\log\left|\frac{36\mu^2-9(\hbar\omega)^2}{4\mu^2-9(\hbar\omega)^2}\right| + \left(3\Theta\left(\hbar\omega-\frac{2\mu}{3}\right)+\Theta(\hbar\omega-2\mu)\right)\log\left|\frac{\Lambda+\hbar\omega}{\Lambda-\hbar\omega}\right|\right]. \tag{C.9}$$

For the non-symmetric multifold fermions, the characteristic frequencies can be calculated analytically for each ϕ, χ using Eqs. 3.35 and 3.36. The slopes for each piece S_i can be calculated numerically and introduced in Eq. C.6 to obtain the corresponding imaginary part of the optical conductivity.

D

Sum rules

Optical sum rules relate the real part of the optical conductivity ($\mathrm{Re}[\sigma] \equiv \sigma_{\mathfrak{Re}}$) with the total number of particles in the system, and are obtained as the integral of the optical conductivity to all frequencies,

$$\langle \sigma \rangle = \hbar^2 \int_0^\infty \mathrm{d}\omega \sigma_{\mathfrak{Re}}(\omega). \tag{D.1}$$

As for the Kramers-Kronig relations, the unbounded linear dispersion of the effective low-energy models requires us to insert a cutoff frequency Λ in Eq. D.1 to regularize the integral. As discussed in the previous section, we will use that the optical conductivity of these models is of the form $\sigma_{\mathfrak{Re}}(\omega) = \sum_{i=0}^{N-1} \sigma_i = \sum_{i=0}^{N-1} S_i \omega \Theta(\omega_{i+1} - \omega_i)$ for both symmetric and non symmetric cases. Introducing this general form in Eq. D.1 as well as the cut-off Λ we obtain a general expression for the sum rule for all multifold fermions:

$$\begin{aligned} \hbar^2 \int_0^{\Lambda/\hbar} \mathrm{d}\omega \sigma_{\mathfrak{Re}}(\omega) &= \hbar^2 \sum_{i=0}^{N-1} \int_0^{\Lambda/\hbar} \mathrm{d}\omega S_i \omega \Theta(\omega_{i+1} - \omega_i) \\ &= \hbar^2 \frac{e^2}{2\hbar v_F} \sum_{i=0}^{N-1} S_i (\omega_{i+1}^2 - \omega_i^2). \end{aligned} \tag{D.2}$$

To obtain analytic results for the symmetric cases we insert the optical conductivities in Table 3.1 in Eq. D.2. In the twofold (Weyl) case we obtain

$$\langle\sigma\rangle_{2f} = \frac{e^2}{48\pi\hbar v_{\mathrm{F}}}\left(\Lambda^2 - 4\mu^2\right). \tag{D.3}$$

For the symmetric threefold fermion we obtain that

$$\langle\sigma\rangle_{3f} = \frac{e^2}{12\pi\hbar v_{\mathrm{F}}}\left(\Lambda^2 - \mu^2\right). \tag{D.4}$$

In the symmetric fourfold case the optical sum rule is

$$\langle\sigma\rangle_{4f} = \frac{e^2}{12\pi\hbar v_F}\left(\Lambda^2 - \frac{4}{3}\mu^2\right). \tag{D.5}$$

For the non symmetric cases the frequencies at which the linear dependence of the optical conductivity on ω changes are given by Eqs. 3.35 and 3.36 for the threefold and fourfold fermions, respectively. In this case, the linear dependence S_i in each section $\omega_i < \omega < \omega_{i+1}$ can be computed numerically and substituted in Eq. D.2 to obtain the corresponding sum rule.

Finally, note that the Drude peak will contribute to the sum rule as well. Extending the results of Ref. [100] to three-dimensions, we expect its contribution to be proportional to μ^2.

E

Parallelized code for computing second-harmonic generation

To obtain results in reasonable time scales we wrote a parallel code in Julia using the package `Distributed` included in the standard Julia library. This code was optimized to minimize the data transfer between different nodes by creating a momentum mesh with a number of points exactly divisible by the number of available nodes for the run. As a result, whole blocks of momentum-space resolved quantities were computed in each node, diagonalizing the Hamiltonian locally and avoiding unnecessary communication between different nodes.

The code was implemented to run in the local cluster at Institut Néel and to compute multiple values of disorder and chemical potential in a single run, computing the disorder- and Fermi-energy-independent elements r^a_{mn}, ω_{mn}, and Δ^a_{mn} for each term in $\chi^{abc}(2\omega;\omega,\omega)$ (Eq. 5.4) a single time. The disorder-dependent denominators $1/(\omega + i\eta)$ and Fermi-energy dependent terms f_{mn} were computed separately for each pair (η, E_F), and the final results of the combined contributions stored independently.

The code provides stable results and good convergence for **k**-mesh larger than $25 \times 25 \times 25$. It it interesting to note that the $k \cdot p$ model used to describe the threefold node at Γ in Sec. 5.3.2 features a degeneracy in the energy differences ω_{mn} between pairs of bands for $b = 0$. The $\omega_{ab} - \omega_{cd}$ terms in the denominators of the interband contributions of $\chi^{abc}(2\omega; \omega, \omega)$ become zero for $b = 0$, leading to stability and convergence problems in the calculation. This issue is easily overcome by choosing a different set of parameters to fit the $k \cdot p$ model to the tight-binding model at the Γ point. Since the set of parameters that provide the best fit is not unique, it is relatively easy to find a good description of the threefold node at Γ with $b \neq 0$.

F

Accounting for many-body effects in the second-harmonic generation of RhSi: scissors potential in DFT calculations

While DFT calculations can provide a good description for ground-state properties and occupied states, treating unoccupied states is more challenging. During the optical transitions, the unoccupied states can be occupied by the electron as a result of intermediate-state processes. The description used in the $k \cdot p$ and tight-binding models lacks any consideration of many-body effects, and this might lead to wrong results when evaluating the energies at which the photons will be absorbed[142,168,169].

To tackle the problem of innacurate energy differences between occupied and unoccupied bands when considering many-body effects we consider a scissors shift Δ[153,170–173]. Under the scissors approximation, the position and velocity matrix elements are modified by the potential

Δ as

$$r_{nm} = \frac{\tilde{v}_{nm}}{\mathrm{i}\left[\omega_{nm} + \frac{\Delta}{\hbar}(\delta_n^{\mathrm{unoc}} - \delta_m^{\mathrm{unoc}})\right]}, \tag{F.1}$$

$$\tilde{v}_{nm} = v_{nm}\frac{\omega_{nm} + \frac{\Delta}{\hbar}(\delta_n^{\mathrm{unoc}} - \delta_m^{\mathrm{unoc}})}{\omega_{nm}}, \tag{F.2}$$

where δ_n^{unoc} is the Kronecker delta for unoccupied state n.

Bibliography

[1] A. A. Michelson, *Light waves and their uses*, vol. 3. University of Chicago Press, 1902.

[2] A. Einstein, "Über einen die erzeugung und verwandlung des lichtes betreffenden heuristischen gesichtspunkt," *Annalen der Physik*, vol. 322, no. 6, pp. 132–148, 1905.

[3] A. Einstein, "Über die von der molekularkinetischen theorie der warme geforderte bewegung von in ruhenden flüssigkeiten suspendierten teilchen," *Ann Phys*, vol. 322, pp. 549–560, 1905.

[4] A. Einstein, "Zur elektrodynamik bewegter körper," *Annalen der physik*, vol. 4, 1905.

[5] A. Einstein, "Ist die trägheit eines körpers von seinem energieinhalt abhängig?," *Annalen der Physik*, vol. 323, no. 13, pp. 639–641, 1905.

[6] A. Pais, *Inward bound: of matter and forces in the physical world*. Oxford University Press, 1986.

[7] K. v. Klitzing, G. Dorda, and M. Pepper, "New method for high-accuracy determination of the fine-structure constant based on quantized Hall resistance," *Phys. Rev. Lett.*, vol. 45, pp. 494–497, Aug 1980.

[8] N. Armitage, E. Mele, and A. Vishwanath, "Weyl and Dirac semimetals in three-dimensional solids," *Reviews of Modern Physics*, vol. 90, Jan. 2018.

[9] M. V. Berry, "Quantal phase factors accompanying adiabatic changes," *Proceedings of the Royal Society of London. A.*

Mathematical and Physical Sciences, vol. 392, no. 1802, pp. 45–57, 1984.

[10] R. Moessner and J. E. Moore, *Topological Phases of Matter*. Cambridge University Press, 2021.

[11] A. Damascelli, Z. Hussain, and Z.-X. Shen, "Angle-resolved photoemission studies of the cuprate superconductors," *Rev. Mod. Phys.*, vol. 75, pp. 473–541, Apr 2003.

[12] M. Z. Hasan and C. L. Kane, "Colloquium: Topological insulators," *Rev. Mod. Phys.*, vol. 82, pp. 3045–3067, Nov 2010.

[13] Z. Liu, B. Zhou, Y. Zhang, Z. Wang, H. Weng, D. Prabhakaran, S.-K. Mo, Z. Shen, Z. Fang, X. Dai, *et al.*, "Discovery of a three-dimensional topological Dirac semimetal, Na_3Bi," *Science*, vol. 343, no. 6173, pp. 864–867, 2014.

[14] S.-Y. Xu, C. Liu, S. K. Kushwaha, R. Sankar, J. W. Krizan, I. Belopolski, M. Neupane, G. Bian, N. Alidoust, T.-R. Chang, H.-T. Jeng, C.-Y. Huang, W.-F. Tsai, H. Lin, P. P. Shibayev, F.-C. Chou, R. J. Cava, and M. Z. Hasan, "Observation of fermi arc surface states in a topological metal," *Science*, vol. 347, no. 6219, pp. 294–298, 2015.

[15] S. Borisenko, Q. Gibson, D. Evtushinsky, V. Zabolotnyy, B. Büchner, and R. J. Cava, "Experimental realization of a three-dimensional dirac semimetal," *Phys. Rev. Lett.*, vol. 113, p. 027603, Jul 2014.

[16] Z. Liu, J. Jiang, B. Zhou, Z. Wang, Y. Zhang, H. Weng, D. Prabhakaran, S. Mo, H. Peng, P. Dudin, *et al.*, "A stable three-dimensional topological Dirac semimetal Cd_3As_2," *Nat. Mater.*, vol. 13, no. 7, p. 677, 2014.

[17] M. Neupane, S.-Y. Xu, R. Sankar, N. Alidoust, G. Bian, C. Liu, I. Belopolski, T.-R. Chang, H.-T. Jeng, H. Lin, *et al.*, "Observation of a three-dimensional topological Dirac semimetal phase in high-mobility Cd_3As_2," *Nat. Commun.*, vol. 5, p. 3786, 2014.

[18] S. Jeon, B. B. Zhou, A. Gyenis, B. E. Feldman, I. Kimchi, A. C. Potter, Q. D. Gibson, R. J. Cava, A. Vishwanath, and

A. Yazdani, "Landau quantization and quasiparticle interference in the three-dimensional Dirac semimetal Cd_3As_2," *Nature Materials*, vol. 13, pp. 851–856, Sept. 2014.

[19] A. Akrap, M. Hakl, S. Tchoumakov, I. Crassee, J. Kuba, M. O. Goerbig, C. C. Homes, O. Caha, J. Novák, F. Teppe, W. Desrat, S. Koohpayeh, L. Wu, N. P. Armitage, A. Nateprov, E. Arushanov, Q. D. Gibson, R. J. Cava, D. van der Marel, B. A. Piot, C. Faugeras, G. Martinez, M. Potemski, and M. Orlita, "Magneto-optical signature of massless Kane electrons in Cd_3As_2," *Phys. Rev. Lett.*, vol. 117, p. 136401, Sep 2016.

[20] X. Wan, A. M. Turner, A. Vishwanath, and S. Y. Savrasov, "Topological semimetal and Fermi-arc surface states in the electronic structure of pyrochlore iridates," *Phys. Rev. B*, vol. 83, p. 205101, May 2011.

[21] W. Witczak-Krempa and Y. B. Kim, "Topological and magnetic phases of interacting electrons in the pyrochlore iridates," *Phys. Rev. B*, vol. 85, p. 045124, Jan 2012.

[22] M. C. Shapiro, S. C. Riggs, M. B. Stone, C. R. de la Cruz, S. Chi, A. A. Podlesnyak, and I. R. Fisher, "Structure and magnetic properties of the pyrochlore iridate $Y_2Ir_2O_7$," *Phys. Rev. B*, vol. 85, p. 214434, Jun 2012.

[23] H. Liu, W. Tong, L. Ling, S. Zhang, R. Zhang, L. Zhang, L. Pi, C. Zhang, and Y. Zhang, "Magnetic order, spin dynamics and transport properties of the pyrochlore iridate $Y_2Ir_2O_7$," *Solid State Communications*, vol. 179, pp. 1–5, 2014.

[24] A. A. Burkov and L. Balents, "Weyl semimetal in a topological insulator multilayer," *Phys. Rev. Lett.*, vol. 107, p. 127205, Sep 2011.

[25] G. Xu, H. Weng, Z. Wang, X. Dai, and Z. Fang, "Chern semimetal and the quantized anomalous Hall effect in $HgCr_2Se_4$," *Phys. Rev. Lett.*, vol. 107, p. 186806, Oct 2011.

[26] S.-M. Huang, S.-Y. Xu, I. Belopolski, C.-C. Lee, G. Chang, B. Wang, N. Alidoust, G. Bian, M. Neupane, C. Zhang, S. Jia, A. Bansil, H. Lin, and M. Z. Hasan, "A Weyl Fermion semimetal

with surface Fermi arcs in the transition metal monopnictide TaAs class," *Nature Communications*, vol. 6, p. 7373, June 2015.

[27] H. Weng, C. Fang, Z. Fang, B. A. Bernevig, and X. Dai, "Weyl semimetal phase in noncentrosymmetric transition-metal monophosphides," *Phys. Rev. X*, vol. 5, no. 1, p. 011029, 2015.

[28] S.-Y. Xu, I. Belopolski, N. Alidoust, M. Neupane, G. Bian, C. Zhang, R. Sankar, G. Chang, Z. Yuan, C.-C. Lee, *et al.*, "Discovery of a Weyl fermion semimetal and topological Fermi arcs," *Science*, vol. 349, no. 6248, pp. 613–617, 2015.

[29] B. Lv, H. Weng, B. Fu, X. Wang, H. Miao, J. Ma, P. Richard, X. Huang, L. Zhao, G. Chen, *et al.*, "Experimental discovery of Weyl semimetal TaAs," *Phys. Rev. X*, vol. 5, no. 3, p. 031013, 2015.

[30] L. X. Yang, Z. K. Liu, Y. Sun, H. Peng, H. F. Yang, T. Zhang, B. Zhou, Y. Zhang, Y. F. Guo, M. Rahn, D. Prabhakaran, Z. Hussain, S. K. Mo, C. Felser, B. Yan, and Y. L. Chen, "Weyl semimetal phase in the non-centrosymmetric compound TaAs," *Nature Physics*, vol. 11, no. 9, pp. 728–732, 2015.

[31] L. Lu, Z. Wang, D. Ye, L. Ran, L. Fu, J. D. Joannopoulos, and M. Soljačić, "Experimental observation of Weyl points," *Science*, vol. 349, no. 6248, pp. 622–624, 2015.

[32] S.-Y. Xu, N. Alidoust, I. Belopolski, Z. Yuan, G. Bian, T.-R. Chang, H. Zheng, V. N. Strocov, D. S. Sanchez, G. Chang, *et al.*, "Discovery of a Weyl fermion state with Fermi arcs in niobium arsenide," *Nat. Phys.*, vol. 11, no. 9, p. 748, 2015.

[33] B. Lv, N. Xu, H. Weng, J. Ma, P. Richard, X. Huang, L. Zhao, G. Chen, C. Matt, F. Bisti, *et al.*, "Observation of Weyl nodes in TaAs," *Nat. Phys.*, vol. 11, no. 9, p. 724, 2015.

[34] S.-Y. Xu, I. Belopolski, D. S. Sanchez, C. Zhang, G. Chang, C. Guo, G. Bian, Z. Yuan, H. Lu, T.-R. Chang, P. P. Shibayev, M. L. Prokopovych, N. Alidoust, H. Zheng, C.-C. Lee, S.-M. Huang, R. Sankar, F. Chou, C.-H. Hsu, H.-T. Jeng, A. Bansil, T. Neupert, V. N. Strocov, H. Lin, S. Jia, and M. Z. Hasan, "Experimental discovery of a topological weyl semimetal state in TaP," *Science Advances*, vol. 1, no. 10, 2015.

[35] N. Xu, H. M. Weng, B. Q. Lv, C. E. Matt, J. Park, F. Bisti, V. N. Strocov, D. Gawryluk, E. Pomjakushina, K. Conder, N. C. Plumb, M. Radovic, G. Autès, O. V. Yazyev, Z. Fang, X. Dai, T. Qian, J. Mesot, H. Ding, and M. Shi, "Observation of Weyl nodes and Fermi arcs in tantalum phosphide," *Nature Communications*, vol. 7, p. 11006, Mar. 2016.

[36] I. Belopolski, S.-Y. Xu, D. S. Sanchez, G. Chang, C. Guo, M. Neupane, H. Zheng, C.-C. Lee, S.-M. Huang, G. Bian, N. Alidoust, T.-R. Chang, B. Wang, X. Zhang, A. Bansil, H.-T. Jeng, H. Lin, S. Jia, and M. Z. Hasan, "Criteria for directly detecting topological fermi arcs in weyl semimetals," *Phys. Rev. Lett.*, vol. 116, p. 066802, Feb 2016.

[37] Z. K. Liu, L. X. Yang, Y. Sun, T. Zhang, H. Peng, H. F. Yang, C. Chen, Y. Zhang, Y. F. Guo, D. Prabhakaran, M. Schmidt, Z. Hussain, S.-K. Mo, C. Felser, B. Yan, and Y. L. Chen, "Evolution of the Fermi surface of Weyl semimetals in the transition metal pnictide family," *Nature Materials*, vol. 15, pp. 27–31, Jan. 2016.

[38] B. Q. Lv, S. Muff, T. Qian, Z. D. Song, S. M. Nie, N. Xu, P. Richard, C. E. Matt, N. C. Plumb, L. X. Zhao, G. F. Chen, Z. Fang, X. Dai, J. H. Dil, J. Mesot, M. Shi, H. M. Weng, and H. Ding, "Observation of Fermi-arc spin texture in TaAs," *Phys. Rev. Lett.*, vol. 115, p. 217601, Nov 2015.

[39] S.-Y. Xu, I. Belopolski, D. S. Sanchez, M. Neupane, G. Chang, K. Yaji, Z. Yuan, C. Zhang, K. Kuroda, G. Bian, C. Guo, H. Lu, T.-R. Chang, N. Alidoust, H. Zheng, C.-C. Lee, S.-M. Huang, C.-H. Hsu, H.-T. Jeng, A. Bansil, T. Neupert, F. Komori, T. Kondo, S. Shin, H. Lin, S. Jia, and M. Z. Hasan, "Spin polarization and texture of the Fermi arcs in the Weyl fermion semimetal TaAs," *Phys. Rev. Lett.*, vol. 116, p. 096801, Mar 2016.

[40] H. Zheng, S.-Y. Xu, G. Bian, C. Guo, G. Chang, D. S. Sanchez, I. Belopolski, C.-C. Lee, S.-M. Huang, X. Zhang, R. Sankar, N. Alidoust, T.-R. Chang, F. Wu, T. Neupert, F. Chou, H.-T. Jeng, N. Yao, A. Bansil, S. Jia, H. Lin, and M. Z. Hasan, "Atomic-scale visualization of quantum interference on a Weyl semimetal surface by scanning tunneling microscopy," *ACS Nano*, vol. 10, Jan. 2016.

[41] H. Inoue, A. Gyenis, Z. Wang, J. Li, S. W. Oh, S. Jiang, N. Ni, B. A. Bernevig, and A. Yazdani, "Quasiparticle interference of the Fermi arcs and surface-bulk connectivity of a Weyl semimetal," *Science*, vol. 351, no. 6278, pp. 1184–1187, 2016.

[42] R. Batabyal, N. Morali, N. Avraham, Y. Sun, M. Schmidt, C. Felser, A. Stern, B. Yan, and H. Beidenkopf, "Visualizing weakly bound surface Fermi arcs and their correspondence to bulk Weyl fermions," *Science Advances*, vol. 2, no. 8, 2016.

[43] H. Nielsen and M. Ninomiya, "The Adler-Bell-Jackiw anomaly and Weyl fermions in a crystal," *Physics Letters B*, vol. 130, pp. 389–396, Nov. 1983.

[44] D. T. Son and B. Z. Spivak, "Chiral anomaly and classical negative magnetoresistance of Weyl metals," *Physical Review B*, vol. 88, Sept. 2013.

[45] A. Burkov, "Chiral anomaly and transport in Weyl metals," *Journal of Physics: Condensed Matter*, vol. 27, no. 11, p. 113201, 2015.

[46] W. Reed, E. Blount, J. Marcus, and A. Arko, "Anomalous longitudinal magnetoresistance in metals," *Journal of Applied Physics*, vol. 42, no. 13, pp. 5453–5459, 1971.

[47] K. Yoshida, "Anomalous electric fields in semimetals under high magnetic fields," *Journal of the Physical Society of Japan*, vol. 39, no. 6, pp. 1473–1481, 1975.

[48] K. Yoshida, "A geometrical transport model for inhomogeneous current distribution in semimetals under high magnetic fields," *Journal of the Physical Society of Japan*, vol. 40, no. 4, pp. 1027–1034, 1976.

[49] K. Yoshida, "An anomalous behavior of the longitudinal magnetoresistance in semimetals," *Journal of the Physical Society of Japan*, vol. 41, no. 2, pp. 574–581, 1976.

[50] K. Yoshida, "Transport of spatially inhomogeneous current in a compensated metal under magnetic fields. iii. a case of bismuth in longitudinal and transverse magnetic fields," *Journal of Applied Physics*, vol. 51, no. 8, pp. 4226–4233, 1980.

[51] F. Arnold, C. Shekhar, S.-C. Wu, Y. Sun, R. D. dos Reis, N. Kumar, M. Naumann, M. O. Ajeesh, M. Schmidt, A. G. Grushin, *et al.*, "Negative magnetoresistance without well-defined chirality in the Weyl semimetal TaP," *Nat. Commun.*, vol. 7, 2016.

[52] T. Ando, Y. Zheng, and H. Suzuura, "Dynamical conductivity and zero-mode anomaly in honeycomb lattices," *Journal of the Physical Society of Japan*, vol. 71, no. 5, pp. 1318–1324, 2002.

[53] A. B. Kuzmenko, E. van Heumen, F. Carbone, and D. van der Marel, "Universal optical conductance of graphite," *Phys. Rev. Lett.*, vol. 100, p. 117401, Mar 2008.

[54] R. R. Nair, P. Blake, A. N. Grigorenko, K. S. Novoselov, T. J. Booth, T. Stauber, N. M. R. Peres, and A. K. Geim, "Fine structure constant defines visual transparency of graphene," *Science*, vol. 320, no. 5881, p. 1308, 2008.

[55] P. Hosur, S. A. Parameswaran, and A. Vishwanath, "Charge transport in Weyl semimetals," *Physical Review Letters*, vol. 108, Jan. 2012.

[56] P. Hosur and X. Qi, "Recent developments in transport phenomena in Weyl semimetals," *Comptes Rendus Physique*, vol. 14, no. 9, pp. 857–870, 2013.

[57] C. J. Tabert, J. P. Carbotte, and E. J. Nicol, "Optical and transport properties in three-dimensional Dirac and Weyl semimetals," *Physical Review B*, vol. 93, Feb. 2016.

[58] Á. Bácsi and A. Virosztek, "Low-frequency optical conductivity in graphene and in other scale-invariant two-band systems," *Phys. Rev. B*, vol. 87, no. 12, p. 125425, 2013.

[59] Q. Ma, A. G. Grushin, and K. S. Burch, "Topology and geometry under the nonlinear electromagnetic spotlight," *Nature Materials*, pp. 1–14, 2021.

[60] J. E. Moore and J. Orenstein, "Confinement-induced Berry phase and helicity-dependent photocurrents," *Phys. Rev. Lett.*, vol. 105, p. 026805, Jul 2010.

[61] I. Sodemann and L. Fu, "Quantum nonlinear Hall effect induced by Berry curvature dipole in time-reversal invariant materials," *Phys. Rev. Lett.*, vol. 115, p. 216806, Nov 2015.

[62] F. de Juan, A. G. Grushin, T. Morimoto, and J. E. Moore, "Quantized circular photogalvanic effect in Weyl semimetals," *Nat. Commun.*, vol. 8, p. 15995, 2017.

[63] C.-K. Chan, N. H. Lindner, G. Refael, and P. A. Lee, "Photocurrents in Weyl semimetals," *Phys. Rev. B*, vol. 95, p. 041104, Jan 2017.

[64] E. J. König, H.-Y. Xie, D. A. Pesin, and A. Levchenko, "Photogalvanic effect in Weyl semimetals," *Phys. Rev. B*, vol. 96, p. 075123, Aug 2017.

[65] Y. Zhang, H. Ishizuka, J. van den Brink, C. Felser, B. Yan, and N. Nagaosa, "Photogalvanic effect in Weyl semimetals from first principles," *Phys. Rev. B*, vol. 97, no. 24, p. 241118, 2018.

[66] L. Wu, S. Patankar, T. Morimoto, N. L. Nair, E. Thewalt, A. Little, J. G. Analytis, J. E. Moore, and J. Orenstein, "Giant anisotropic nonlinear optical response in transition metal monopnictide Weyl semimetals," *Nat. Phys.*, vol. 13, no. 4, p. 350, 2017.

[67] S. Patankar, L. Wu, B. Lu, M. Rai, J. D. Tran, T. Morimoto, D. E. Parker, A. G. Grushin, N. Nair, J. Analytis, *et al.*, "Resonance-enhanced optical nonlinearity in the Weyl semimetal TaAs," *Phys. Rev. B*, vol. 98, no. 16, p. 165113, 2018.

[68] S. Patankar, L. Wu, B. Lu, M. Rai, J. D. Tran, T. Morimoto, D. E. Parker, A. G. Grushin, N. L. Nair, J. G. Analytis, J. E. Moore, J. Orenstein, and D. H. Torchinsky, "Resonance-enhanced optical nonlinearity in the weyl semimetal taas," *Phys. Rev. B*, vol. 98, p. 165113, Oct 2018.

[69] M. Z. Hasan, G. Chang, I. Belopolski, G. Bian, S.-Y. Xu, and J.-X. Yin, "Weyl, Dirac and high-fold chiral fermions in topological quantum matter," *Nature Reviews Materials*, Apr. 2021.

[70] B. Bradlyn, J. Cano, Z. Wang, M. G. Vergniory, C. Felser, R. J. Cava, and B. A. Bernevig, "Beyond Dirac and Weyl fermions:

Unconventional quasiparticles in conventional crystals," *Science*, vol. 353, p. aaf5037, Aug. 2016.

[71] F. Flicker, F. De Juan, B. Bradlyn, T. Morimoto, M. G. Vergniory, and A. G. Grushin, "Chiral optical response of multifold fermions," *Phys. Rev. B*, vol. 98, no. 15, p. 155145, 2018.

[72] P. Tang, Q. Zhou, and S.-C. Zhang, "Multiple types of topological fermions in transition metal silicides," *Phys. Rev. Lett.*, vol. 119, no. 20, p. 206402, 2017.

[73] D. A. Pshenay-Severin, Y. V. Ivanov, A. A. Burkov, and A. T. Burkov, "Band structure and unconventional electronic topology of CoSi," *Journal of Physics: Condensed Matter*, vol. 30, p. 135501, mar 2018.

[74] B. Xu, Z. Fang, M.-Á. Sánchez-Martínez, J. W. F. Venderbos, Z. Ni, T. Qiu, K. Manna, K. Wang, J. Paglione, C. Bernhard, C. Felser, E. J. Mele, A. G. Grushin, A. M. Rappe, and L. Wu, "Optical signatures of multifold fermions in the chiral topological semimetal CoSi," *Proceedings of the National Academy of Sciences*, vol. 117, no. 44, pp. 27104–27110, 2020.

[75] Z. Ni, B. Xu, M.- . Sánchez-Martínez, Y. Zhang, K. Manna, C. Bernhard, J. W. F. Venderbos, F. de Juan, C. Felser, A. G. Grushin, and L. Wu, "Linear and nonlinear optical responses in the chiral multifold semimetal RhSi," *npj Quantum Materials*, vol. 5, p. 96, Dec. 2020.

[76] B. Lu, S. Sayyad, M.-Á. Sánchez-Martínez, K. Manna, C. Felser, A. G. Grushin, and D. H. Torchinsky, "Suppression of second-harmonic generation from linear bands in the topological multifold semimetal RhSi," *arXiv:2102.07416*, 2021.

[77] J. L. Mañes, "Existence of bulk chiral fermions and crystal symmetry," *Physical Review B*, vol. 85, Apr. 2012.

[78] G. Chang, S.-Y. Xu, B. J. Wieder, D. S. Sanchez, S.-M. Huang, I. Belopolski, T.-R. Chang, S. Zhang, A. Bansil, H. Lin, and M. Z. Hasan, "Unconventional Chiral Fermions and Large Topological Fermi Arcs in RhSi," *Physical Review Letters*, vol. 119, Nov. 2017.

[79] T. Kajita, "Nobel lecture: Discovery of atmospheric neutrino oscillations," *Rev. Mod. Phys.*, vol. 88, p. 030501, Jul 2016.

[80] A. B. McDonald, "Nobel lecture: The sudbury neutrino observatory: Observation of flavor change for solar neutrinos," *Rev. Mod. Phys.*, vol. 88, p. 030502, Jul 2016.

[81] C. Herring, "Accidental degeneracy in the energy bands of crystals," *Phys. Rev.*, vol. 52, pp. 365–373, Aug 1937.

[82] H. Nielsen and M. Ninomiya, "The adler-bell-jackiw anomaly and weyl fermions in a crystal," *Physics Letters B*, vol. 130, no. 6, pp. 389–396, 1983.

[83] D. Xiao, M.-C. Chang, and Q. Niu, "Berry phase effects on electronic properties," *Reviews of Modern Physics*, vol. 82, pp. 1959–2007, July 2010.

[84] X. Wan, A. M. Turner, A. Vishwanath, and S. Y. Savrasov, "Topological semimetal and Fermi-arc surface states in the electronic structure of pyrochlore iridates," *Phys. Rev. B*, vol. 83, p. 205101, May 2011.

[85] G. Chang, B. J. Wieder, F. Schindler, D. S. Sanchez, I. Belopolski, S.-M. Huang, B. Singh, D. Wu, T.-R. Chang, T. Neupert, *et al.*, "Topological quantum properties of chiral crystals," *Nat. Mater.*, vol. 17, no. 11, p. 978, 2018.

[86] C. Fang, M. J. Gilbert, X. Dai, and B. A. Bernevig, "Multi-Weyl topological semimetals stabilized by point group symmetry," *Phys. Rev. Lett.*, vol. 108, p. 266802, Jun 2012.

[87] S. S. Tsirkin, I. Souza, and D. Vanderbilt, "Composite Weyl nodes stabilized by screw symmetry with and without time-reversal invariance," *Phys. Rev. B*, vol. 96, p. 045102, Jul 2017.

[88] A. Bouhon and A. M. Black-Schaffer, "Global band topology of simple and double Dirac-point semimetals," *Phys. Rev. B*, vol. 95, p. 241101, Jun 2017.

[89] D. S. Sanchez, I. Belopolski, T. A. Cochran, X. Xu, J.-X. Yin, G. Chang, W. Xie, K. Manna, V. Süß, C.-Y. Huang, N. Alidoust, D. Multer, S. S. Zhang, N. Shumiya, X. Wang, G.-Q. Wang, T.-R.

Chang, C. Felser, S.-Y. Xu, S. Jia, H. Lin, and M. Z. Hasan, "Discovery of topological chiral crystals with helicoid arc states," *arXiv:1812.04466 [cond-mat]*, Dec. 2018.

[90] D. Takane, Z. Wang, S. Souma, K. Nakayama, T. Nakamura, H. Oinuma, Y. Nakata, H. Iwasawa, C. Cacho, T. Kim, *et al.*, "Observation of chiral fermions with a large topological charge and associated Fermi-arc surface states in CoSi," *Phys. Rev. Lett.*, vol. 122, no. 7, p. 076402, 2019.

[91] Z. C. Rao, H. Li, T. T. Zhang, S. J. Tian, C. H. Li, B. B. Fu, C. Y. Tang, L. Wang, Z. L. Li, W. H. Fan, J. J. Li, Y. B. Huang, Z. H. Liu, Y. W. Long, C. Fang, H. M. Weng, Y. G. Shi, H. C. Lei, Y. J. Sun, T. Qian, and H. Ding, "Observation of unconventional chiral fermions with long fermi arcs in cosi," *Nature*, vol. 567, no. 7749, pp. 496–499, 2019.

[92] N. B. Schröter, D. Pei, M. G. Vergniory, Y. Sun, K. Manna, F. De Juan, J. A. Krieger, V. Süss, M. Schmidt, P. Dudin, *et al.*, "Chiral topological semimetal with multifold band crossings and long fermi arcs," *Nature Physics*, vol. 15, no. 8, pp. 759–765, 2019.

[93] E. Blount, "Formalisms of band theory," in *Solid state physics*, vol. 13, pp. 305–373, Elsevier, 1962.

[94] M. S. Dresselhaus, "Lecture notes on solid state physics. *Part II: Optical properties of solids.*," *MIT 6.732*, Fall 2001.

[95] G. D. Mahan, *Many-particle physics*. Kluwer Academic-Plenum Publishers, 2000.

[96] F. Flicker, F. de Juan, B. Bradlyn, T. Morimoto, M. G. Vergniory, and A. G. Grushin, "Chiral optical response of multifold fermions," *Physical Review B*, vol. 98, Oct. 2018.

[97] P. E. C. Ashby and J. P. Carbotte, "Chiral anomaly and optical absorption in Weyl semimetals," *Physical Review B*, vol. 89, June 2014.

[98] S. P. Mukherjee and J. P. Carbotte, "Doping and tilting on optics in noncentrosymmetric multi-Weyl semimetals," *Physical Review B*, vol. 97, Jan. 2018.

[99] B. Dóra, J. Kailasvuori, and R. Moessner, "Lattice generalization of the dirac equation to general spin and the role of the flat band," *Phys. Rev. B*, vol. 84, p. 195422, Nov 2011.

[100] J. Sabio, J. Nilsson, and A. H. C. Neto, "f-Sum Rule and Unconventional Spectral Weight Transfer in Graphene," *Physical Review B*, vol. 78, Aug. 2008.

[101] J. Ma and D. Pesin, "Chiral magnetic effect and natural optical activity in metals with or without Weyl points," *Phys. Rev. B*, vol. 92, no. 23, p. 235205, 2015.

[102] S. Zhong, J. E. Moore, and I. Souza, "Gyrotropic magnetic effect and the magnetic moment on the Fermi surface," *Phys. Rev. Lett.*, vol. 116, no. 7, p. 077201, 2016.

[103] G. Chang, S. Y. Xu, B. J. Wieder, D. S. Sanchez, S. M. Huang, I. Belopolski, T. R. Chang, S. Zhang, A. Bansil, H. Lin, and M. Z. Hasan, "Unconventional chiral fermions and large topological Fermi arcs in RhSi," *Physical Review Letters*, vol. 119, no. 20, pp. 1–6, 2017.

[104] F. de Juan, Y. Zhang, T. Morimoto, Y. Sun, J. E. Moore, and A. G. Grushin, "Difference frequency generation in topological semimetals," *Physical Review Research*, vol. 2, p. 012017, Jan. 2020.

[105] D. S. Sanchez, I. Belopolski, T. A. Cochran, X. Xu, J.-X. Yin, G. Chang, W. Xie, K. Manna, V. Süß, C.-Y. Huang, *et al.*, "Topological chiral crystals with helicoid-arc quantum states," *Nature*, vol. 567, no. 7749, p. 500, 2019.

[106] Q. Ma, S.-Y. Xu, C.-K. Chan, C.-L. Zhang, G. Chang, Y. Lin, W. Xie, T. Palacios, H. Lin, S. Jia, *et al.*, "Direct optical detection of Weyl fermion chirality in a topological semimetal," *Nat. Phys.*, vol. 13, no. 9, p. 842, 2017.

[107] G. B. Osterhoudt, L. K. Diebel, M. J. Gray, X. Yang, J. Stanco, X. Huang, B. Shen, N. Ni, P. J. Moll, Y. Ran, *et al.*, "Colossal mid-infrared bulk photovoltaic effect in a type-I Weyl semimetal," *Nat. Mater.*, vol. 18, no. 5, p. 471, 2019.

[108] Z. Ji, G. Liu, Z. Addison, W. Liu, P. Yu, H. Gao, Z. Liu, A. M. Rappe, C. L. Kane, E. J. Mele, *et al.*, "Spatially dispersive circular photogalvanic effect in a Weyl semimetal," *Nat. Mater.*, p. 1, 2019.

[109] J. Ma, Q. Gu, Y. Liu, J. Lai, P. Yu, X. Zhuo, Z. Liu, J.-H. Chen, J. Feng, and D. Sun, "Nonlinear photoresponse of type-II Weyl semimetals," *Nat. Mater.*, vol. 18, pp. 476–481, 2019.

[110] N. Sirica, R. Tobey, L. Zhao, G. Chen, B. Xu, R. Yang, B. Shen, D. Yarotski, P. Bowlan, S. Trugman, *et al.*, "Tracking ultrafast photocurrents in the Weyl semimetal TaAs using THz emission spectroscopy," *Phys. Rev. Lett.*, vol. 122, no. 19, p. 197401, 2019.

[111] D. Rees, K. Manna, B. Lu, T. Morimoto, H. Borrmann, C. Felser, J. Moore, D. H. Torchinsky, and J. Orenstein, "Helicity-dependent photocurrents in the chiral Weyl semimetal RhSi," *Science advances*, vol. 6, no. 29, p. eaba0509, 2020.

[112] Y. Gao, S. Kaushik, E. Philip, Z. Li, Y. Qin, Y. Liu, W. Zhang, Y. Su, X. Chen, H. Weng, *et al.*, "Chiral terahertz wave emission from the Weyl semimetal TaAs," *Nat. Commun.*, vol. 11, no. 1, pp. 1–10, 2020.

[113] Z. Ni, K. Wang, Y. Zhang, O. Pozo, B. Xu, X. Han, K. Manna, J. Paglione, C. Felser, A. G. Grushin, and et al., "Giant topological longitudinal circular photo-galvanic effect in the chiral multifold semimetal CoSi," *Nature Communications*, vol. 12, Jan 2021.

[114] B. Xu, Z. Fang, M.-Á. Sánchez-Martínez, J. W. F. Venderbos, Z. Ni, T. Qiu, K. Manna, K. Wang, J. Paglione, C. Bernhard, C. Felser, E. J. Mele, A. G. Grushin, A. M. Rappe, and L. Wu, "Optical signatures of multifold fermions in the chiral topological semimetal CoSi," *Proceedings of the National Academy of Sciences*, vol. 117, no. 44, pp. 27104–27110, 2020.

[115] M.-Á. Sánchez-Martínez, F. de Juan, and A. G. Grushin, "Linear optical conductivity of chiral multifold fermions," *Phys. Rev. B*, vol. 99, p. 155145, Apr. 2019.

[116] T. Habe, "Dynamical conductivity in the multiply degenerate point-nodal semimetal CoSi," *Physical Review B*, vol. 100, no. 24, p. 245131, 2019.

[117] X. Xu, X. Wang, T. A. Cochran, D. S. Sanchez, G. Chang, I. Belopolski, G. Wang, Y. Liu, H.-J. Tien, X. Gui, *et al.*, "Crystal growth and quantum oscillations in the topological chiral semimetal CoSi," *Physical Review B*, vol. 100, no. 4, p. 045104, 2019.

[118] G. F. Bassani and G. Pastori Parravicini, *Electronic states and optical transitions in solids*. Pergamon Press Oxford, New York, 1st ed. ed., 1975.

[119] L. Maulana, K. Manna, E. Uykur, C. Felser, M. Dressel, and A. Pronin, "Optical conductivity of multifold fermions: The case of RhSi," *Phys. Rev. Research*, vol. 2, no. 2, p. 023018, 2020.

[120] "CoSi Crystal Structure: Datasheet from "PAULING FILE Multinaries Edition – 2012" in SpringerMaterials."

[121] A. Wittmann, K. O. Burger, and H. Nowotny, "Mono- und Disilicidsysteme der Eisengruppe," *Monatshefte für Chemie und verwandte Teile anderer Wissenschaften*, vol. 92, pp. 961–966, Sept. 1961.

[122] P. Giannozzi, S. Baroni, N. Bonini, M. Calandra, R. Car, C. Cavazzoni, D. Ceresoli, G. L. Chiarotti, M. Cococcioni, I. Dabo, *et al.*, "Quantum espresso: a modular and open-source software project for quantum simulations of materials," *Journal of physics: Condensed matter*, vol. 21, no. 39, p. 395502, 2009.

[123] P. Giannozzi, O. Andreussi, T. Brumme, O. Bunau, M. B. Nardelli, M. Calandra, R. Car, C. Cavazzoni, D. Ceresoli, M. Cococcioni, *et al.*, "Advanced capabilities for materials modelling with quantum espresso," *Journal of physics: Condensed matter*, vol. 29, no. 46, p. 465901, 2017.

[124] P. Giannozzi, O. Baseggio, P. Bonfà, D. Brunato, R. Car, I. Carnimeo, C. Cavazzoni, S. De Gironcoli, P. Delugas, F. Ferrari Ruffino, *et al.*, "Quantum espresso toward the exascale," *The Journal of chemical physics*, vol. 152, no. 15, p. 154105, 2020.

[125] D. Wu, N. Barišić, P. Kallina, A. Faridian, B. Gorshunov, N. Drichko, L. J. Li, X. Lin, G. H. Cao, Z. A. Xu, N. L. Wang, and M. Dressel, "Optical investigations of the normal and

superconducting states reveal two electronic subsystems in iron pnictides," *Phys. Rev. B*, vol. 81, p. 100512, Mar 2010.

[126] Y. M. Dai, B. Xu, B. Shen, H. Xiao, H. H. Wen, X. G. Qiu, C. C. Homes, and R. P. S. M. Lobo, "Hidden T-Linear Scattering Rate in $Ba_{0.6}K_{0.4}Fe_2As_2$ Revealed by Optical Spectroscopy," *Phys. Rev. Lett.*, vol. 111, p. 117001, Sep 2013.

[127] B. Xu, Z. C. Wang, E. Sheveleva, F. Lyzwa, P. Marsik, G. H. Cao, and C. Bernhard, "Band-selective clean-limit and dirty-limit superconductivity with nodeless gaps in the bilayer iron-based superconductor $CsCa_2Fe_4As_4F_2$," *Phys. Rev. B*, vol. 99, p. 125119, Mar 2019.

[128] Y. R. Shen, "Surface second harmonic generation: A new technique for surface studies," *Annual Review of Materials Science*, vol. 16, no. 1, pp. 69–86, 1986.

[129] Y. R. Shen, "Surface properties probed by second-harmonic and sum-frequency generation," *Nature*, vol. 337, no. 6207, pp. 519–525, 1989.

[130] A. Dähn, W. Hübner, and K. H. Bennemann, "Symmetry analysis of the nonlinear optical response: Second harmonic generation at surfaces of antiferromagnets," *Phys. Rev. Lett.*, vol. 77, pp. 3929–3932, Oct 1996.

[131] J. C. Petersen, M. D. Caswell, J. S. Dodge, I. A. Sergienko, J. He, R. Jin, and D. Mandrus, "Nonlinear optical signatures of the tensor order in $Cd_2Re_2O_7$," *Nature Physics*, vol. 2, no. 9, pp. 605–608, 2006.

[132] J. W. Harter, Z. Y. Zhao, J.-Q. Yan, D. G. Mandrus, and D. Hsieh, "A parity-breaking electronic nematic phase transition in the spin-orbit coupled metal $Cd_2Re_2O_7$," *Science*, vol. 356, no. 6335, pp. 295–299, 2017.

[133] N. Sirica, P. P. Orth, M. S. Scheurer, Y. M. Dai, M. C. Lee, P. Padmanabhan, L. T. Mix, S. W. Teitelbaum, M. Trigo, L. X. Zhao, G. F. Chen, B. Xu, R. Yang, B. Shen, C. C. Lee, H. Lin, T. A. Cochran, S. A. Trugman, J. X. Zhu, M. Z. Hasan, N. Ni, X. G. Qiu, A. J. Taylor, D. A. Yarotski, and R. P. Prasankumar,

"Photocurrent-driven transient symmetry breaking in the Weyl semimetal TaAs," *arXiv:2005.10308*, May 2020.

[134] V. Mizrahi and J. E. Sipe, "Phenomenological treatment of surface second-harmonic generation," *JOSA B*, vol. 5, no. 3, pp. 660–667, 1988.

[135] R.-P. Pan, H. D. Wei, and Y. R. Shen, "Optical second-harmonic generation from magnetized surfaces," *Phys. Rev. B*, vol. 39, pp. 1229–1234, Jan 1989.

[136] Y. M. Chang, L. Xu, and H. W. K. Tom, "Observation of coherent surface optical phonon oscillations by time-resolved surface second-harmonic generation," *Phys. Rev. Lett.*, vol. 78, pp. 4649–4652, Jun 1997.

[137] A. Kirilyuk and T. Rasing, "Magnetization-induced-second-harmonic generation from surfaces and interfaces," *JOSA B*, vol. 22, no. 1, pp. 148–167, 2005.

[138] D. Hsieh, J. W. McIver, D. H. Torchinsky, D. R. Gardner, Y. S. Lee, and N. Gedik, "Nonlinear optical probe of tunable surface electrons on a topological insulator," *Phys. Rev. Lett.*, vol. 106, p. 057401, Feb 2011.

[139] C. Lee, F. Katmis, P. Jarillo-Herrero, J. S. Moodera, and N. Gedik, "Direct measurement of proximity-induced magnetism at the interface between a topological insulator and a ferromagnet," *Nature communications*, vol. 7, no. 1, pp. 1–6, 2016.

[140] "Far-infrared wave generation," in *Physical Principles of Far-Infrared Radiation* (L. Robinson, ed.), vol. 10 of *Methods in Experimental Physics*, pp. 10–81, Academic Press, 1973.

[141] J. Zhao, J. Fan, W. Liu, H. Shi, N. Xiao, and M. Hu, "Ultra-broadband second-harmonic generation in ZnO nano-tetrapod with over-one-octave bandwidth," *IEEE Photonics Technology Letters*, vol. 31, no. 3, pp. 250–252, 2019.

[142] S. Bergfeld and W. Daum, "Second-harmonic generation in GaAs: Experiment versus theoretical predictions of $\chi^{(2)}_{xyz}$," *Phys. Rev. Lett.*, vol. 90, p. 036801, Jan 2003.

[143] H. P. Wagner, M. Kühnelt, W. Langbein, and J. M. Hvam, "Dispersion of the second-order nonlinear susceptibility in znte, znse, and zns," *Phys. Rev. B*, vol. 58, pp. 10494–10501, Oct 1998.

[144] Z. Li, Y.-Q. Jin, T. Tohyama, T. Iitaka, J.-X. Zhang, and H. Su, "Second harmonic generation in the Weyl semimetal TaAs from a quantum kinetic equation," *Phys. Rev. B*, vol. 97, p. 085201, Feb 2018.

[145] S.-M. Huang, S.-Y. Xu, I. Belopolski, C.-C. Lee, G. Chang, T.-R. Chang, B. Wang, N. Alidoust, G. Bian, M. Neupane, D. Sanchez, H. Zheng, H.-T. Jeng, A. Bansil, T. Neupert, H. Lin, and M. Z. Hasan, "New type of Weyl semimetal with quadratic double Weyl fermions," *PNAS*, vol. 113, pp. 1180–1185, Feb. 2016.

[146] F. de Juan, A. G. Grushin, T. Morimoto, and J. E. Moore, "Quantized circular photogalvanic effect in Weyl semimetals," *Nature Communications*, vol. 8, p. 15995, July 2017. arXiv: 1611.05887.

[147] M.-Y. Yao, J. Noky, K. Manna, N. Kumar, V. Strocov, C. Shekhar, Y. Sun, and C. Felser, "Observation of chirality-neutral Fermi surface in Weyl semimetal candidate $SrSi_2$," *arXiv:2106.11332*, 2021.

[148] K. Manna, N. Kumar, S. Chattopadhyay, J. Noky, M. Yao, J. Park, T. Förster, M. Uhlarz, T. Chakraborty, B. V. Schwarze, *et al.*, "Three-dimensional quasi-quantized Hall insulator phase in $SrSi_2$," *arXiv:2106.11329*, 2021.

[149] Z. Wang, H. Weng, Q. Wu, X. Dai, and Z. Fang, "Three-dimensional Dirac semimetal and quantum transport in Cd_3As_2," *Phys. Rev. B*, vol. 88, no. 12, p. 125427, 2013.

[150] Z. Wang, Y. Sun, X.-Q. Chen, C. Franchini, G. Xu, H. Weng, X. Dai, and Z. Fang, "Dirac semimetal and topological phase transitions in A_3Bi (A= Na, K, Rb)," *Phys. Rev. B*, vol. 85, no. 19, p. 195320, 2012.

[151] S.-M. Huang, S.-Y. Xu, I. Belopolski, C.-C. Lee, G. Chang, B. Wang, N. Alidoust, G. Bian, M. Neupane, C. Zhang, *et al.*, "A Weyl Fermion semimetal with surface Fermi arcs in the transition metal monopnictide TaAs class," *Nat. Commun.*, vol. 6, 2015.

[152] J. E. Sipe and A. I. Shkrebtii, "Second-order optical response in semiconductors," *Physical Review B*, vol. 61, pp. 5337–5352, Feb. 2000.

[153] F. Nastos, B. Olejnik, K. Schwarz, and J. E. Sipe, "Scissors implementation within length-gauge formulations of the frequency-dependent nonlinear optical response of semiconductors," *Phys. Rev. B*, vol. 72, p. 045223, Jul 2005.

[154] O. Pozo and F. de Juan, "Computing observables without eigenstates: Applications to Bloch Hamiltonians," *Phys. Rev. B*, vol. 102, p. 115138, Sep 2020.

[155] J. Bezanson, A. Edelman, S. Karpinski, and V. B. Shah, "Julia: A fresh approach to numerical computing," *SIAM Review*, vol. 59, no. 1, pp. 65–98, 2017.

[156] A. Gulans, S. Kontur, C. Meisenbichler, D. Nabok, P. Pavone, S. Rigamonti, S. Sagmeister, U. Werner, and C. Draxl, "EXCITING: a full-potential all-electron package implementing density-functional theory and many-body perturbation theory," *Journal of Physics: Condensed Matter*, vol. 26, p. 363202, aug 2014.

[157] I. Engström and T. Johnsson, "Least-squares refinement of the structure of RhSi (FeSi-type)," *Acta Chemica Scandinavica*, vol. 19, pp. 1508–1509, 1965.

[158] L. Wu, S. Patankar, T. Morimoto, N. L. Nair, E. Thewalt, A. Little, J. G. Analytis, J. E. Moore, and J. Orenstein, "Giant anisotropic nonlinear optical response in transition metal monopnictide weyl semimetals," *Nature Physics*, vol. 13, no. 4, p. 350, 2017.

[159] A. Avdoshkin, V. Kozii, and J. E. Moore, "Interactions remove the quantization of the chiral photocurrent at Weyl points," *Physical review letters*, vol. 124, no. 19, p. 196603, 2020.

[160] P. Dutta and S. K. Pandey, "Electronic correlation effect on nontrivial topological fermions in CoSi," *The European Physical Journal B*, vol. 94, no. 4, pp. 1–11, 2021.

[161] D. Rees, B. Lu, Y. Sun, K. Manna, R. Ozgur, S. Subedi, C. Felser, J. Orenstein, and D. H. Torchinsky, "Direct measurement of helicoid surface states in RhSi using nonlinear optics," 2021.

[162] D. S. Wu, Z. Y. Mi, Y. J. Li, W. Wu, P. L. Li, Y. T. Song, G. T. Liu, G. Li, and J. L. Luo, "Single crystal growth and magnetoresistivity of topological semimetal CoSi," *Chinese Physics Letters*, vol. 36, p. 077102, Jul 2019.

[163] D. E. Kharzeev, Y. Kikuchi, R. Meyer, and Y. Tanizaki, "Giant photocurrent in asymmetric Weyl semimetals from the helical magnetic effect," *Phys. Rev. B*, vol. 98, p. 014305, Jul 2018.

[164] S. Kaushik and J. Cano, "Magnetic photocurrents in multifold Weyl fermions," *arXiv:2107.05106*, 2021.

[165] C. W. Groth, M. Wimmer, A. R. Akhmerov, and X. Waintal, "Kwant: a software package for quantum transport," *New Journal of Physics*, vol. 16, no. 6, p. 063065, 2014.

[166] J. Ahn and N. Nagaosa, "Theory of optical responses in clean multi-band superconductors," *arXiv:2010.02956*, Oct. 2020.

[167] T. Xu, T. Morimoto, and J. E. Moore, "Nonlinear optical effects in inversion-symmetry-breaking superconductors," *Physical Review B*, vol. 100, 220501(R), p. 220501, Dec. 2019.

[168] C. S. Wang and B. M. Klein, "First-principles electronic structure of Si, Ge, GaP, GaAs, ZnS, and ZnSe. II. optical properties," *Phys. Rev. B*, vol. 24, pp. 3417–3429, Sep 1981.

[169] Y. Chi, H.-G. Xue, and S.-P. Guo, "Designing sulfide borate as a novel type of second-order nonlinear-optical material," *Inorg. Chem.*, vol. 59, Jan 2020.

[170] Z. H. Levine and D. C. Allan, "Linear optical response in silicon and germanium including self-energy effects," *Phys. Rev. Lett.*, vol. 63, pp. 1719–1722, Oct 1989.

[171] J. L. P. Hughes and J. E. Sipe, "Calculation of second-order optical response in semiconductors," *Phys. Rev. B*, vol. 53, pp. 10751–10763, Apr 1996.

[172] B. Sadhukhan, Y. Zhang, R. Ray, and J. van den Brink, "First-principles calculation of shift current in chalcopyrite semiconductor $ZnSnP_2$," *Phys. Rev. Materials*, vol. 4, p. 064602, Jun 2020.

[173] W. Song, G.-Y. Guo, S. Huang, L. Yang, and L. Yang, "First-principles studies of second-order nonlinear optical properties of organic-inorganic hybrid halide perovskites," *Phys. Rev. Applied*, vol. 13, p. 014052, Jan 2020.